

# **Thermal Atomic Level Etching of Al<sub>2</sub>O<sub>3</sub>, HfO<sub>2</sub>, TiN and SiGe**

**Varun Sharma**

Department of Chemistry  
Faculty of Science  
University of Helsinki  
Helsinki, Finland

ACADEMIC DOCTORAL DISSERTATION

*To be presented, with the permission of the Faculty of Science of the University of Helsinki, for public criticism in Auditorium A129 of the Department of Chemistry, A. I. Virtasen aukio 1, on the 21<sup>st</sup> of April, 2023 at 12 o'clock.*

HELSINKI 2023

**Supervisors:**

Dr. Tech. Marko Tuominen  
Dr. Suvi Haukka (retired)  
ASM Microchemistry Oy  
Helsinki, Finland

Prof. Mikko Ritala  
Department of Chemistry  
University of Helsinki  
Helsinki, Finland

**Reviewers:**

Prof. Dr. Andrew V. Teplyakov  
Department of Chemistry and Biochemistry  
University of Delaware  
Delaware, United States of America

Prof. Dr. Fred Roozeboom  
Faculty of Science and Technology  
University of Twente  
Enschede, The Netherlands

**Opponent:**

Prof. Dr. Sami Franssila  
Department of Chemistry and Materials Science  
Aalto University  
Helsinki, Finland

Copyright © 2023 *Varun Sharma*.

*ISBN 978-951-51-8997-4 (softcover)*

*ISBN 978-951-51-8998-1 (PDF)*

*<http://ethesis.helsinki.fi>*

*Unigrafia*

*Helsinki 2023*

*"Why to repeat mistakes ? When you can learn from the other's.....,  
or.. sometimes not." — Anonymous*



# Abstract

With a continuous pursuit of making semiconductor devices and integrated circuits (ICs) faster, better, and more energy efficient, the shrinking of device dimensions became imminent. Today we are approaching the ångström era, where the manufacturability of such devices is becoming challenging. As a result, atomic level processing (ALP) is now most desired. Atomic layer deposition (ALD) and atomic level etching are two such ALP methods that take full advantage of surface chemistry and allow growth and removal of atomistically thin layers of material on a substrate, respectively. Atomic level etching broadly describes the etching that maintains the ångström-level (i.e. below 1 nm) etched-thickness control and uses sequential gas-surface reactions that may be self-limiting. Atomic level etching can be either plasma based (plasma atomic layer etching - PALE), or thermal based (thermal atomic layer etching - ALEt, gas-phase pulsed etching - GPPE). PALE has existed at least for three decades. Although thermal atomic level etching is relatively new, it has evolved rapidly over the last seven years.

In this thesis work, new thermal atomic level etching processes based on  $\text{NbF}_5$ , HF,  $\text{CCl}_4$ ,  $\text{SOCl}_2$ ,  $\text{O}_2$ , and  $\text{O}_3/\text{O}_2$  reactants were developed. The materials that were removed selectively over  $\text{SiO}_2$  and  $\text{Si}_3\text{N}_4$  are  $\text{Al}_2\text{O}_3$ , TiN, and  $\text{HfO}_2$ . Two types of etching processes were investigated, the first one uses sequential exposures of two or more reactants (ALEt), and the second uses pulsing of a single reactant (GPPE) to etch the target. The processes explored here show that the novel etch chemistries are capable of removing the material in the ångström regime isotropically from 3D structures. Thermochemical analyses of possible reactions based on the atomic-scale surface-gas models were carried out using first-principles calculations in density functional theory (DFT) as well as molecular dynamics (MD) simulations. In addition, potential etch reactions were also evaluated using conventional thermodynamic calculations. Finally, the post-etched surfaces were characterized using various surface sensitive techniques such as spectroscopic ellipsometry (SE), X-ray photoelectron spectroscopy (XPS), X-ray reflectivity/diffraction (XRR/XRD), transmission electron microscopy (TEM), atomic force microscopy (AFM), and weighing balance.



# Preface

The research work included in this thesis and in the publications [I, III, IV] was carried out at ASM Microchemistry Oy (ASMM), Helsinki. For me, it was a privilege to have access to the advanced infrastructure of ASMM, continuous guidance, constructive criticism, and support from my senior colleagues at ASM. No matter how busy the days were, you always made sure that there is enough time for the discussions aiming towards the pursuit of improvements.

Special thanks to Dr. Tom Blomberg for teaching and giving me an industrial perspective of the ALD technique. With your continuous support and willingness to take me to the equipment maintenance rides, I learnt a good deal about the in-house processing equipments. I express my heartfelt gratitude to my supervisors from the company, Dr. Suvi Haukka, and Dr. Marko Tuominen. Without your continuous support and feedback, the whole PhD project would not have been possible. Suvi, I feel lucky to have participated in your Chemistry 101 (1-on-1) sessions, which were the key highlight of our overall interaction. The support from ASM as a whole is deeply acknowledged. My sincere gratitude to Dr. Michael Givens for all the suggestions you made and the initiatives you took for me during the course of this project. Dr. Vamsi Paruchuri, I am so glad that there was someone at a higher level who blew the strong winds to help sail this boat. I am grateful to you for all your support in the last few years. The list of appreciations is quite long and it might be difficult to do justice to express a fair amount of gratitude to all the people who made this project a success.

Dr. Ivo Raijmakers, Dr. Han Westendorp, Bob Hollands, Ryan Liebengood, Hannu Huotari, Dr. Pinja Jaspers, and Patrick Lee, without your input, support and feedback to my articles this whole project would have been far-fetched. Thanks to all of you for going beyond your daily tasks and providing all the permissions to publish the research results. Dr. Andrea Illiberi, thank you so much for your support and for giving me enough time off to compile this thesis work.

Jaakko Anttila, Robert Huggare, Dr. Raija Matero, Dr. Timo Asikainen, and Sari Kaipio are thanked for their support in teaching and handling the relevant equipment. A big bow to all of you for providing me with the facilities. Thank you Kirsi Kylänpää for making the working place full of fun. Dr. Antti Niskanen, thank you for the fruitful discussion on the metrology.

I am grateful to have the full support from Prof. Mikko Ritala from the Department of Chemistry at the University of Helsinki. It all started with a mere participation in your course "Chemistry of thin films", and the way the course was presented ignited a spark in me to take this challenge to a next level. Thank you so much for giving me the opportunity and for reposing your faith in me. This whole project would have never become a reality without your feedback and the guidance. You are a living example of what people describe as an ideal professor.

Many thanks go to Prof. Dr. Andrew V. Teplyakov and Prof. Dr. Fred

Roozeboom for acting as the pre-examiners of the thesis. Your valuable comments broadened my perspective and added another level of understanding. I am grateful to Prof. Dr. Sami Franssila for acting as an opponent for this work.

With immense pleasure, I wish to express my deep sense of gratitude to my co-authors: Dr. Simon Elliot, Dr. Suresh Kondati Natarajan, Shaun Cembella, Dr. Wes Graff, and Dr. Rajesh Odedra, without your continuous support and participation this PhD project would not have been successfully completed. I express my deep gratitude to Dr. Aziz Abdulagatov and Prof. Steven M. George from the University of Colorado, Boulder for the opportunity to collaborate on their ongoing research that led to the publication [II]. In addition, I am grateful to all of you for encouraging the technical discussions during the collaboration, which always resulted in a better understanding and personal growth.

I express my sincere thanks to Bernd Bock from Tascon GmbH and Eurofins EAG Laboratories (esp. Dr. Sukanta Biswas) for their valuable support and discussions on various sets of TEM and XPS analyses.

Last but not least, I am so grateful to my family: Varinder, Veena, Maarja, Elora, and Vasudha for their continuous encouragement and patience over the past few years. With all your blessings, I am closing this amazing chapter of my life and moving ahead to embrace the Now.

Helsinki, March 9, 2023

*Varun Sharma*



# Contents

<b>Abstract</b>	<b>v</b>
<b>Preface</b>	<b>vii</b>
<b>Acronyms</b>	<b>xi</b>
<b>List of Publications</b>	<b>xiii</b>
<b>1 Introduction</b>	<b>1</b>
1.1 Etching in nanoelectronics . . . . .	1
1.2 Aim and outline of this thesis . . . . .	2
<b>2 Atomic level etching</b>	<b>3</b>
2.1 Definition of atomic level etching . . . . .	3
2.2 Classification of atomic level etching . . . . .	3
2.2.1 Self-limiting atomic level etching . . . . .	4
2.2.2 Non self-limiting atomic level etching . . . . .	7
2.2.3 Etch rate vs. etch per cycle . . . . .	8
2.3 Features of ALEt processes . . . . .	9
2.3.1 Atomic Level Precision . . . . .	9
2.3.2 Isotropic etching . . . . .	9
2.3.3 Selective etching . . . . .	10
2.3.4 Minimal surface damage . . . . .	10
2.4 ALEt processes and mechanisms . . . . .	11
2.4.1 Surface modification . . . . .	15
2.4.2 Volatilization . . . . .	16
2.5 Challenges in ALEt . . . . .	17
<b>3 Experimental techniques</b>	<b>19</b>
3.1 Experimental setup . . . . .	19
3.2 Etch target thin films . . . . .	19
3.3 Etchants and process gases . . . . .	20
3.4 Film characterization techniques . . . . .	21
3.5 Computational chemistry . . . . .	22
<b>4 Results and discussion</b>	<b>25</b>
4.1 Al <sub>2</sub> O <sub>3</sub> etching by NbF <sub>5</sub> -CCl <sub>4</sub> . . . . .	25
4.1.1 DFT investigations of the etch-mechanism . . . . .	25
4.1.2 Etching experiments . . . . .	29
4.1.3 Post-etch film characterization . . . . .	31
4.1.4 Reaction mechanism . . . . .	34
4.2 TiN etching by NbF <sub>5</sub> -CCl <sub>4</sub> or CCl <sub>4</sub> alone . . . . .	36
4.2.1 Computational chemistry . . . . .	36
4.2.2 Effect of etchant pulse times . . . . .	41
4.2.3 Effect of etching temperature . . . . .	42

4.2.4	Post-etch film characterization . . . . .	43
4.3	TiN etching by $\text{SOCl}_2$ . . . . .	45
4.3.1	Thermodynamic calculations . . . . .	45
4.3.2	Effect of etchant pulse and purge times . . . . .	46
4.3.3	Selectivity and effect of etching temperature . . . . .	47
4.3.4	Post-etch film characterization . . . . .	47
4.4	SiGe etching by $(\text{O}_2$ or $\text{O}_3/\text{O}_2)$ -HF-TMA . . . . .	50
4.4.1	Etching experiments . . . . .	50
4.4.2	Thermodynamic calculations . . . . .	51
4.4.3	XPS analysis of the post-etched film . . . . .	52
4.5	$\text{HfO}_2$ etching by $\text{NbF}_5\text{-CCl}_4$ . . . . .	54
4.5.1	Effect of reactant pulse times . . . . .	54
4.5.2	Thermodynamics of the etch chemistry . . . . .	55
4.5.3	Post-etch film characterization . . . . .	55
4.6	Activation energy determination . . . . .	58
<b>5</b>	<b>Conclusions and outlook</b>	<b>61</b>
	<b>Bibliography</b>	<b>63</b>
<b>A</b>	<b>Bond dissociation energies</b>	<b>79</b>

# Acronyms

acac	Acetylacetonate ligand
AFM	Atomic Force Microscopy
ALD	Atomic Layer Deposition
ALE	Atomic Layer Etching
ALEt	Thermal Atomic Layer Etching
ALP	Atomic Level Processing
CVE	Chemical Vapor Etching
DFT	Density Functional Theory
DMAC	Dimethylaluminum chloride
FET	Field Effect Transistor
FIB	Focused Ion Beam
GAA	Gate-All-Around
GPPE	Gas-Phase Pulsed Etching
Hacac	Acetylacetone
hfac	Hexafluoroacetylacetonate ligand
Hhfac	Hexafluoroacetylacetone
Hthd	2,2,6,6-Tetramethyl-3,5-heptanedione
IC	Integrated Circuit
LPCVD	Low Pressure Chemical Vapor Deposition
MD	Molecular Dynamics
Me	Methyl
MOS	Metal Oxide Semiconductor
NS	Nanosheet
PALE	Plasma Atomic Layer Etching
PVD	Physical Vapor Deposition
RBS	Rutherford Backscattering Spectrometry
SE	Spectroscopic Ellipsometry
TEM	Transmission Electron Microscopy
TMA	Trimethylaluminum
TOx	Thermal Oxide
VNAND	Vertically-stacked Not AND Flash Memory
XPS	X-ray Photoelectron Spectroscopy
XRD	X-ray Diffraction
XRR	X-ray Reflectivity



# List of publications

This dissertation summarizes all ALEt processes known in the literature (up to Oct. 2022) and the following publications, which are referred to in the text by corresponding roman numerals.

**I Thermal gas-phase etching of titanium nitride (TiN) by thionyl chloride (SOCl<sub>2</sub>)**

Varun Sharma, Tom Blomberg, Suvi Haukka, Shaun Cembella, Michael E. Givens, Marko Tuominen, Rajesh Odedra, Wes Graff, and Mikko Ritala,  
*Applied Surface Science*, 2021, **540**, 148309.

**II Thermal atomic layer etching of germanium-rich SiGe using an oxidation and “conversion-etch” mechanism**

Aziz I. Abdulagatov, Varun Sharma, Jessica A. Murdzek, Andrew S. Cavanagh, and Steven M. George  
*Journal of Vacuum Science & Technology A*, 2021, **39**, 022602.

**III Thermal Atomic Layer Etching of Aluminum Oxide (Al<sub>2</sub>O<sub>3</sub>) using Sequential Exposures of Niobium Pentafluoride (NbF<sub>5</sub>) and Carbon Tetrachloride (CCl<sub>4</sub>): A Combined Experimental and Density Functional Theory Study of the Etch Mechanism**

Varun Sharma, Simon D Elliott, Tom Blomberg, Suvi Haukka, Michael E Givens, Marko Tuominen, and Mikko Ritala  
*Chemistry of Materials*, 2021, **33**, 2883–2893.

**IV Combining Experimental and DFT Investigation of the Mechanism Involved in Thermal Etching of Titanium Nitride Using Alternate Exposures of NbF<sub>5</sub> and CCl<sub>4</sub>, or CCl<sub>4</sub> only**

Varun Sharma, Suresh Kondati Natarajan, Simon D. Elliott, Tom Blomberg, Suvi Haukka, Michael E. Givens, Marko Tuominen, and Mikko Ritala  
*Advanced Materials Interfaces*, 2021, **8**, 2101085.

In articles [I, III, IV], the author planned and performed the experiments and analysed the data. Most of the film characterizations (AFM, ellipsometry, weight, XPS, XRR, and XRD) were performed by the author. TEM imaging was outsourced to EAG Laboratories, CA, USA and the analyses of the images were done by the author together with EAG experts. The basic thermodynamic calculations using HSC software were carried out by the author. The author wrote the first drafts of the articles [I, III, IV] (except the DFT sections in III, IV) and finalised them with the co-authors. In article II, the author performed the XPS analyses and wrote the introduction and part of the article.

## **Selected list of patents**

- 1 "Showerhead device for semiconductor processing system"  
T. E. Blomberg, and V. Sharma, 2022, US Patent 11,437,249 B2,
- 2 "Chemical dispensing apparatus and methods for dispensing a chemical to a reaction chamber"  
V. Sharma, 2022, US Patent 11,387,120 B2
- 3 "Thermal atomic layer etching processes"  
T. E. Blomberg, V. Sharma, S. Haukka, M. Tuominen, and C. Zhu, 2022, US Patent App. 2022/0119,962 A1
- 4 "Method of cleaning a surface"  
S. Deng, A. Illiberi, D. Chiappe, E. Tois, G. A. Verni, M. Givens, and V. Sharma, 2022, US Patent App. 2022/0068,634 A1
- 5 "Atomic layer etching processes"  
T. E. Blomberg, V. Sharma, S. Haukka, M. Tuominen, and C. Zhu, 2021, US Patent 11,183,367
- 6 "Reactor system including the reactor, and methods of manufacturing and using same"  
T. E. Blomberg, V. Sharma, and C. Zhu, 2021, US Patent 11,114,283 B2
- 7 "Atomic layer etching"  
C. Dezelah, and V. Sharma, 2021, US Patent App. 2021/0175,088 A1
- 8 "Semiconductor vapor etching device with intermediate chamber"  
T. E. Blomberg, and V. Sharma, 2021, US Patent App. 2021/0020,469 A1

# Chapter 1: Introduction

## 1.1 Etching in nanoelectronics

Creation of the miniature wild world residing in the integrated circuit (IC) chips requires a balanced combination of various advanced processing techniques. This world is populated with devices such as transistors, diodes, capacitors, and other components that are well connected for electrons to travel across efficiently. Ever since its inception, this world is shrinking, becoming dense and has evolved to a point where more advanced 3D architectures are needed to make it less power hungry and optimise its overall operations. Two main techniques that are necessary in the realizing of the IC world are deposition and etching. In the deposition process, material is added on the substrate surface while in the etching process material is removed from the surface. In order to further the miniaturization, the ability of these techniques to provide precise atomic level processing (ALP) is becoming of prime importance. Atomic layer deposition (ALD) and atomic level etching are examples of such techniques.

ALD is a chemical technique that utilizes two or more self-limiting gas-surface reactions to deposit atomic thin films of various materials in a highly conformal manner.<sup>1,2</sup> In ALD, the reactions can be activated using thermal energy, plasma, photons, and electrons. However, the thermal ALD offers the advantage of depositing materials on non-line-of-sight features conformally due to the self-limiting reactions, isotropicity of the thermal energy, randomness of the gaseous reactants, and stability of the reactants in the gas phase. Since the 1970s, innovations in thermal ALD chemistries and related processing equipment have made the deposition of vast list of materials possible.<sup>2,3</sup>

Atomic level etching uses gas-surface reactions in a sequential manner to remove thin layers of material from the substrate. Atomic level etching can be either plasma based (plasma atomic layer etching - PALE), or thermal based (thermal atomic layer etching - ALEt, gas-phase pulsed etching - GPPE). In PALE, the plasma-generated energetic species remove material from the surface, while thermal atomic level etching relies on thermal energy to generate and volatilize etch products from the substrate surface. The idea of using plasma etching in the manufacturing of IC chips was first conceived by Stephen M. Irving around 1970,<sup>4,5</sup> but it was not until 1988 that the first patent on PALE was made public.<sup>6</sup> Advancements in PALE started in the 1990s, and over the last three decades, PALE has developed in parallel with ALD.<sup>7</sup> Consequently, etching and deposition of thin layers of materials within the atomic-regime control has become possible. Despite the inherent directionality in PALE, researchers have studied both the isotropic and anisotropic etching capabilities. Now, for the industry that is rapidly adopting complex 3D device architectures such as gate-all-around (GAA), nanosheets (NS), forksheets, and nanowire-based MOSFET transistors as well as VNAND memory,<sup>8-12</sup> isotropic etching is becoming equally important

to anisotropic etching. Moreover, device dimensions are shrinking below 10 nm and PALE alone cannot provide sufficient isotropicity due to the short lifetimes of the reactive species generated by plasma. Therefore, ALEt is now sought after. The very first patent that described thermal atomic layer etching was filed in 1981 by Suwa Seikosha KK<sup>13</sup> and published in 1983. Surprisingly, since then ALEt remained dormant and picked up the pace in 2015.<sup>14</sup>

With the advent of ALEt, the realization of 3D device architectures, as well as heterogeneous 3D integration of several functional blocks such as logic, memory, sensors, and MEMS are now possible.<sup>10</sup> Moreover, ALEt is not a direct replacement of PALE, as both types of etching are important and needed for future devices that are not limited to the IC chips alone.

## 1.2 Aim and outline of this thesis

The aim of the thesis was to develop new thermal atomic level etching processes for materials used in semiconductor devices and to assess their capability of performing isotropic removal from three dimensional features. In addition, the goal was to selectively etch one material over the other. This thesis explores the feasibility of various novel thermal etching chemistries and it provides several pathways to etch one material over the other.

Chapter 2 introduces its readers to the definition of atomic level etching and its flavours, features of ALEt as well as the involved mechanisms, summary of all known ALEt processes, and some existing challenges in ALEt. In Chapter 3, various experimental techniques used in this research work are discussed. Chapter 4 summarizes the results and observations from the published articles [I-IV] and gives a glimpse of unpublished work. This chapter further discusses the thermodynamics of the etching reactions together with the predicted etch products and reaction pathways. Moreover, the experimental findings of the etch processes are discussed. In Chapter 5 the conclusions and recommendations for future research in ALEt are presented.



## Chapter 2: Atomic level etching

The aim of this chapter is to introduce readers to the fundamentals of atomic level etching. Section 2.1 covers a broad definition of atomic level etching. Section 2.2 categorizes atomic level etching based on the type of gas-surface reactions. Section 2.3 discusses some features of thermal atomic layer etching (ALEt, a subcategory) processes. Later in section 2.4, a summary of known ALEt processes is provided in a tabular form and various mechanisms involved in ALEt are explored. Finally, the chapter is closed with a discussion on some challenges in ALEt.

### 2.1 Definition of atomic level etching

Atomic level etching processes are based on cyclic and sequential gas-surface reactions that may or may not be self-limiting. Each cycle consists of one or more gas-surface reactions, which leads to the net removal from the target surface. Ideally, after each cycle the same amount of material is removed from the surface. Atomic level etching is broadly defined as a technique that removes material from the substrate in atomic-regime, i.e. as long as the etched layers are below 1 nm/cycle in thickness, the term atomic level etching is applicable. The etch cycles are repeated to either achieve a specific target thickness or remove one material completely over the other.

### 2.2 Classification of atomic level etching

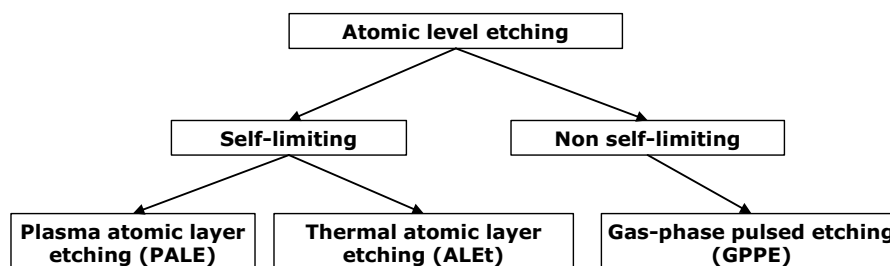


Figure 2.1: Classification of atomic level etching based on the type of gas-surface reactions.

Based on the type of the gas-surface reactions, atomic level etching can be categorized as either self-limiting or non self-limiting as shown in Figure 2.1. In the self-limiting atomic level etching, at least one gas-surface reaction is self-limiting and is further classified as plasma atomic layer etching (PALE) and thermal atomic layer etching (ALEt). In the literature, self-limiting atomic level etching is somewhat interchangeably described using terms such as atomic layer etching (ALE or ALEt) and plasma atomic layer etching (ALE or

PALE), which may be a little confusing to the readers.<sup>15-19</sup> Thus, here keeping the terms consistent with the literature while attempting to minimize the confusion, the plasma based ALE is called PALE and thermal ALE is defined as ALEt. On the other hand, the non self-limiting atomic level etching is based on pulsing of a reactant in a cyclic manner and is called gas-phase pulsed etching (GPPE) technique. In publications II, III, and IV, ALEt processes are reported, while GPPE processes are described in publications I and IV.

## 2.2.1 Self-limiting atomic level etching

Atomic level etching is a technique that provides atomic level precision while removing material from the surface. Ideally, a self-limiting atomic level etching process is based on cyclic, sequential, and self-limiting gas-surface reactions. The self-limiting reactions involve surface modification by the first reactant followed by the formation and release of volatile by-products upon exposure to the second reactant. More than two gas-surface reactions may be used in this technique. The inert gas purges are introduced in between two gas-surface reactions to remove the excess reactant molecules and the by-products.

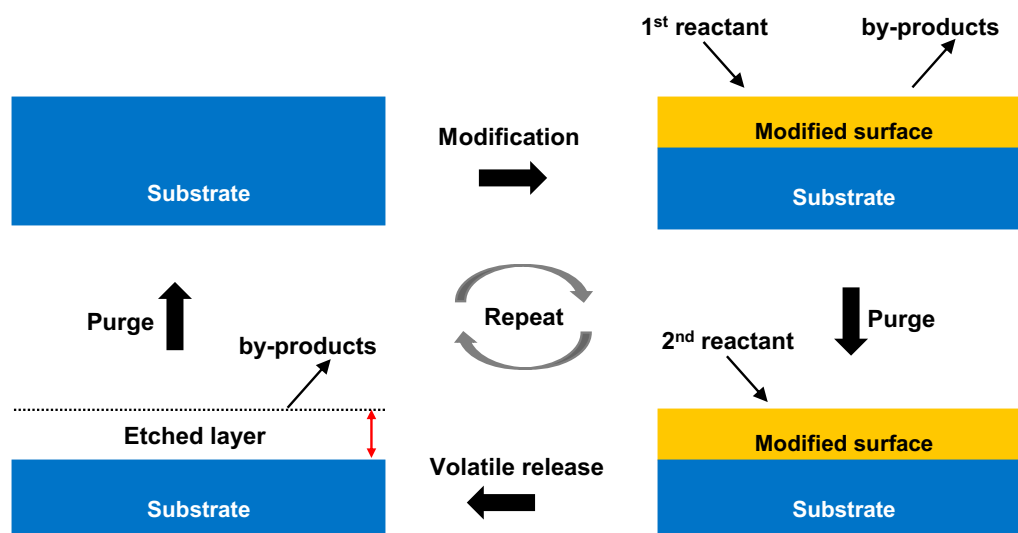


Figure 2.2: Block diagram of a complete atomic level etching cycle based on surface modification and release of volatile by-products (copyright 2022 © the author).

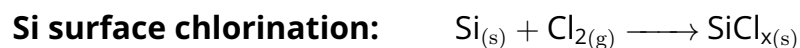
Figure 2.2 shows an atomic level etching cycle based on two gas-surface reactions. The first reactant modifies a top part of the substrate. Based on the type of surface reactions, there is a possibility of formation of volatile by-products during this step. However, in some cases volatile by-products might not form e.g. oxidation of metals<sup>20,21</sup> or adsorption of Cl species on silicon.<sup>7,22</sup> The second step is the exposure to the second reactant (etchant) which converts the modified surface into volatile species. After this step, the modified surface is removed. For this to occur, a sufficient temperature is required for the gas-surface reaction to take place and volatilize the surface species, or enough energy must be provided by the reactive species

originated in plasma to cause the desorption.<sup>22</sup> In this manner, the etching takes place through the modification of the initial substrate followed by the volatilization of the modified surface. The various forms of energies that can drive either the modification or the volatilization steps are chemical energy, kinetic energy,<sup>7</sup> thermal energy,<sup>15,23,24</sup> electrons,<sup>25-28</sup> ions,<sup>22,29</sup> neutral beam,<sup>30</sup> and other forms of radiation.<sup>31-34</sup> Based on these energies, one can categorize self-limiting atomic level etching technique. The existing flavors of this technique are the much-developed plasma atomic layer etching (PALE),<sup>7,35-37</sup> and the recently explored thermal atomic layer etching (ALEt).<sup>38-40</sup>

### 2.2.1.1 Plasma Atomic Layer Etching (PALE)

PALE is a process of removing material from the surface where plasma is utilized in either the surface modification or the volatilization, or both. The plasma uses a glow discharge to create chemically reactive species from relatively inert gases such as H<sub>2</sub>, N<sub>2</sub>, Ar, CF<sub>4</sub>, SF<sub>6</sub>, etc.<sup>22</sup> Also chemically reactive species such as electrons, ions, radicals, or neutral atoms acquire kinetic energy due to the presence of biasing and thus, have directionality.<sup>22,29</sup> In Figure 2.3 a), the directional etching of silicon is used as an example to describe a complete PALE cycle. It is based on sequential exposures to chlorine gas and argon plasma with intermittent N<sub>2</sub> purges. In Figure 2.3 a), step i) shows silicon atoms forming a substrate with a smooth surface. In reality, silicon surfaces contain many defects<sup>41</sup> which further increases the reactivity with plasma-generated species.

In the subsequent step of chlorination (Figure 2.3 a) ii), the silicon surface is exposed to the diatomic chlorine gas (Cl<sub>2</sub>) which upon reaction modifies the silicon surface in a self-limiting manner to SiCl<sub>x</sub> surface species.<sup>42</sup> Chlorination can be performed by either thermal or plasma reaction. In the reaction below, the thermal chlorination uses Cl<sub>2</sub> gas. In an ideal Si PALE, no etching takes place during the chlorination step<sup>7</sup> and a room temperature is chosen to minimize thermal desorption of SiCl<sub>x</sub> species.<sup>36</sup> Thus, the chlorination is self-limiting in nature. The gas-phase chlorination can etch silicon by itself at high temperatures ( $\geq 650$  °C)<sup>36</sup> and this type of etching is called spontaneous etching. Plasma chlorination is performed in order to increase the production yield.<sup>7</sup>



Afterwards, the excess of unreacted chlorine is purged away from the etch reactor with the help of inert gases such as N<sub>2</sub> or Ar. This in-between inert gas purging eliminates interaction between the surface modification and the volatilization steps. Any overlap of these two steps may result in the loss of atomic level precision.<sup>7</sup>

The next step iii) is the desorption or volatilization step, where plasma-generated argon ions (Ar<sup>+</sup>) with sufficient kinetic energy assist in the desorption of the SiCl<sub>x</sub> surface species, as shown in the reaction below.<sup>31,36,42</sup> The main desorbed species are found to be SiCl<sub>2</sub>, SiCl, and

$\text{SiCl}_4$ .<sup>36,42,43</sup> After the argon plasma step, an inert gas purging is performed to remove all the gaseous by-products. This desorption step is also self-limiting at  $\text{Ar}^+$  energy of 50 eV.<sup>42</sup>

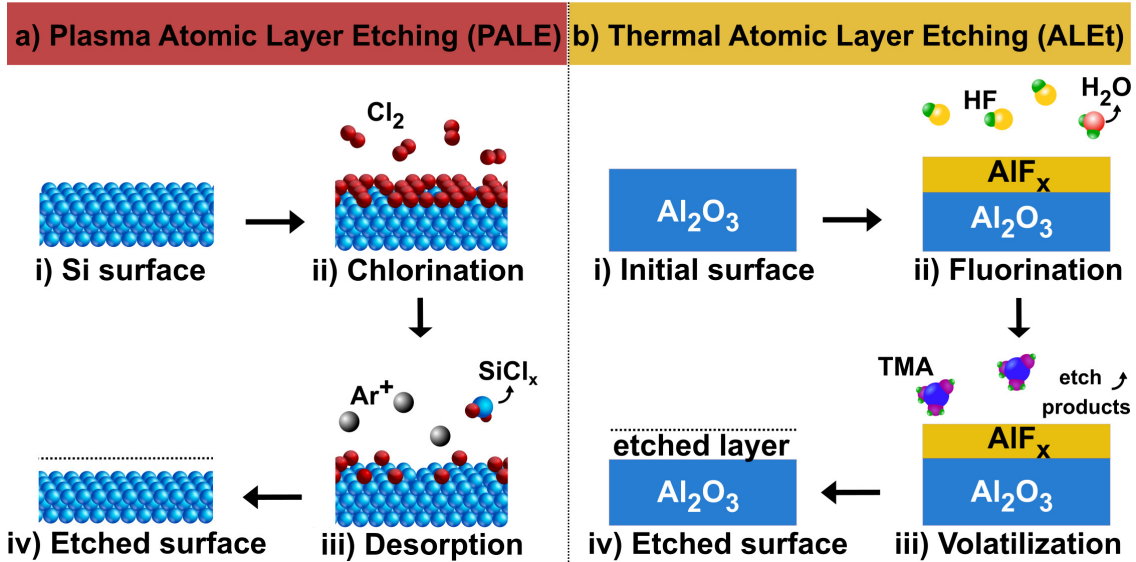


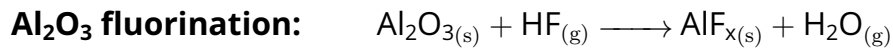
Figure 2.3: Schematic representation of a full etching cycle for: a) silicon by plasma atomic layer etching and b)  $\text{Al}_2\text{O}_3$  by thermal atomic layer etching (copyright 2022 © the author). The subfigures i) and iv) are the starting and end phases of each etch cycle.

### 2.2.1.2 Thermal Atomic Layer Etching (ALEt)

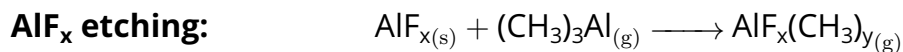
ALEt is a non-plasma technique that removes the material from the surface with the help of chemical reactions at elevated temperatures. The elevated temperature is necessary to provide sufficient energy for the reactions to occur and desorb volatile species from the surface. Ideally, each ALEt cycle consists of two or more sequential gas-surface reactions and at least, one of these is self-limiting. The reactions are based on a surface modification and formation of volatile gaseous products<sup>15</sup> and are discussed in more details in section 2.4. Unlike its counter part, i.e., thermal ALD, in ALEt the bonds between surface atoms and the underlying substrate are broken resulting in the formation of volatile species that leave the surface. The released volatile species are then evacuated by the vacuum pumping system. ALEt can be seen as the "reverse of thermal ALD", where material is now sequentially removed from the surface.<sup>15</sup>

In Figure 2.3 b),  $\text{Al}_2\text{O}_3$  ALEt is used to illustrate one complete ALEt cycle.<sup>44</sup> The step 2.3 b) i) represents the initial  $\text{Al}_2\text{O}_3$  etch target surface. During the fluorination step ii), the  $\text{Al}_2\text{O}_3$  surface is exposed to the HF gas. Here the starting  $\text{Al}_2\text{O}_3$  surface gets converted into the  $\text{AlF}_x$  surface. The fluorination step can be described with the help of a chemical reaction mentioned below,

where water is released as a by-product. Even though the oxygen from the  $\text{Al}_2\text{O}_3$  layer(s) is removed in this step, in the literature this step is termed as a fluorination step. For simplicity in this thesis, the term fluorination is used to keep the terminology consistent with the literature. After the fluorination is performed, an inert gas purging is needed to remove the gaseous by-products and the surplus reactants from the etch reactor. This inert gas purging is needed to keep the fluorination step separated from the volatilization step. Otherwise, the atomic level precision is may be lost.



In step iii), the volatilization of the previously formed  $\text{AlF}_x$  surface takes place upon trimethylaluminum (TMA) exposure.<sup>40</sup> In the literature, this step is known as etching step involving ligand-exchange reaction.<sup>15</sup> In the ligand-exchange reaction, fluorine from  $\text{AlF}_x$  surface and  $\text{CH}_3$  from TMA exchange the central metal atoms to form volatile etch products. One of the identified etch products is dimethylaluminum fluoride ( $(\text{CH}_3)_2\text{AlF}$ ).<sup>40,45</sup> After the ligand-exchange reaction, an inert gas purge step is followed to remove the volatile reaction products from the etch reactor. Typically, the  $\text{Al}_2\text{O}_3$  ALEt is performed at temperatures above  $200^\circ\text{C}$ .<sup>38,44</sup>



The thickness of  $\text{Al}_2\text{O}_3$  removed in one cycle is defined in terms of etch per cycle (EPC). In order to achieve the desired etch thickness, several etch cycles are performed.

### 2.2.2 Non self-limiting atomic level etching

If the etch target reacts spontaneously and forms volatile species upon contacting the reactant molecules, the etching occurs continuously as long as the etchant and the target material encounter each other. Sufficient temperature and continuous evacuation of the formed volatile species ensure the etching is favoured. The non self-limiting (spontaneous) etching is considered as continuous vapor phase etching (CVE). Several reports of CVE exist in the literature, for example etching of Si by  $\text{XeF}_2$  or  $\text{F}_2$ ,<sup>46</sup> etching of  $\text{TiO}_2$  by  $\text{WF}_6$ <sup>47</sup> and etching of  $\text{AlF}_3$  by TMA.<sup>48</sup> In order to achieve atomic level etch control, discontinuity in CVE is needed. This discontinuity, i.e. switching the etching on and off, is achieved by either adding cycles (as in GPPE) or surface modification steps (as in ALEt) as additional parameters. In GPPE, surface modification and etching occur simultaneously. ALEt is a special type of CVE where the surface modification step makes the spontaneous etch intermittent and hence, digital.

Gas-Phase Pulsed Etching (GPPE) is a special variant of continuous or spontaneous thermal etching and does not involve any plasma step.<sup>46,49-57</sup> GPPE utilizes cyclic pulses of the gaseous etchant followed by the inert gas purging at elevated temperatures. Thermal etching of TiN by  $\text{SOCl}_2$  or  $\text{CCl}_4$  are examples of GPPE [I, IV]. Figure 2.4, represents a complete GPPE cycle.

The initial substrate is exposed to the etchant gas for a short duration and during this step, etch products are formed. This exposure step involves both the surface modification and the volatilization steps. After the etchant exposure, inert gas purging is performed to remove all the by-products and excess of the etchant molecules. In this manner, the top layer of the material is etched. After a complete GPPE cycle, an original surface is created once all the by-products are volatilized from the surface. Several cycles of etchant/purge are repeated in order to remove a certain thickness from the target films. In GPPE, the etch per cycle can be maintained below 1 nm and hence, atomic level precision is achieved. Various process parameters such as the pulse time of the etchant, inert gas purge time, partial pressure of the etchant, temperature, and reactor pressure can be used to tune the EPC. GPPE can also offer isotropic etching from the non-line-of-sight features shown in articles I and IV.

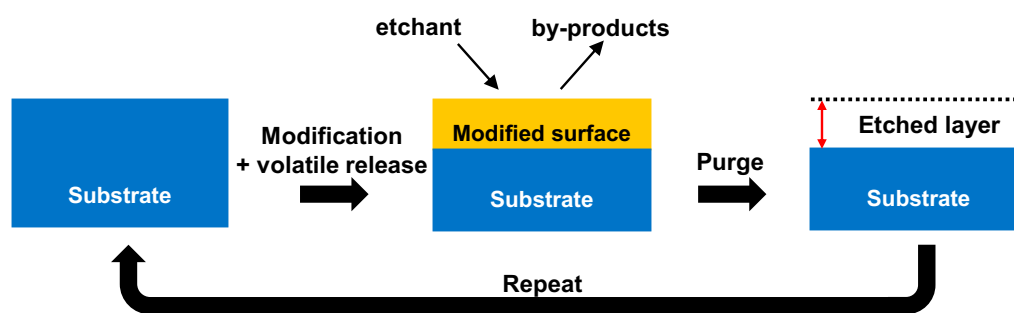


Figure 2.4: Schematic representation of a complete cycle of gas-phase pulsed etching (copyright 2022 © the author).

### 2.2.3 Etch rate vs. etch per cycle

Typically for CVE or plasma based continuous etching processes, the etch rates are quantified as the removed thickness (typically in nm or Å) per unit time such as Å/min, nm/min, and Å/sec.<sup>7,22</sup>

On the contrary, in PALE, ALEt and GPPE processes where the etching cycles ensure a digital control over the removed thickness, the etch per cycle (EPC) is often used. EPC is defined as the thickness removed per cycle, and its unit is typically Å/cycle. In the ideal atomic level etching (PALE, ALEt and GPPE), almost the same amount of material is removed from the surface in each cycle, hence a constant EPC with cycles is expected. The atomic level precision is extremely desirable for the fabrication of complex and three dimensional devices with sub-10 nm dimensions.<sup>16,17</sup>

There are several factors that affect the EPC of an ALEt process. Under self-limiting ALEt conditions, temperature is the most important factor. Typically, the higher the temperature, the higher the EPC.<sup>15,48</sup> In a non or partially self-limiting thermal atomic level etching, the partial pressure of the etchant can play an important role. With higher partial pressures of the etchants a higher EPC is observed.<sup>58</sup> However, if the modified surface layer acts as a diffusion barrier and further stops the gas-surface reaction from advancing into the

solid, a saturated EPC with etchant partial pressure is observed. One such example is the fluorination of  $\text{Al}_2\text{O}_3$  by HF in which at higher partial pressures of HF, an increase in the thickness of  $\text{AlF}_3$  is observed.<sup>59</sup> An effect of no-purge times after the etchant exposures on EPC has also been studied. A significant increase in the EPC was observed in a purge-less ALEt (Rapid-ALEt).<sup>60</sup>

The other factors that can impact EPC are the phase of the material,<sup>61</sup> material preparation technique (ALD vs. CVD vs. epitaxy etc.), and obviously the choice of the etchant or the etch chemistry.<sup>15</sup> EPC of crystalline films is significantly lower than that of the amorphous films of the same material.<sup>61,62</sup> The higher EPC of amorphous films can be due to the lower density of amorphous films. Films of lower density are more prone to molar expansion, which is inherent to the fluorination step.<sup>61</sup>

## 2.3 Features of ALEt processes

### 2.3.1 Atomic Level Precision

One of the main advantages of ALEt is its ability to process material in the atomic regime.<sup>7,15,16</sup> Due to the sequential and self-limiting gas-surface reactions, an ideal ALEt offers a precise control of the removed thickness within few ångströms.<sup>14</sup> Similar to ALD, the ability of ALEt to maintain atomic scale precision while etching may endorse the realization of complex 3D integrated circuits.<sup>63</sup>

### 2.3.2 Isotropic etching

Another key feature of ALEt is its isotropic etching property. The isotropic etching is uniform in all directions.<sup>17</sup> ALEt lacks directionality due to the absence of plasma-generated energetic charged or neutral species.<sup>17</sup> ALEt relies on self-limiting gas-surface reactions that are thermally activated at elevated temperatures. Ideally in ALEt, the EPC is the same regardless of the location in 3D structures. This key property helps to achieve conformal etching of materials from the non-line-of-sight surfaces. On the contrary, in PALE the kinetically energized reactive species have directionality and, consequently, provide anisotropic etching.<sup>22</sup> In the anisotropic etching, the etch occurs in the direction perpendicular to the wafer surface. Anisotropic etching is important for the creation of high aspect ratio structures like those required in finFETs,<sup>16</sup> multiple patterning,<sup>64-66</sup> VNAND, DRAM capacitor trenches, etc. On the other hand, isotropicity in ALEt is going to be important in the fabrication of future complex 3D architectures such as gate-all-around (GAA), nanosheet and forksheet devices.<sup>9,16</sup>

Figure 2.5 compares the isotropic and conformal etching to the anisotropic and non-conformal etching. The schematic in the middle shows a patterned substrate in blue and the conformal target film on top in red. In PALE, the directionality of the reactive species such as ions and neutral atoms provide different etch rates for the top vs. side, as depicted in Figure 2.5 a). On the other hand, ALEt etches conformally with the same EPC for the top, side, as

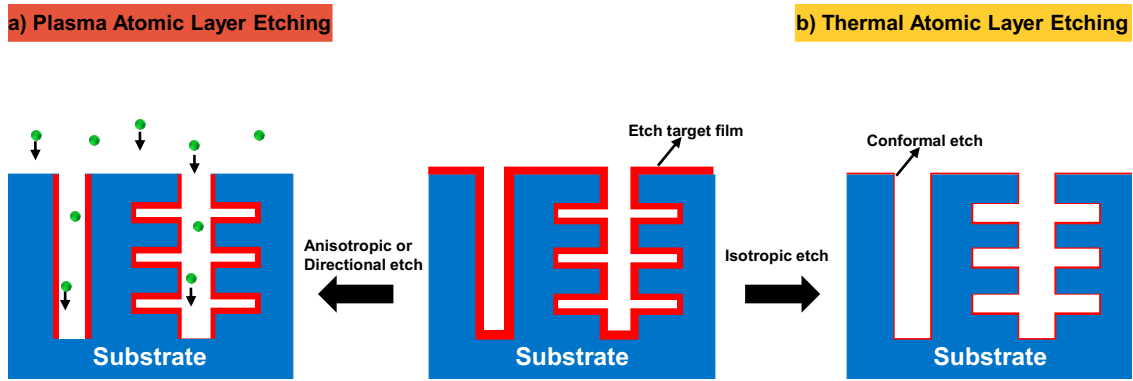


Figure 2.5: Illustration of isotropic and anisotropic etching (copyright 2022 © the author).

well as the lateral cavity. Thus, the overall result of ALEt is conformal etching as shown in Figure 2.5 b).

### 2.3.3 Selective etching

The choice and careful design of ALEt chemistries can also provide etch selectivity. Typically, different solid surfaces have different reactivity with various gaseous reactants. Several studies have reported that the different ligands involved in ligand-exchange reactions can lead to selective etching.<sup>44,61,67</sup> In addition, the lack of the energetic charged species in ALEt allows the development of highly selective etching processes. In the literature, various chemistries show different etching rates for different materials and the EPC can be further tuned by correctly setting additional process parameters such as etch temperature and partial pressures of the reactants. Moreover, combining ALD with ALE is being explored to allow selective deposition of one material over the other in a more efficient way.<sup>63,68</sup> Another interesting concept of rapid pulsing of the thermal energy to tune the etch selectivity among various materials is proposed.<sup>23,24</sup> Selective etching is desired to decrease the number of photolithographic steps and the associated manufacturing costs.

### 2.3.4 Minimal surface damage

Since ALEt does not involve any plasma-generated energetically charged or neutral species, the damage caused by these species to the sub-surface layers is avoided. Moreover, radiation-induced plasma damage is also absent in ALEt. However, surface contamination arising from either incomplete gas-surface reactions or diffusion of the atoms from the ALEt reactants into the bulk can deteriorate film properties. Nevertheless, the surface contamination can be chemically removed with an additional step in the ALEt process. For instance, it is reported that after ALEt of  $\text{Al}_2\text{O}_3$  and  $\text{SiO}_2$ , the surface F- and Cl-residuals are successfully hydrolysed using a water pulse above 325 °C.<sup>62,69</sup>



## 2.4 ALEt processes and mechanisms

Back in 2015, the concept and the need for thermal ALE (ALEt) was first proposed by the components research team of Intel in their report on industrial ALE perspective.<sup>16</sup> In the same year, an experimental proof of this concept was provided by George's group at the University of Colorado, Boulder.<sup>14,38,39</sup> They were able to perform ALEt of  $\text{HfO}_2$ ,  $\text{Al}_2\text{O}_3$  and  $\text{AlF}_3$  using self-limiting sequential reactions with  $\text{Sn}(\text{acac})_2$  and HF vapors. Over the past seven years, ALEt has developed rapidly both in industry as well as academia. Rapid development in ALEt has already shown its potential, and many materials such as metals and their oxides as well as nitrides can now be etched using novel chemistries.<sup>17</sup> With the continuous down scaling and implementation of 3D devices and complex integration schemes, the early prospects of ALEt being adopted by the fast changing semiconductor industry are looking bright.

In this section, Table 2.1 provides a brief summary of reported ALEt processes. Table 2.1 lists only ALEt processes that are thermally activated and utilize two or more sequential gas-surface reactions. It also excludes hybrid-ALEt processes that require any plasma step. More details on ALEt processes are described in the recent review articles.<sup>15,17,70-73</sup>

A typical ALEt process involves at least two steps to achieve the atomic etch precision. Several mechanisms that take place in ALEt have been reported<sup>15,70</sup> and can be broadly classified into surface modification and volatilization steps. In an ideal ALEt process, the surface modification and volatilization are performed by different reactants and are non-overlapping. The table highlights the reactants used for the surface modification and the volatilization steps in separate columns. The individual steps are briefly described next.

Table 2.1: Summary of reported ALEt processes. In the table, separate EPC values are reported for crystalline materials and are denoted by label (c-). The remaining EPC values are for amorphous materials. Alphabetically ordered by etch target. (last accessed: Oct. 2022)

Etch target	Reactants for surface modification	Reactants for volatilization	EPC [Å]	T <sub>etch</sub> [°C]	References
Al <sub>2</sub> O <sub>3</sub>	HF	TMA	0.6-2.5 @ 300 °C	>170	44,45,60,74,75
	HF	DMAC (Al[Me] <sub>2</sub> Cl)	1.2 @ 250 °C	>200	45,48,76
	HF	Sn(acac) <sub>2</sub>	0.23 @ 200 °C	≥ 150	44,77
	SF <sub>4</sub>	Sn(acac) <sub>2</sub>	0.2 @ 200 °C	≥ 150	77
	CHF <sub>3</sub>	TMA	0 @ 350 °C	-	69
	HF	SiCl <sub>4</sub>	0 @ 350 °C	-	44
	HF	BCl <sub>3</sub>	0.9 @ 290 °C	≥ 230	59
AlF <sub>3</sub>	HF	Sn(acac) <sub>2</sub>	0.63 @ 250 °C	≥ 150	14
(c-) AlN	HF	Sn(acac) <sub>2</sub>	0.36 @ 275 °C	275	78
(c-) AlN	XeF <sub>2</sub>	BCl <sub>3</sub>	0.19 @ 212 °C	≥ 212	62
AlN	HF	BCl <sub>3</sub>	> 0 @ 298 °C	> 200	62
Co	Cl <sub>2</sub>	Hhfac, Hacac	2 @ 140 °C	≥ 140	79
	O <sub>2</sub>	Hhfac	-	≥ 352	57
CoFeB	Cl <sub>2</sub>	Hacac	1.5 @ 150 °C	150	80
Cu	O <sub>2</sub>	Hhfac	0.9 (O <sub>2</sub> ) @ 275 °C	275	81
Cu	O <sub>3</sub>	Hhfac	84 @ 210 °C	> 127	58,81
Fe	Cl <sub>2</sub>	Hacac	50 @ 140 °C	> 135	82,83
Ga <sub>2</sub> O <sub>3</sub>	HF	BCl <sub>3</sub>	1.2 @ 200 °C	≥ 150	67
	HF	TMA	1.1 @ 250 °C	250	67
	HF	DMAC	1.3 @ 250 °C	250	67
	HF	TiCl <sub>4</sub>	0.82 @ 250 °C	250	67
	HF	Ga(NMe <sub>2</sub> ) <sub>3</sub>	0.21 @ 250 °C	250	67

Continued on next page

Table 2.1 – Continued from previous page

Etch target	Reactants for surface modification	Reactants for volatilization	EPC [Å]	T <sub>etch</sub> [°C]	References
	HF	Ga(Me) <sub>3</sub>	1 @ 300 °C	300	67
(c-)GaN	XeF <sub>2</sub>	BCl <sub>3</sub>	0.55 @ 195 °C	≥ 170	84
	HF	BCl <sub>3</sub>	0 @ 250 °C	-	84
	SF <sub>4</sub>	BCl <sub>3</sub>	0 @ 250 °C	-	84
HfO <sub>2</sub>	HF	TMA	0.1 @300 °C	300	44,61,76
	HF	DMAC	0.08 (c-); 0.68 @250 °C	≥ 200	44,61,76
	HF	TiCl <sub>4</sub>	0.02 (c-); 0.36 @250°C	250	61
	HF	SiCl <sub>4</sub>	0.05 @350 °C	350	44
	HF	Sn(acac) <sub>2</sub>	0.06 @200 °C	≥ 200	44
	SF <sub>4</sub>	DMAC	0 (c-); 0.5 @250 °C	250	61
	SF <sub>4</sub>	TiCl <sub>4</sub>	0.08 (c-); 0.7 @250 °C	250	61
	XeF <sub>2</sub>	TiCl <sub>4</sub>	1.26 (c-); 1.96 @250 °C	250	61
HfZrO <sub>2</sub>	HF	DMAC	0.16 (c-); 0.69 @250 °C	250	61
	HF	TiCl <sub>4</sub>	0.04 (c-); 0.35 @250 °C	250	61
	SF <sub>4</sub>	DMAC	0 (c-); 0.49 @250 °C	250	61
	SF <sub>4</sub>	TiCl <sub>4</sub>	0.25 (c-); 0.62 @250 °C	250	61
	XeF <sub>2</sub>	TiCl <sub>4</sub>	1.71 (c-); 2.07 @250 °C	250	61
InGaAs	HF	DMAC	0.24 @300 °C	> 250	85
InAlAs	HF	DMAC	0.62 @300 °C	> 250	85
Ni	SO <sub>2</sub> Cl <sub>2</sub>	PMe <sub>3</sub>	1.5 - 4.6 @175 °C	≥ 75	86
Si	O <sub>2</sub> , HF	TMA	0.2 - 0.4 @290 °C	≥ 225	87
Si <sub>3</sub> N <sub>4</sub>	O <sub>2</sub> , O <sub>3</sub> , HF	TMA	0.25 (O <sub>2</sub> ), 0.47 (O <sub>3</sub> ) @290 °C	≥ 210	88
SiO <sub>2</sub>	HF	TMA	0.3 @350 °C	> 300	69,74
	CHF <sub>3</sub>	TMA	0.1 @350 °C	> 350	69
TiN	O <sub>3</sub>	HF	0.2 @250 °C	≥ 150	89

Continued on next page

Table 2.1 – Continued from previous page

Etch target	Reactants for surface modification	Reactants for volatilization	EPC [Å]	T <sub>etch</sub> [°C]	References
	H <sub>2</sub> O <sub>2</sub>	HF	0.15 @250 °C	≥ 250	89
TiO <sub>2</sub>	WF <sub>6</sub>	BCl <sub>3</sub>	0.6 @170 °C	≥ 170	47
VO <sub>2</sub>	SF <sub>4</sub>	Sn(acac) <sub>2</sub>	0.3 @200 °C	200	77
	HF	Sn(acac) <sub>2</sub>	0.1 @200 °C	200	
W	O <sub>2</sub> , O <sub>3</sub> , BCl <sub>3</sub>	HF	2.56 @207 °C	≥ 128	20
	O <sub>2</sub> , O <sub>3</sub>	WF <sub>6</sub>	6.3 @300 °C	≥ 275	90
	O <sub>2</sub> , O <sub>3</sub>	WCl <sub>6</sub>	7.3 @205 °C	≥ 200	21
WO <sub>3</sub>	BCl <sub>3</sub>	HF	4.18 @207°C	≥ 128	20
ZnO	HF	TMA	(c-) 2 @265 °C	> 205	91
ZrO <sub>2</sub>	HF	TMA	0.01 @300 °C	250	44
	HF	TiCl <sub>4</sub>	0.26 (c-); 0.61 @250 °C	250	61
	HF	DMAC	0.82 (c-); 1.11 @250 °C	250	44,61
	SF <sub>4</sub>	TiCl <sub>4</sub>	0.36 (c-); 1.08 @250 °C	250	61
	HF	SiCl <sub>4</sub>	0.14 @350 °C	350	44
	SF <sub>4</sub>	DMAC	0.34 (c-); 0.46 @250 °C	250	61
	XeF <sub>2</sub>	TiCl <sub>4</sub>	1.75 (c-); 2.69 @250 °C	250	61
	HF	Sn(acac) <sub>2</sub>	0.14 @200 °C	≥ 200	44

### 2.4.1 Surface modification

The surface modification is a crucial step in ALEt where a part of the initial etch target surface layer is altered.<sup>15</sup> Depending on the number of elements in the etch target layer, in the surface modification step, the reactant(s) may either add or exchange element(s) with the etch target surface layer. In some cases, such as metal nitride or elemental (zero oxidation state) films, two subsequent surface modifications may be required. Often in surface modification, a change in the oxidation state of the elements in the etch target layer and an increase due to molar volume expansion in thickness are encountered.<sup>15,61</sup> Surface modification may involve oxidation, conversion, or halogenation reactions. These are briefly explained below with some examples.

- **Oxidation:** In oxidation, the substrate is exposed to either oxygen or halogen containing gaseous species.<sup>48</sup> The oxidation can be performed by gaseous O<sub>2</sub>, O<sub>3</sub>, H<sub>2</sub>O, Cl<sub>2</sub> (can be also considered as halogenation) etc.<sup>48</sup> This step is commonly employed to increase the oxidation state of the elements in the target films. Mostly in the metal containing volatile etch products, metals exist in higher oxidation states (> +2). The correct oxidation state is necessary to ensure the formation of stable and volatile etch products.<sup>15</sup> In an overall oxidation step, either oxygen or halogen atoms are added to the initial surface layer. The oxidation is usually accompanied by an increase in the total thickness. The oxidation step is critical for thermal etching of elemental (atoms with zero oxidation state) and some metal nitride films.

In the literature, the ALEt processes of elemental films such as Si, Ge, W, Co, Cu, Fe, Mo and Ni are reported and summarized in Table 2.1. Most Si compounds that are volatile have Si in the +4 oxidation state. Therefore in the first step, Si is converted to SiO<sub>2</sub> and then, the top SiO<sub>2</sub> layer is etched in a manner explained in the later paragraphs.

- **Conversion:** Another example of the surface modification is by chemical conversion.<sup>15</sup> In the conversion step, the etch target is exposed to reactants that convert the original metal oxide to another metal or non-metal oxides.<sup>15</sup> The conversion step may or may not involve a change in the oxidation state of the elements. In the conversion step, the altered surface layer is either more reactive than the original layer or is able to form stable and volatile etch products upon reacting with the second reactant in the volatilization step. The conversion step is important for films that would be otherwise etched spontaneously and therefore the intermediate conversion step is needed to control the etch per cycle. In addition, the conversion step is necessary for films that do not easily form volatile etch products. The examples of the etch target layers that require conversion steps are WO<sub>3</sub>, ZnO and SiO<sub>2</sub>.<sup>15</sup> The total film thickness can also change in this step.

ALEt of SiO<sub>2</sub> and ZnO involve slightly different etching mechanisms, where after TMA exposure, Al<sub>2</sub>O<sub>3</sub>/aluminosilicate (on SiO<sub>2</sub>) and Al<sub>2</sub>O<sub>3</sub>

(on ZnO) surfaces are left behind.<sup>74,91</sup> A part of ZnO is also etched during the TMA exposure in the form of  $\text{ZnMe}_2$  species.<sup>91</sup>

- **Halogenation:** The halogenation step involves the exposure of the etch target to halogen containing gases such as HF,  $\text{WF}_6$ ,  $\text{Cl}_2$ ,  $\text{SF}_4$ ,  $\text{XeF}_2$ , etc.<sup>48</sup> This step may involve a change in the oxidation state of the elements in the target films. Halogenation of metals is also an oxidation step, however, fluorination of metal oxides may not change the oxidation number of the metal atoms, e.g. aluminum exists as  $\text{Al}^{3+}$  in both the original layer ( $\text{Al}_2\text{O}_3$ ) and the fluorinated layer ( $\text{AlF}_3$ ).<sup>39</sup> For converting  $\text{Al}_2\text{O}_3$  to  $\text{AlF}_3$ , reagents like HF,  $\text{SF}_4$  and  $\text{CHF}_3$  are used at elevated temperatures ( $\geq 150$  °C). Similarly, other oxides such as  $\text{HfO}_2$ ,  $\text{Ga}_2\text{O}_3$ ,  $(\text{HfZr})\text{O}_2$  [HZO],  $\text{VO}_2$ , and  $\text{ZrO}_2$  are fluorinated using either HF,  $\text{SF}_4$ ,  $\text{XeF}_2$ , or  $\text{WF}_6$ . The existence of reactive but non-volatile metal fluorides such as  $\text{AlF}_3$ ,  $\text{HfF}_4$ ,  $\text{ZrF}_4$ , and  $\text{GaF}_3$ <sup>92</sup> is a prerequisite for a successful surface modification step by fluorination. At a given process conditions, the formed metal fluoride layer should act as a barrier for further reaction because in this way a self-limiting modification is achieved.<sup>93</sup> Other metal oxides such as  $\text{TiO}_2$ ,  $\text{V}_2\text{O}_5$ ,  $\text{Ta}_2\text{O}_5$ , and  $\text{WO}_3$  form volatile metal fluorides upon complete fluorination.  $\text{VF}_5$ ,  $\text{TaF}_5$ , and  $\text{WF}_6$  are all volatile above 200 °C while  $\text{TiF}_4$  sublimates at 284°C.<sup>39,92</sup>

The surface modification steps are not necessarily limited to the surface only, as there is some possibility of diffusion occurring deeper into more than several monolayers of the thin films.<sup>48,94,95</sup> Usually gas-solid reactions result in a concentration gradient of added atoms in a solid such as the top surface vs. sub-surface layers. This results in diffusion of added atoms from the surface toward the bulk of the solid.<sup>48,96</sup> The diffusion process is promoted at higher temperature, partial pressure of gas, time, and defects in the solids, and depends on the phase of the host material.<sup>48,58,75,96-99</sup> However, under given conditions, the in-diffused atoms can form a chemically modified layer that serves as a diffusion barrier<sup>96,100</sup> and hence, a self-limiting modification step is achieved.<sup>38,44,48,75,94,97</sup> Therefore, such diffusion assisted modification step may result in thicker modified layers that may show self-limiting behaviour. In addition, one can employ more than one surface modification step in ALEt.<sup>20,87,88</sup>

## 2.4.2 Volatilization

Volatilization is a process of turning the solid modified surface layer into gaseous species that are then released into the vacuum. In ALEt, the volatilization step follows the surface modification step. The actual removal happens when the modified layer is volatilized by the reactants or the temperature. Hence, this is defined as a volatilization step.<sup>38,39,49,101</sup> This step may involve ligand-exchange (including halide-exchange), chelation and adduct formation reactions with the species on the modified surfaces.<sup>15,102</sup> Volatilization usually occurs in a spontaneous fashion, i.e. it continues as long as the modified layer is present and stops when the original surface is revealed.<sup>15,48,81,103</sup> Therefore, the EPC in ALEt is dependent on the thickness

of the modified surface layer.<sup>48,75</sup> Various types of chemical reactions taking place during the volatilization step are briefly described below.

- **Ligand-exchange:** In the ligand-exchange, the ligands attached to the cations on the modified surface layer are exchanged with the ligands of the incoming gaseous reactants. This ligand-exchange causes atoms on the modified surface to form volatile species. Therefore, the modified surface is removed. An example of the ligand-exchange reaction is between gaseous TMA ( $\text{AlMe}_3$ ) molecules and  $\text{AlF}_x$  species on the modified surface which produces volatile products such as  $\text{AlMe}_2\text{F}$ ,  $\text{AlMe}_3\text{-AlMeF}_2$  and  $\text{AlMe}_2\text{F-AlMe}_2\text{F}$ .<sup>45,103</sup> The  $\text{AlF}_3$  layer can also be volatilized using reactants such as  $\text{AlMe}_2\text{Cl}$  and  $\text{Sn}(\text{acac})_2$ , which undergo ligand-exchange reactions with the surface bound ligands. As summarized in Table 2.1, for the metal oxides, reactants used for the ligand-exchange reactions are  $\text{AlMe}_3$ ,  $\text{AlMe}_2\text{Cl}$ ,  $\text{Sn}(\text{acac})_2$ ,  $\text{SiCl}_4$ ,  $\text{TiCl}_4$ ,  $\text{BCl}_3$ ,  $\text{GaMe}_3$  and  $\text{Ga}(\text{NMe}_2)_3$ .

In the case of  $\text{SiO}_2$ , the  $\text{AlMe}_3$  converts a part of the  $\text{SiO}_2$  layer to  $\text{Al}_2\text{O}_3$ /aluminosilicate layer. The converted layer is then fluorinated by HF to form  $\text{AlF}_3$ /silicate layer and is then volatilized using a subsequent  $\text{AlMe}_3$  pulse in the form of  $\text{AlF}_x\text{Me}_y$  and  $\text{SiF}_x\text{Me}_y$  species.<sup>74</sup> In the ZnO ALEt, the top ZnO layer is converted to  $\text{Al}_2\text{O}_3$  by  $\text{AlMe}_3$ . During the conversion step, the Zn from ZnO is volatilized in the form of  $\text{ZnMe}_2$  gaseous species. In a subsequent HF pulse, the  $\text{Al}_2\text{O}_3$  layer is fluorinated to  $\text{AlF}_3$  which is then volatilized during the  $\text{AlMe}_3$  pulse.

- **Chelation:** Volatilization by a chelation reaction with  $\beta$ -diketones such as Hacac, Hthd, and Hhfac is well reported in the literature.<sup>15,48,58,104</sup> For example, etching of copper and cobalt is performed using an oxidation-chelation reaction.<sup>79,81</sup> Co metal is first oxidized to  $\text{CoO}_x$  using  $\text{O}_2$ <sup>81</sup> or chlorinated to  $\text{CoCl}_x$  using  $\text{Cl}_2$ <sup>79</sup> and the volatilization of the modified layer is performed using either Hhfac or Hacac. The volatile species are proposed to be  $\text{CoCl}_x(\text{hfac})_y$ ,  $\text{Co}(\text{hfac})_2$ , HCl, and  $\text{H}_2\text{O}$ .<sup>15</sup> Similarly, Cu is first oxidized to  $\text{CuO}_x$  using either  $\text{O}_2$  or  $\text{O}_3$  and the volatilization step was performed using Hhfac.<sup>58</sup>
- **Adduct-formation:** Modified layers can also be volatilized using neutral electron donor species like  $\text{PMe}_3$ .<sup>86</sup> Ni surface is first modified to  $\text{NiCl}_2$  which is further reacted with  $\text{PMe}_3$  to form a volatile adduct  $\text{NiCl}_2(\text{PMe}_3)_2$ .

## 2.5 Challenges in ALEt

Like any other etching or deposition technique, ALEt comes with its own challenges<sup>7,15,105</sup> that are discussed here.

Despite its rapid development in the past seven years, ALEt faces many challenges. One of the key challenges is the use of strong fluorinating agents and the associated concerns about toxicity, contamination, and compatibility.<sup>106-108</sup> Compatibility concerns can arise from hardware, process integration, or both. In semiconductor industry, various

fundamental processes such as etching, deposition and cleaning utilize fluorine containing gases or solutions.<sup>109,110</sup> However, in ALEt and CVE, the use of strong fluorinating agents in their gaseous form at elevated temperatures (e.g. > 200 °C) is expected to enhance the corrosion of the processing equipment and its parts. To prevent such corrosion, various protection layers are required. From Table 2.1, it is clear that most ALEt processes utilize anhydrous or concentrated HF mixtures (such as HF:pyridine) and therefore, the storage and delivery of aggressive HF reactant has to be taken into account. Otherwise, one has to look for alternatives. Moreover, to mitigate the environmental impact of fluorinating agents, careful design and compatible scrubber systems are necessary.

In ALEt, the modification step may involve diffusion-assisted conversion that can pose challenges in achieving the uniform modification of crystalline materials. Diffusion of halide or oxide ions is usually faster along grain boundaries, and this can change the film properties and hence, can have a deteriorating effect.<sup>111-113</sup> Moreover, the grain boundary diffusion can impart contamination from the ALEt process chemistries into the bulk films. Isotropic etching of single crystalline materials is also challenging using ALEt. Etching of materials containing more than two elements can involve preferential etching of one atom over the others, thus, causing composition variation on the surface of the remaining films. Nevertheless, this can be sometimes mitigated using optimized etch chemistry, process parameters or choosing the hybrid-ALEt (plasma + thermal) approach. Furthermore, incomplete gas-surface reactions may leave contaminants that must be removed using extra steps, such as exposing the etched surfaces to H<sub>2</sub>O.<sup>62,69</sup>

Another challenge inherent to ALEt is slow processing, similar to that of ALD. In ALEt, especially of high-aspect 3D topologies as in VNAND structures long purges may be needed to minimize any overlap between surface modification and volatilization steps as well as to remove by-products efficiently, especially from the deep non-line-of-sight features.

Although the reported ALEt processes are capable of etching various metal oxides and nitrides, the list is by no means complete.<sup>15,17</sup> On the contrary, only a few metal ALEt processes have been reported so far. Therefore, a lot of effort would be needed to develop new metal ALEt processes.<sup>15</sup> There is also an increasing demand to develop ALEt processes that can be customized to etch one material over another, because the material selectivity is becoming increasingly important. Moreover, understanding of ALEt mechanisms is important to expand its scope to other materials and requires sophisticated analysis techniques such as in-situ spectroscopic ellipsometry, Fourier-transform infrared spectroscopy, mass spectroscopy, etc.<sup>40,47,74,88</sup>

Regardless of the above challenges, ALEt and its derivatives such as hybrid-ALEt have a huge potential in becoming a mainstream etch technology of the future.



# Chapter 3: Experimental techniques

## 3.1 Experimental setup

All etching experiments (details in the published articles [I, III, IV]) were performed using two similarly designed commercial reactors, of the Pulsar® type 2000 (P2000) manufactured by ASM Microchemistry Oy. Both apparatus are hot-wall, cross-flow type reactors, designed to process 200 mm silicon wafers. The main difference between the two reactors was that the one was made of titanium and the other one was made of nickel. The etching experiments using  $\text{NbF}_5$  and  $\text{CCl}_4$  chemistries were performed in the titanium-made P2000 reactor which was operated under isothermal conditions to a maximum  $T_{\text{etch}}$  of 460 °C. The other nickel-made P2000 was used for  $\text{SOCl}_2$  chemistry, operated at isothermal conditions. The maximum obtainable temperature of the nickel-made P2000 reactor was 370 °C. Both P2000 reactors had a corrosion protective coating of  $\text{SiO}_2$  to prevent any interaction between the etchant and the chamber walls. Using separate reactors to study different chemistries not only allowed parallel processing but avoided any overlap between different processes ( $\text{NbF}_5\text{-CCl}_4$  vs.  $\text{SOCl}_2$ ) which reduced maintenance costs. Prior to any etching, all target substrates were kept in the vacuum chamber for 5 minutes in order to ensure stabilization of the wafer surface temperature. The chamber pressure in all etch experiments was between 2 and 4 Torr.

For the SiGe etching experiments (described in article [II]) a home-built, warm wall, hot-stage, cross-flow reactor made of stainless steel was used, which was fitted with in-situ spectroscopic ellipsometer. The detailed experimental setup is described in the earlier report by Aziz et al.<sup>87</sup> The substrate temperature was varied from 225 to 290 °C while the reactor walls were kept at 160 °C.

## 3.2 Etch target thin films

Most etch-target thin films ( $\text{SiO}_2$ ,  $\text{Al}_2\text{O}_3$ ,  $\text{HfO}_2$  and  $\text{Si}_3\text{N}_4$ ) were deposited on p-type 200 mm silicon wafers with about 1.5 nm native oxide. However, TiN thin films were deposited on 22 nm thermally grown  $\text{SiO}_2$ . The  $\text{SiO}_2$  etch-target films were either 20 nm thermal  $\text{SiO}_2$  (TOx) grown at high temperature using an oxidation process<sup>114</sup> or 15 nm  $\text{SiO}_2$  grown in-house using the plasma enhanced atomic layer deposition (PEALD) technique.<sup>115</sup> High quality  $\text{Si}_3\text{N}_4$  films of about 30 nm in thickness were produced by Low Pressure Chemical Vapor Deposition (LPCVD).<sup>116</sup>

$\text{Al}_2\text{O}_3$  films were deposited at 300 °C by the trimethylaluminum (TMA) and water vapor ALD process.<sup>117</sup>  $\text{HfO}_2$  films were deposited at 300 °C by the hafnium tetrachloride ( $\text{HfCl}_4$ ) and water ALD process.<sup>118</sup> The thickness of the  $\text{HfO}_2$  films ranged from 25 to 40 nm. TiN films were deposited on 22 nm thermal oxide at 400°C by thermal ALD process utilizing  $\text{TiCl}_4$  and  $\text{NH}_3$ .<sup>119</sup>

The TiN films used in these etch experiments were 10 to 50 nm in thickness. TiN grown without an air break was also subjected to the etching experiments.

About 100 nm SiGe films grown by physical vapor deposition (PVD) were supplied by Hionix Inc. Rutherford backscattering spectrometry (RBS) revealed their composition to be  $\text{Si}_{0.15}\text{Ge}_{0.85}$  [II]. For simplicity, we use the SiGe notation throughout the thesis. The SiGe films were deposited on 100 nm  $\text{SiO}_2$  covered Si substrates.

### 3.3 Etchants and process gases

The etchants used for the ALEt of  $\text{Al}_2\text{O}_3$ , TiN,  $\text{HfO}_2$ ,  $\text{Si}_3\text{N}_4$  and  $\text{SiO}_2$  were  $\text{NbF}_5$ ,  $\text{CCl}_4$ , and  $\text{SOCl}_2$ . For the SiGe etching, the etchants were HF, TMA, and the oxidizing agents were  $\text{O}_3/\text{O}_2$  and  $\text{O}_2$ .

$\text{NbF}_5$  ( $\geq 99.5\%$  pure) is a solid powder and was purchased from abcr GmbH, (Germany). Despite being solid,  $\text{NbF}_5$  has sufficient vapor pressure (about 0.1 Torr at  $45\text{ }^\circ\text{C}$ <sup>120</sup>). Therefore, the  $\text{NbF}_5$  vessel was kept at  $45\text{-}50\text{ }^\circ\text{C}$  and  $\text{N}_2$  as an inert carrier gas was used to transport the  $\text{NbF}_5$  vapors into the reaction chamber, commonly known as vapor-push mode. The gas-transport line was kept at  $70\text{ }^\circ\text{C}$  to prevent any condensation in the lines. There was no needle valve in the delivery line of  $\text{NbF}_5$  because of its low vapor pressure. A particle filter was installed in the  $\text{NbF}_5$  delivery line to avoid blowing the precursor particles into the chamber and onto the wafer surface.

$\text{CCl}_4$  (anhydrous,  $\geq 99.5\%$ ) was bought from Merck KGaA (Germany). The  $\text{CCl}_4$  vessel was held at room temperature.  $\text{CCl}_4$  has high vapor pressure of about 90 Torr at  $20\text{ }^\circ\text{C}$ <sup>121</sup> and was therefore delivered by the vacuum-draw mode with a needle valve attached at the delivery line to control its dose.

$\text{SOCl}_2$  was supplied by Seastar Chemicals Inc. (Canada), with ultra-high purity ( $> 99.9999\%$ ) and extremely low metal contamination ( $< 1\text{ ppb}$ ). Since it has a sufficiently high vapor pressure of about 93 Torr at  $20\text{ }^\circ\text{C}$ ,<sup>122</sup> the vessel was kept at room temperature.  $\text{SOCl}_2$  was delivered by the vacuum-draw mode and the dose was controlled by a needle valve.

For both the inert gas purges and the carrier gas (for the vapor-push mode in the case of  $\text{NbF}_5$ ), nitrogen was used. Purge gas flows were controlled by needle valves. The purity of the carrier gas was 5.0 (99.999 %) and it was further purified by an Entegris purifier to a 6.0 ( $\geq 99.9999\%$ ) purity level.

For the SiGe etching, HF from an HF-pyridine solution (70 % by wt. and purchased from Sigma-Aldrich) was used. The HF-pyridine source vessel (gold coated from inside to prevent any corrosion) was kept at room temperature. TMA bought from Sigma-Aldrich was kept at room temperature. The high purity  $\text{N}_2$  (6.0) was used as a carrier as well as purge gas. The oxygen used was an industrial grade, supplied by Airgas and the same was fed into the ozone generator from O3ONIA, Switzerland. The  $\text{O}_3$  concentration was about  $220\text{ g/cm}^3$ .

## 3.4 Film characterization techniques

Several techniques such as spectroscopic ellipsometry (SE), weighing balance, resistivity mapping (ResMap), X-ray photoelectron spectroscopy (XPS), X-ray reflectivity (XRR), X-ray diffraction (XRD), and transmission electron microscopy (TEM) were employed to characterize the ALEt processes.

For the thicknesses and the optical constants of  $\text{Al}_2\text{O}_3$ , TiN,  $\text{HfO}_2$ ,  $\text{Si}_3\text{N}_4$  and  $\text{SiO}_2$  thin films, an SE-800 spectroscopic ellipsometer from SENTECH Instruments GmbH, (Germany) was used. In contrast, the SiGe ALEt was monitored using an in-situ SE tool from J.A. Woollam Co. (model: M-2000 UI).

The removed thickness, phase, surface roughness, and density of the films were measured by XRR/XRD. For that, an Xpert PRO MRD X-ray diffractometer from Malvern Panalytical Ltd (United Kingdom) was used. For consistency, the center points of the wafers were chosen as the measurement spots.

An SAG 204 balance from Mettler Toledo with a resolution of about 0.1 mg was used for weight measurements. The EPC and the removed thickness values were extracted by using a simple mass-density-volume relationship, as previously described.<sup>123</sup>

Transmission electron microscopy was executed by Evans Analytical Group (EAG), California. For the imaging an FEI Tecnai TF-20 FEG/TEM operated at 200 kV was used in the bright-field TEM mode. For the sample preparation, an in-situ focused ion beam (FIB) lift-out technique on an FEI Dual Beam FIB/SEM was used. Prior to the ion milling, the samples were carbon coated followed by sputtering iridium on top. The thickness of the TEM lamella was about 100 nm.

In articles [I, II, IV], the surface compositions as well as the elemental depth profiles were determined with the help of XPS. The XPS system used here was a K-Alpha<sup>+</sup> from Thermo Scientific<sup>TM</sup>. The Al- $K\alpha$  (1486.6 eV / 15 kV) X-ray source was used with a spot size of 400  $\mu\text{m}$ . In the XPS depth profile measurements, an argon ion energy for sputtering was set to 1 keV. For the high resolution survey scan, a total of 10 scans were performed with a pass energy of 200 eV, and an increment of 0.5 eV. Quantification of the atomic concentrations was performed on Thermo Advantage data analysis software (v5.9921) which utilized the relative sensitivity factors (RSF) from its library. The RSF values for Ti2p<sub>3</sub>, N1s, O1s, C1s, Si2p<sub>3</sub>, Cl2p(2p<sub>3</sub>), F1s, Nb3d<sub>5</sub> and Al2p are 4.4, 1.7, 2.9, 1.0, 0.6, 2.7(1.8), 4.1 and 0.6, respectively. The binding energies of the elements were calibrated using a reference C1s signal peaked at 284.6 eV.

For the  $\text{HfO}_2$  etching, surface composition investigations were performed with XPS using PHI Quantera SXM equipment. Monochromatic Al- $K\alpha$  (1486.6 eV/15 kV) X-rays at a take-off angle of 45° were used. The analysis chamber pressure was  $3 \times 10^{-6}$  Pa. In the depth profile measurements, the argon ion energy was set at 1 keV and the X-ray spot size was 100  $\mu\text{m}$ . The pass energy of 140 eV was used. The detection limit of this particular tool is about 0.1 - 0.5 atomic percent.

### 3.5 Computational chemistry

The basic thermodynamic calculations for various chemical reactions discussed in articles I, II, and section 4.5.2 were performed using HSC software. The DFT (density functional theory) investigations discussed in the article [III] were carried out by Dr. Simon D. Elliot, while the computations in the article [IV] were performed by Dr. Suresh Kondati Natarajan together with Dr. Simon D. Elliot.

In section 4.1 and article [III], the Schrödinger's Materials Science Suite<sup>124</sup> was used to perform the DFT investigation of the etch mechanism. The atomic-scale surface models and the gaseous molecules were created and optimized under periodic boundary conditions with the Perdew-Burke-Ernzerhof (PBE) functional.<sup>125</sup> PBE approximations are universally applied to both molecules and solids, including metals.<sup>126</sup> Moreover, the relative quantities such as energy differences, bond length changes, and frequency shifts are studied more accurately with PBE.<sup>126</sup> The PBE ultrasoft pseudopotentials<sup>127</sup> and Monkhorst-Pack  $k$ -point sets<sup>128</sup> were implemented in the Quantum ESPRESSO code,<sup>129,130</sup> more details are discussed by Suresh et al.<sup>131</sup> Reaction energies  $\Delta E$  for possible surface conversions by the reactants were calculated using DFT.

The Gibbs free energy of a system at any time and given temperature  $T$  is defined as:

$$G = H - TS \quad (3.1)$$

where  $H$  is the enthalpy and  $S$  is the entropy of the system. Most likely, the etching is driven by the entropy and therefore in order to accurately determine the changes in the Gibbs free energies ( $\Delta G$ ), the effect of temperature ( $T$ ) and reactant ( $P_r$ ) as well as product ( $P_p$ ) pressures must be considered.<sup>93</sup> Thus, the change in the Gibbs free energy for ideal gases at constant volume is given by 3.2:<sup>93</sup>

$$\Delta G = \Delta H - T\Delta S + RT\ln\left(\prod P_p^{np} / \prod P_r^{nr}\right), \quad (3.2)$$

$$\Delta H = \Delta E + \Delta ZPE + \Delta W(T), \quad (3.3)$$

where the number of gaseous molecules in the reactant and the product states are given by 'nr' and 'np', respectively.  $R$  is the gas constant. As defined in 3.3,  $\Delta H$  includes the electronic energy ( $\Delta E$ ) of the system at 0 K, the zero point energy change ( $\Delta ZPE$ ) and a contribution from the temperature dependent enthalpy change ( $\Delta W(T)$ ).<sup>93</sup> If  $\Delta G$  is  $< 0$  the reaction is said to be exergonic (favourable), otherwise it is endergonic (unfavourable).<sup>93</sup>

In article [III], for the etchants  $P_r$  of 0.1 Torr is used. In an equilibrium,  $P_p = sP_r$  is assumed. In contrast, the sticking coefficient ' $s$ ' is an unknown reactant parameter and is generally in the range  $10^{-2}$  to  $10^{-4}$  for ALD precursors<sup>132</sup> and here the value of ' $s$ ' used is  $10^{-3}$ .

For the TiN etching described in [IV], the quantum chemical computations were performed on Vienna Ab initio Simulation Package (VASP v5.3).<sup>133,134</sup> The

'freeh' tool in the TURBOMOLE suite<sup>135</sup> and the Phonopy code<sup>136</sup> were used to obtain  $H$  as well as  $S$  for the gaseous and the bulk systems. The  $P_p$  is not controlled in an etch reactor and it is typically much lower than the  $P_r$  and the  $P_p$  of 0.01 Torr was chosen for our calculations.



## Chapter 4: Results and discussion

In this chapter, key findings obtained during the course of this PhD study are summarized. Section 4.1 discusses the etching of  $\text{Al}_2\text{O}_3$  and is based on publication [III]. TiN etching is detailed in the sections 4.2 and 4.3, and the findings are published in the articles [I, IV]. In the section 4.4, a summary of SiGe etching is provided which is covered in the article [II]. The section 4.5 is dedicated to an unpublished work on  $\text{HfO}_2$  etching. Finally, in section 4.6 the activation energies for various etch processes are determined using Arrhenius plots.

### 4.1 $\text{Al}_2\text{O}_3$ etching by $\text{NbF}_5\text{-CCl}_4$

Amorphous  $\text{Al}_2\text{O}_3$  was etched by alternate exposures of  $\text{NbF}_5$  and  $\text{CCl}_4$  vapors at elevated temperatures (380 - 460 °C). This section discusses the predicted etching mechanism as investigated using the first-principles density functional theory (DFT) implemented in the Schrödinger's Materials Science Suite.<sup>124</sup> Enthalpies and Gibbs free energies that include the effect of temperature as well as reactant pressure for several reactions were also calculated. The main results of the etching experiments of  $\text{Al}_2\text{O}_3$  are reported in 4.1.2.

#### 4.1.1 DFT investigations of the etch-mechanism

For the alumina surface, the  $\theta\text{-Al}_2\text{O}_3$  ( $\bar{2}01$ ) periodic slab model was used. The ions in this polymorph have similar coordination environment as those in the amorphous as-deposited  $\text{Al}_2\text{O}_3$ .<sup>137</sup> Based on the stability, a  $2 \times 1$  expansion of a 3-layer ( $\bar{2}01$ ) slab was selected as a representative surface model and is described in [III].

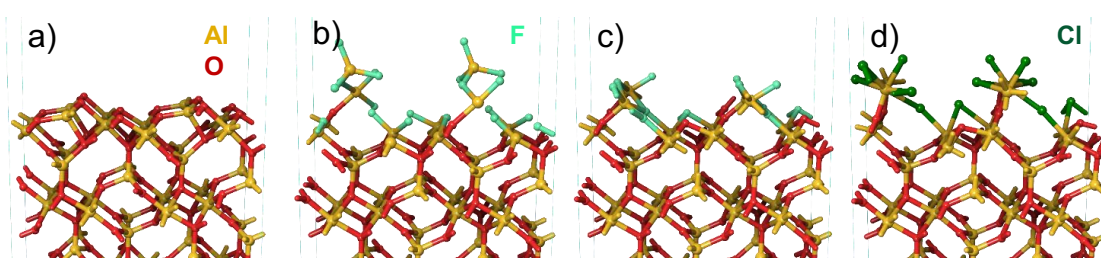



Figure 4.1: Structural models optimized with DFT for (a) bare  $\text{Al}_2\text{O}_3$  surface with 0% halides, (b) surface covered with 166%-F, (c) 100%-F, (d) 100%-Cl. Reproduced from [III], Copyright © 2021 Authors, Published by American Chemical Society, distributed under a Creative Commons (CC BY 4.0 ) License.

Figure 4.1 a) depicts the bare  $\theta\text{-Al}_2\text{O}_3$  surface. In Figures 4.1 b)-d), the halide (F or Cl) covered surfaces were generated by replacing an oxide dianion ( $\text{O}^{2-}$ ) with two halide monoanions ( $\text{F}^-$  or  $\text{Cl}^-$ ) in the topmost layer of

the  $\text{Al}_2\text{O}_3$  slab, in order to keep the stoichiometry and charge neutrality. The maximum level of chlorination was determined to be 3 Cl per 4-coordinate Al (i.e. 12 Cl per  $2 \times 1$  cell), and this is designated as 100%-Cl covered  $\text{Al}_2\text{O}_3$  surface. Higher Cl coverages led to the spontaneous desorption of  $\text{AlCl}_3$  molecules during the optimization step. On the contrary, because  $\text{AlF}_3$  is practically non-volatile (sublimes above  $1000\text{ }^\circ\text{C}$ )<sup>92,138</sup> at temperatures below  $500\text{ }^\circ\text{C}$ , fluorinated  $\text{Al}_2\text{O}_3$  can reach up to 166%-F (i.e. 20 F per  $2 \times 1$  cell). This excess fluorination is energetically favourable and creates structural motifs similar to  $\text{AlF}_3$ . In the DFT studies, inter-conversions between the fluorinated (166%-F and 100%-F), chlorinated (100%-Cl) and bare 0% alumina surfaces as shown in Figure 4.1 were investigated (more details in [III]).

The DFT simulations were targeted to predict the etching mechanism. Numerous reactions and by-products are possible, and the goal was to identify surface transformations that are thermodynamically favourable at the process conditions. The simulations can reveal the saturated surface after each exposure of the reactant during the etching cycle and the corresponding EPC values. In reality, etching is a non-equilibrium process which is controlled by the reaction kinetics. Moreover, because of the continuous removal of by-products from the reactor, the desorption of the by-products from the surface becomes an irreversible process. Detailed study on the surface adsorbates, intermediates, reaction pathways and associated reaction kinetics with DFT is beyond the current scope and can be studied in the future. The reactions computed here are concluded to be thermodynamically feasible if  $\Delta G < 0$  at a given temperature. These feasible reactions may still face a high kinetic barrier and therefore, are not necessarily observed on the experimental timescale. Due to the lack of kinetic data, the assumption is that for a family of competing reactions, the kinetic barriers scale with the reaction energies, and therefore the most feasible reaction is likely to be the most kinetically favourable one.

In an ALEt process, the gaseous reactants interact with the target surface, one at a time. However, during the individual reactant exposure steps, surface-bulk diffusion may also take place. The net effect of a cycle is the removal of  $\text{Al}_2\text{O}_3$  layer and regeneration of surface functionalities. During the surface-bulk diffusion, the surface adsorbates can penetrate into the bulk of the film and cause various effects such as conversion/fluorination, structural reorganization, etching, etc. Therefore, the most simple yet a valid way to assess the viability of ALEt is to compute the bulk etching thermodynamics.

Initially, the thermodynamic favourability of the reactions between either reactant and the bulk alumina was considered (more details are given in [III]).  $\text{NbF}_5$  reacts with aluminum oxide according to the reaction **R1** in Table 4.1 and the DFT calculation yields  $\Delta E = +140\text{ kJ/mol-NbF}_5$  and  $\Delta G^{300\text{ }^\circ\text{C}} = -100\text{ kJ/mol-NbF}_5$ . This highly positive  $\Delta E$  means the reaction is highly endothermic but favourable due to the large negative change in the Gibbs free energy.

However, according to the reaction **R7** in Table 4.1, the bulk alumina is more readily etched by  $\text{CCl}_4$  alone. For **R7**  $\Delta E = -18\text{ kJ/mol-Al}_2\text{O}_3$  and  $\Delta G^{300\text{ }^\circ\text{C}} = -248\text{ kJ/mol-Al}_2\text{O}_3$ . However, no etching was observed experimentally with  $\text{CCl}_4$  alone (Figure. 4.3 a)), which can mean that the kinetic barriers are not

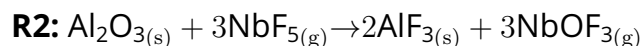


Table 4.1: The DFT computed reaction thermodynamics for potential half-reactions during the NbF<sub>5</sub> pulse (reactions R1-R6) and CCl<sub>4</sub> pulse (R7-R14), as well as the overall etching cycle (R15). Bulk solid is labelled (s), gas-phase molecules (g) and coverage is indicated as a percentage for surface slabs. Reproduced from [III], Copyright © 2021 Authors, Published by American Chemical Society, distributed under a Creative Commons (CC BY 4.0 ) License.

R. No.	Reaction	$\Delta E$	$\Delta G^{100^\circ\text{C}}$	$\Delta G^{200^\circ\text{C}}$	$\Delta G^{300^\circ\text{C}}$	$\Delta G^{600^\circ\text{C}}$	units
<b>R1</b>	Al <sub>2</sub> O <sub>3(s)</sub> + 3NbF <sub>5(g)</sub> → 2AlF <sub>3(g)</sub> + 3NbOF <sub>3(g)</sub>	139.9	-10.2	-54.6	-100.1	-241.4	$\frac{\text{kJ}}{\text{mol}(\text{NbF}_5)}$
<b>R2</b>	Al <sub>2</sub> O <sub>3(s)</sub> + 3NbF <sub>5(g)</sub> → 2AlF <sub>3(s)</sub> + 3NbOF <sub>3(g)</sub>	-24.1	-47.4	-52.5	-57.5	-71.7	$\frac{\text{kJ}}{\text{mol}(\text{NbF}_5)}$
<b>R3</b>	0%-slab + 6NbF <sub>5(g)</sub> → 100%F-slab + 6NbOF <sub>3(g)</sub>	-26.8	-50.1	-55.3	-60.3	-74.5	$\frac{\text{kJ}}{\text{mol}(\text{NbF}_5)}$
<b>R4</b>	100%-slab + 4NbF <sub>5(g)</sub> → 166%F-slab + 4NbOF <sub>3(g)</sub>	0.8	-22.4	-27.6	-32.6	-46.8	$\frac{\text{kJ}}{\text{mol}(\text{NbF}_5)}$
<b>R5</b>	100%Cl-slab + 16NbF <sub>5(s)</sub> → 166%F-slab + 12NbClF <sub>4(g)</sub> + 4NbOF <sub>3(g)</sub>	-44.9	-80.4	-91.1	-102.1	-136.0	$\frac{\text{kJ}}{\text{mol}(\text{NbF}_5)}$
<b>R6</b>	100%Cl-slab + 12NbF <sub>5(s)</sub> → 100%F-slab + 12NbClF <sub>4(g)</sub>	-60.1	-99.7	-112.3	-125.3	-165.7	$\frac{\text{kJ}}{\text{mol}(\text{NbF}_5)}$
<b>R7</b>	Al <sub>2</sub> O <sub>3(s)</sub> + 3CCl <sub>4(g)</sub> → 2AlCl <sub>3(g)</sub> + 3COCl <sub>2(g)</sub>	-17.7	-164.1	-206.0	-248.4	-372.9	$\frac{\text{kJ}}{\text{mol}(\text{CCl}_4)}$
<b>R8</b>	Al <sub>2</sub> O <sub>3(s)</sub> + 3CCl <sub>4(g)</sub> → 2AlCl <sub>3(s)</sub> + 3COCl <sub>2(g)</sub>	-62.8	-74.2	-74.1	-73.4	-62.8	$\frac{\text{kJ}}{\text{mol}(\text{CCl}_4)}$
<b>R9</b>	0%-slab + 6CCl <sub>4(g)</sub> → 100%Cl-slab + 6COCl <sub>2(g)</sub>	-40.1	-51.6	-51.5	-50.7	-40.2	$\frac{\text{kJ}}{\text{mol}(\text{CCl}_4)}$
<b>R10</b>	100%F-slab + 12CCl <sub>4(g)</sub> → 100%Cl-slab + 12CFCl <sub>3(g)</sub>	72.5	51.4	46.2	41.0	25.7	$\frac{\text{kJ}}{\text{mol}(\text{CCl}_4)}$
<b>R11</b>	100%F-slab + 12CCl <sub>4(g)</sub> + (2/3)Al <sub>2</sub> O <sub>3(s)</sub> → 66%Cl-slab + 12CFCl <sub>3(g)</sub> + (4/3)AlCl <sub>3(g)</sub>	72.5	28.9	16.7	4.3	-33.5	$\frac{\text{kJ}}{\text{mol}(\text{CCl}_4)}$
<b>R12</b>	166%F-slab + 20CCl <sub>4(g)</sub> + (4/3)Al <sub>2</sub> O <sub>3(s)</sub> → 100%Cl-slab + 20CFCl <sub>3(g)</sub> + (8/3)AlCl <sub>3(g)</sub>	71.5	23.3	9.7	-4.1	-46.4	$\frac{\text{kJ}}{\text{mol}(\text{CCl}_4)}$
<b>R13</b>	100%F-slab + 12CCl <sub>4(g)</sub> + 2Al <sub>2</sub> O <sub>3(s)</sub> → 0%-slab + 12CFCl <sub>3(g)</sub> + 4AlCl <sub>3(g)</sub>	83.7	-4.9	-31.1	-57.9	-140.6	$\frac{\text{kJ}}{\text{mol}(\text{CCl}_4)}$
<b>R14</b>	166%F-slab + 20CCl <sub>4(g)</sub> + (10/3)Al <sub>2</sub> O <sub>3(s)</sub> → 0%-slab + 20CFCl <sub>3(g)</sub> + (20/3)AlCl <sub>3(g)</sub>	78.2	-10.4	-36.6	-63.4	-146.2	$\frac{\text{kJ}}{\text{mol}(\text{CCl}_4)}$
<b>R15</b>	Al <sub>2</sub> O <sub>3(s)</sub> + 3NbF <sub>5(g)</sub> + 6CCl <sub>4(g)</sub> → 2AlCl <sub>3(g)</sub> + 3NbOF <sub>3(g)</sub> + 6CFCl <sub>3(g)</sub>	421.8	-62.6	-194.2	-329.1	-747.6	$\frac{\text{kJ}}{\text{mol}(\text{Al}_2\text{O}_3)}$

breached. Furthermore, DFT simulations show that the  $\text{CCl}_4$  molecule does not adsorb efficiently on a bare surface of alumina. Hence, after considering **R1** and **R7**, the single-etchant reactions are excluded, and only reactions that remove either Al or O, but not Al and O simultaneously are considered. This is the key requirement for a successful self-limiting ALEt process.

Now, according to **R2**, the conversion of bulk alumina into solid aluminum fluoride is as follows.

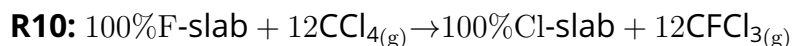


For **R2**, the computed  $\Delta E = -24$  kJ/mol-NbF<sub>5</sub> and  $\Delta G^{300^\circ\text{C}} = -58$  kJ/mol-NbF<sub>5</sub> (Table 4.1).

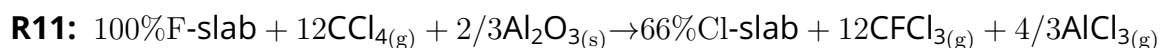
Moreover, **R3** shows the conversion of the bulk alumina surface into a 100%-fluorinated surface, which in terms of thermodynamics is similar to **R2** (for **R3**:  $\Delta E = -27$  kJ/mol-NbF<sub>5</sub> and  $\Delta G^{300^\circ\text{C}} = -60$  kJ/mol-NbF<sub>5</sub>). However when compared to **R3**, the additional fluorination of the surface is less but still favourable (e.g. **R4**:  $\Delta E = +0.8$  kJ/mol-NbF<sub>5</sub> and  $\Delta G^{300^\circ\text{C}} = -33$  kJ/mol-NbF<sub>5</sub> for fluorination from 100%F to 166%F). This indicates that the surface conversion does not self-limit when the fluorination reaches 100%F. This is consistent with the experimental findings discussed in the section 4.1.2.

In a nutshell, the DFT calculations show that the continuous fluorination of alumina into aluminum fluoride is favourable under experimental conditions. Though, the degree to which the actual conversion takes place is dependent on the kinetics of reactions between NbF<sub>5</sub> and bulk Al<sub>2</sub>O<sub>3</sub>. Therefore, it is proposed that the conversion step is determined by the kinetics of diffusion at the Al<sub>2</sub>O<sub>3</sub>-AlF<sub>3</sub> interface. The prolonged NbF<sub>5</sub> exposure therefore fluorinates not only the surface layer but possibly the sub-surface layers as is experimentally verified in Figures 4.3 b) and 4.4.

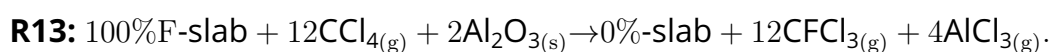
Next, possible reactions are investigated between the fluorinated surfaces (100%F- and 166%F-slabs) and the gaseous CCl<sub>4</sub>. According to the DFT calculations, the energetically most favoured products are CFCI<sub>3</sub> and AlCl<sub>3</sub> as shown in Table 4.1 (more details in [III]). CFCI<sub>3</sub> is likely the product of a halide-exchange reaction between CCl<sub>4</sub> and the fluorinated surface:



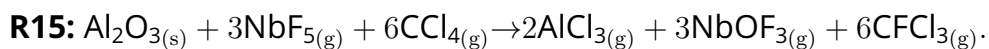
which is endoergic across a wide temperature range ( $\Delta G^{300^\circ\text{C}} = +41$  kJ/mol-CCl<sub>4</sub>). The reaction becomes more favourable when Al is simultaneously etched away as AlCl<sub>3</sub>, as shown by **R11** with computed  $\Delta G^{300^\circ\text{C}} = +4.3$  kJ/mol-CCl<sub>4</sub> for partial etching:



and  $\Delta G^{300^\circ\text{C}} = -58$  kJ/mol-CCl<sub>4</sub> for complete etching to a bare surface as shown by **R13**.



Finally, a highly favourable ( $\Delta G^{300\text{ }^\circ\text{C}} = -329\text{ kJ/mol-CCl}_4$ ) overall ALEt reaction is obtained:



According to **R15**, the etch products of Al<sub>2</sub>O<sub>3</sub> ALEt are most likely the gaseous AlCl<sub>3</sub>, NbOF<sub>3</sub> and CFCl<sub>3</sub>.

**Etch per cycle:** The DFT calculations predicted a theoretical EPC of 1.2 Å for 100%F-slab coverage, according to **R13**. However, for prolonged fluorination as in **R4** and **R5**, an EPC of 1.7 Å is achieved as per **R14**. In the etching experiments, an EPC of 1.5 Å was recorded for 3.0 s NbF<sub>5</sub> and CCl<sub>4</sub> pulse lengths (Figure 4.2), which is consistent with a coverage of about 120%F for etching following **R15**.

Within the experimented range, the etch temperature is the most critical parameter that affects the EPC. At higher temperatures (i.e.  $\geq 380\text{ }^\circ\text{C}$ ), higher EPC values were recorded. No etching was observed at temperatures below 380 °C. The DFT calculations did not show any reasons for this behaviour. Therefore, the temperature dependence is likely due to the kinetics of diffusion and structural reorganization at the Al<sub>2</sub>O<sub>3</sub>-AlF<sub>3</sub> interface. After examining the DFT computed structures, it is pointed out that the atoms near the surface have to reorganize so that aluminum takes a low coordination number (i.e. 4 at the surface rather than 6 in bulk) which is a pre-requisite for the volatilization to occur.

#### 4.1.2 Etching experiments

Al<sub>2</sub>O<sub>3</sub> ALEt was investigated by measuring changes in the EPC in response to various process parameters. The parameters that were considered to have an impact on the EPC are etching temperature, NbF<sub>5</sub> and CCl<sub>4</sub> pulse times. 6.0 s long N<sub>2</sub> purge steps were introduced after each reactant exposure. Partial pressures of the reactants were difficult to control and were not included in the study. Both reactant pulse times were varied from 0.5 to 3.0 s and the etch temperature from 380 to 460 °C.

**Effect of reactant pulse times:** Figure 4.2 a) shows that the EPC increases with increasing NbF<sub>5</sub> pulse time when the rest of the parameters are fixed. The fixed parameters are the etch temperature, pressure, source temperatures, number of etch cycles, the CCl<sub>4</sub> pulse time and the both purge times. In Figure 4.2 a) an EPC of 1.5 Å at 3.0 s NbF<sub>5</sub> pulse time is noted. EPC response with varying NbF<sub>5</sub> pulse time shows no saturation up to 3.0 s. An increase in the EPC with the NbF<sub>5</sub> pulse time can be explained by diffusion-assisted fluorination of the Al<sub>2</sub>O<sub>3</sub> surface that does not self-limit to a monolayer, which is consistent with the DFT calculation. In addition, the increase of EPC could also be due to an increase surface roughness, however, the surface roughness did not significantly increase when measured by AFM (see Figure 4.6).

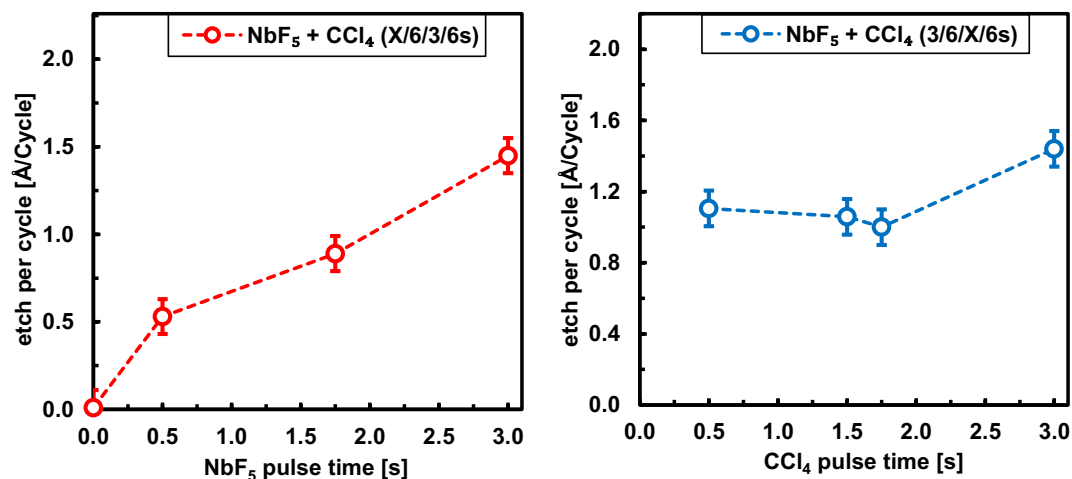


Figure 4.2: An etch per cycle of Al<sub>2</sub>O<sub>3</sub> with varying: a) NbF<sub>5</sub> pulse time, and b) CCl<sub>4</sub> pulse time. The etch temperature was fixed to 460 °C while each purge time was set to 6.0 s. For every data point a total of 150 etch cycles were performed. Reproduced from [III], Copyright © 2021 Authors, Published by American Chemical Society, distributed under a Creative Commons (CC BY 4.0) License.

Figure 4.2 b) shows an EPC of about 1.1 Å for CCl<sub>4</sub> pulse times between 0.5 and 1.75 s and 1.4 Å for 3.0 s CCl<sub>4</sub> pulse time. This could indicate the self-limiting nature of the removal step that is limited by the amount of AlF<sub>x</sub> available at the surface for CCl<sub>4</sub> to react with. The increase in the EPC at 3.0 s CCl<sub>4</sub> pulse time can be due to insufficient purging of CCl<sub>4</sub> molecules resulting in CVE type of reaction due to partial overlap between the NbF<sub>5</sub> and CCl<sub>4</sub> pulses in the reactor.

**Effect of Temperature:** Figure 4.3 a) displays the EPC values at various temperatures for Al<sub>2</sub>O<sub>3</sub> (blue or red), SiO<sub>2</sub> (yellow) and Si<sub>3</sub>N<sub>4</sub> (green) films. The figure shows that Al<sub>2</sub>O<sub>3</sub> was etched only by the binary chemistry, i.e. NbF<sub>5</sub> - CCl<sub>4</sub> (red curve). CCl<sub>4</sub> alone is unable to etch Al<sub>2</sub>O<sub>3</sub> (blue curve) within 380 - 460 °C, as was also confirmed by XPS, XRR/D, SE and TEM (see Figure 4.5). SiO<sub>2</sub> and Si<sub>3</sub>N<sub>4</sub> were not etched by the binary process or either of the single reactant. This provides the etch selectivity: the binary process removes Al<sub>2</sub>O<sub>3</sub> but neither the SiO<sub>2</sub> nor the Si<sub>3</sub>N<sub>4</sub> from the same substrate. Moreover, no significant etching of Al<sub>2</sub>O<sub>3</sub>, SiO<sub>2</sub> or Si<sub>3</sub>N<sub>4</sub> was observed at temperatures below 380 °C.

To study the extent of fluorination and verify the DFT prediction, an excessive fluorination step was performed. At 460 °C, 150 and 850 NbF<sub>5</sub> pulses, and at 400 °C, 150 and 900 NbF<sub>5</sub> pulses of 3.0 s length were delivered on Al<sub>2</sub>O<sub>3</sub> films. Each NbF<sub>5</sub> pulse was separated by 6.0 s N<sub>2</sub> purge step, to ensure the regeneration of NbF<sub>5</sub> vapors in the source vessel. Afterwards, the thicknesses of the formed AlF<sub>x</sub>[O] layers was measured using SE (Figure 4.3 b). Upon prolonged fluorination, a significant part of Al<sub>2</sub>O<sub>3</sub> was converted to an AlF<sub>x</sub>[O] layer. The figure shows the self-limiting nature of the fluorination step and the temperature dependence that shows the fluorination likely

involves diffusion of fluoride ions. The excessive fluorination was further confirmed by XPS (see Figure 4.4 a)) and the prolonged fluorination leads to thicker AlF<sub>x</sub>[O] layer which greatly exceeds its monolayer thickness.

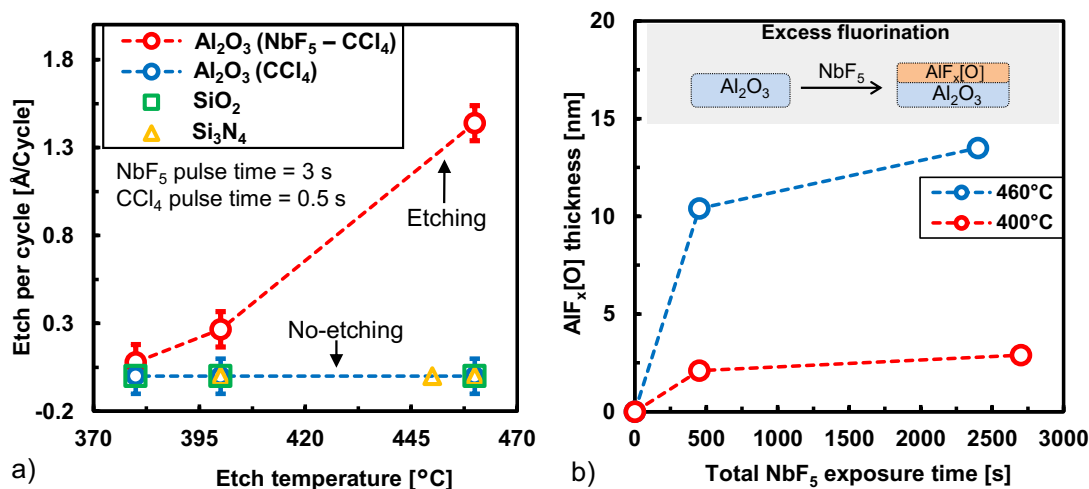


Figure 4.3: a) EPC vs. etch temperature for Al<sub>2</sub>O<sub>3</sub>, SiO<sub>2</sub> and Si<sub>3</sub>N<sub>4</sub> substrates. The substrates were exposed to either NbF<sub>5</sub> - CCl<sub>4</sub>, or CCl<sub>4</sub> only, or NbF<sub>5</sub> only reactants. The NbF<sub>5</sub> and CCl<sub>4</sub> pulse times were fixed to 3.0 s and 0.5 s, respectively. b) AlF<sub>x</sub>[O] layer thickness with total NbF<sub>5</sub> exposure time. The N<sub>2</sub> purge times were kept constant at 6.0 s, each. Reproduced from [III], Copyright © 2021 Authors, Published by American Chemical Society, distributed under a Creative Commons (CC BY 4.0) License.

The molar mass of Al<sub>2</sub>O<sub>3</sub> is 102 g/mol and its bulk density is 3.9 g/cm<sup>3</sup>. Therefore, the molar volume of Al<sub>2</sub>O<sub>3</sub> is 26.2 cm<sup>3</sup>/mol. Similarly, the molar volume of crystalline AlF<sub>3</sub> is calculated to be 28.9 cm<sup>3</sup>/mol.<sup>139,140</sup> Thus, the volume expansion upon fluorination is expected to be 10%. Similar expansion upon fluorination of ZrO<sub>2</sub> and HfO<sub>2</sub> is described by Murdzek et al.<sup>61</sup>

In most thermal ALEt processes reported so far, there is no ALEt window<sup>15,38,44,48,74,75,88</sup> and the EPC is observed to be dependent on the partial pressure<sup>74,75,88</sup> and temperature.<sup>38,44,89</sup> Similarly, from our findings it is evident that there is no ALEt window. On the contrary, there are only a few ALEt processes that exhibit an ALEt window such as ALEt of HfO<sub>2</sub>,<sup>38</sup> TiO<sub>2</sub><sup>47</sup> and TiN.<sup>89</sup>

### 4.1.3 Post-etch film characterization

To further understand the etch mechanism, the post-etched and the fluorinated Al<sub>2</sub>O<sub>3</sub> layers were studied with ex-situ XPS. XPS depth profile of about 11 nm thick AlF<sub>x</sub>[O] is plotted in Figure 4.4 a). After a surface cleaning step (15 s of sputtering), a high amount of fluorine of about 55 atomic % is detected. Similar F (about 52 atomic %) content was reported by Kim et al. after fluorinating Al<sub>2</sub>O<sub>3</sub> with CF<sub>4</sub>/O<sub>2</sub> plasma and the AlF<sub>x</sub>[O] layer was estimated to be a few nm (> 2 nm, exact values were not reported) in thickness.<sup>141</sup> Park et al. used F-beam and F<sup>-</sup> ions to fluorinate Al<sub>2</sub>O<sub>3</sub> and obtained 5 nm thick AlF<sub>x</sub>[O] layers with 32 atomic % F.<sup>142</sup> For comparison,

Cano et al. used HF as the fluorinating agent at 300 °C and reported 10 atomic % F for 0.6 nm thick fluorinated layers<sup>75</sup> On the other hand, in Figure 4.4 a) a decreased oxygen content of 17 atomic % (about 60 atomic % of O in bulk  $\text{Al}_2\text{O}_3$ ) is observed. A gradual decrease in the F content with sputter time indicates a composition gradient in the  $\text{AlF}_x[\text{O}]$  layer. This gradient points in the direction of diffusion based fluorination step as discussed earlier in section 2.4.1. Moreover, a very low Nb content of about 1 atomic % is found on the surface. From these depth profiles, it can be said that  $\text{NbF}_5$  efficiently performs the conversion step, in accordance with the reaction **R2**.

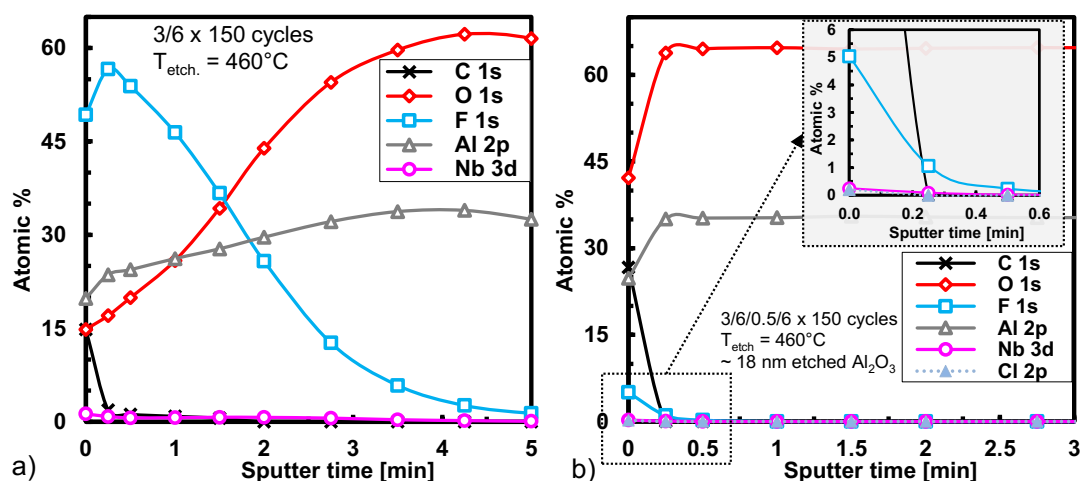



Figure 4.4: XPS depth profiles of a)  $\text{Al}_2\text{O}_3$  exposed to  $\text{NbF}_5$  for a total of 450 s at 460 °C, b)  $\text{Al}_2\text{O}_3$  remaining after removing about 18 nm film by the  $\text{NbF}_5$  -  $\text{CCl}_4$  ALEt process. A zoomed figure at the top right corner focuses on Nb, F and Cl signals. Reproduced from [III], Copyright © 2021 Authors, Published by American Chemical Society, distributed under a Creative Commons (CC BY 4.0 ) License.

Figure 4.4 b) shows the depth profile of the remaining  $\text{Al}_2\text{O}_3$  film after 150 ALEt cycles at 460 °C. The inset of the figure depicts an F- content around 5 atomic % and extremely small amounts of Nb (< 0.3 atomic %) or Cl (< 0.2 atomic %). The small amount of remnant surface F may be the result of incomplete reactions with  $\text{CCl}_4$ , and therefore pulse times longer than 0.5 s are needed to either completely remove the converted layer or complete the halide-exchange reaction.

Cross-sectional bright-field TEM images of  $\text{Al}_2\text{O}_3$  on silicon substrate are shown in Figure 4.5. Initially, 56 nm thick  $\text{Al}_2\text{O}_3$  film was used as an etch target. Figure 4.5 a) shows the  $\text{Al}_2\text{O}_3$  film after exposing it for 150 times to 3.0 s long  $\text{CCl}_4$  pulses. The figure shows no etching by  $\text{CCl}_4$  and the surface appears smooth. On the other hand, Figure 4.5 b) shows the remaining 39.3 nm thick  $\text{Al}_2\text{O}_3$  film after 150 cycles of the  $\text{NbF}_5$  -  $\text{CCl}_4$  ALEt process. After etching about 18 nm of  $\text{Al}_2\text{O}_3$ , the remaining film appears to be slightly rougher than the unetched film. The increase in the surface roughness can be due to either variation in the diffusion depths or reorganization of the near-surface region during the fluorination (SE and XPS in Figure 4.4 b) show



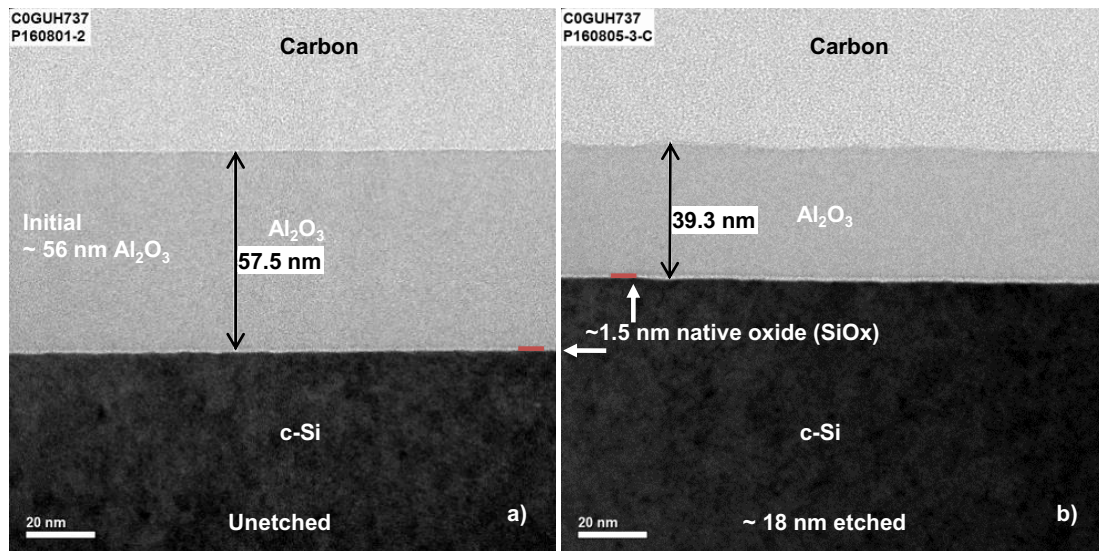



Figure 4.5: Cross-sectional bright-field transmission electron microscope (BF-TEM) images of a) unetched 57.5 nm (includes 1.5 nm native silicon oxide)  $\text{Al}_2\text{O}_3$  film after exposing it for 150 times to 3.0 s  $\text{CCl}_4$  pulses, and b) after etching about 18 nm  $\text{Al}_2\text{O}_3$  film by 150 cycles of the  $\text{NbF}_5$  -  $\text{CCl}_4$  ALEt process. Initially, about 56 nm  $\text{Al}_2\text{O}_3$  was measured by SE. The  $\text{NbF}_5$  and  $\text{CCl}_4$  pulse times were 3.0 s and 0.5 s, respectively. For both experiments, an etch temperature of 460 °C was used. Reproduced from [III], Copyright © 2021 Authors, Published by American Chemical Society, distributed under a Creative Commons (CC BY 4.0 ) License.

≈ 1.3 nm thick fluorinated layer). The etched surface does not appear to be crystalline.

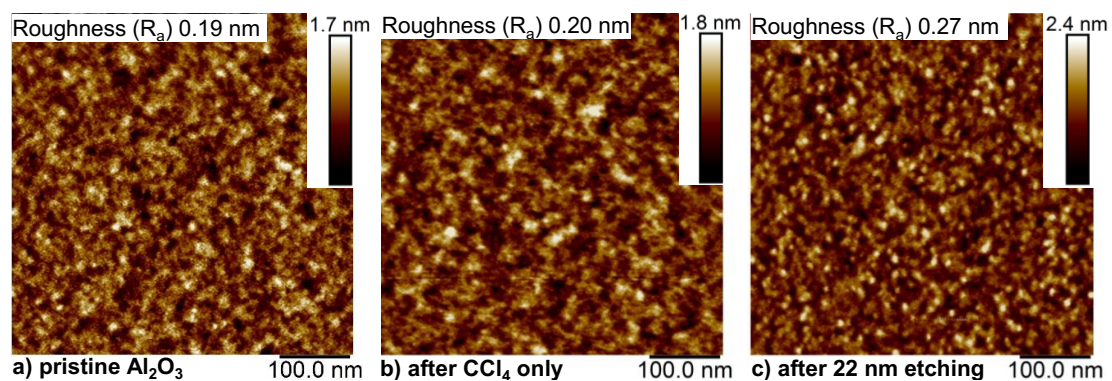



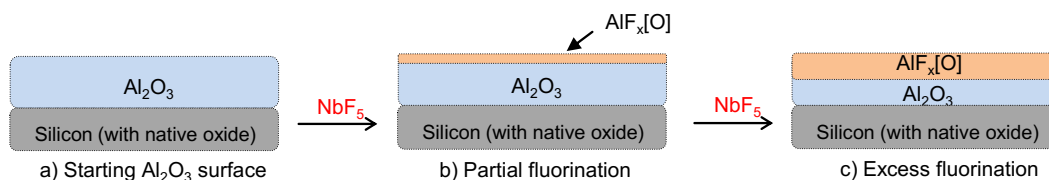
Figure 4.6: Surface morphology by AFM of a) about 56 nm unetched  $\text{Al}_2\text{O}_3$ , b) after 150 3.0 s long  $\text{CCl}_4$  pulses, c) after etching about 22 nm  $\text{Al}_2\text{O}_3$  by the  $\text{NbF}_5$  -  $\text{CCl}_4$  process at 460 °C. Reproduced from [III], Copyright © 2021 Authors, Published by American Chemical Society, distributed under a Creative Commons (CC BY 4.0 ) License.

To investigate the surface morphology, AFM was performed on about 56 nm pristine aluminum oxide film, the same film after 150 pulses of 3.0 s  $\text{CCl}_4$  (no etching observed), and after removing about 22 nm of  $\text{Al}_2\text{O}_3$  by the  $\text{NbF}_5$  -  $\text{CCl}_4$  ALEt process (Figure 4.6). The AFM images do not show a significant

increase in the surface roughness after the  $\text{CCl}_4$  pulses. However, consistent with the TEM image, a slight increase in the roughness was observed after the etching.

#### 4.1.4 Reaction mechanism

**Step 1: Conversion/Fluorination** -  $\text{NbF}_5(\text{g})$  fluorinates the  $\text{Al}_2\text{O}_3$  surface



**Step 2: Volatilization** -  $\text{CCl}_4(\text{g})$  reaction with  $\text{AlF}_x[\text{O}]$  surface

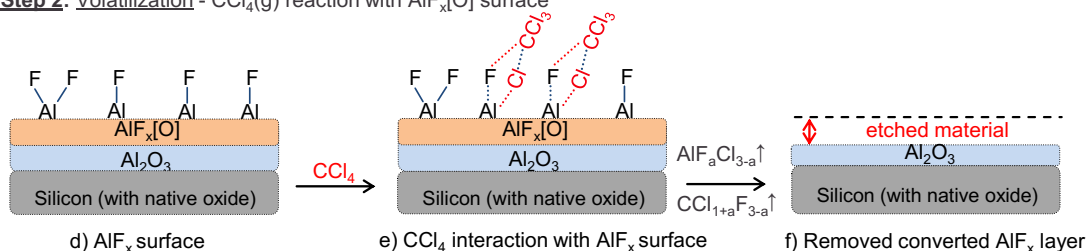



Figure 4.7: The proposed etch mechanism: where step 1 is a fluorination step and step 2 is the volatilization step. The volatilization step shows a possible halide-exchange interaction between  $\text{CCl}_4$  and the  $\text{AlF}_x[\text{O}]$  surface. Adapted from [III], Copyright © 2021 Authors, Published by American Chemical Society, distributed under a Creative Commons (CC BY 4.0 ) License.

After analysing the DFT and experimental results, a two-step cyclic ALEt mechanism is proposed as shown in Figure 4.7. In the first step, the gaseous  $\text{NbF}_5$  fluorinates or converts the  $\text{Al}_2\text{O}_3$  surface into an  $\text{AlF}_x[\text{O}]$  layer. In the second step, the converted layer is removed by the  $\text{CCl}_4$  molecules. There are numerous reports describing a two-step ALEt mechanism that is coined as the conversion-etch mechanism.<sup>39,40,47,74,88,91</sup>

In the conversion step, the initial  $\text{Al}_2\text{O}_3$  film on the silicon substrate is converted to the fluorinated  $\text{Al}_2\text{O}_3$  layer (i.e.  $\text{AlF}_x[\text{O}]$ ) upon exposure to the  $\text{NbF}_5$ , as depicted in Figure 4.7 b).  $\text{NbF}_5$  works as a fluorinating agent similar to  $\text{HF}$ <sup>39</sup> and  $\text{WF}_6$ .<sup>47</sup> The DFT and experimental findings suggest that this step is not self-limiting, and with prolonged fluorination a thicker (more than a monolayer)  $\text{AlF}_x[\text{O}]$  layer is formed, as depicted in Figure 4.7 c) and is evident from Figure 4.4 a) (more details in the supplementary information of [III]). DFT also suggests that niobium is volatilized in the form of  $\text{NbOF}_3$  and the existence of gaseous  $\text{NbOF}_3$  has been previously verified.<sup>120,143–146</sup> In the conversion step, oxygen from the  $\text{Al}_2\text{O}_3$  layer is etched away at least partially if not completely and thus the converted layer is labelled as  $\text{AlF}_x[\text{O}]$ . Figures 4.7 c) and d) depict an excessively fluorinated surface and are consistent with the findings shown in Figures 4.3 b) and 4.4 a).

In the second step, the volatilization of the converted  $\text{AlF}_x[\text{O}]$  layer takes place as shown in Figures 4.7 d) to f). The volatilization proceeds via halide-



exchange and forms gaseous by-products ( $AlF_aCl_{3-a}$  and  $CCl_{1+a}F_{3-a}$ , where  $0 \leq a \leq 2$ ). The DFT computations revealed that  $AlCl_3$  and  $CFCl_3$  are the most favourable etch products.

## 4.2 TiN etching by NbF<sub>5</sub>-CCl<sub>4</sub> or CCl<sub>4</sub> alone

There are two types of TiN etching processes explored here. The first one includes exposing TiN surface sequentially to NbF<sub>5</sub> and CCl<sub>4</sub> reactants in a cyclic manner (ALET). The second etching process is based on pulsing of a single etchant, i.e. CCl<sub>4</sub> in a chemical vapor etching (CVE) or gas-phase pulse etching (GPPE) mode [as in articles I, IV]. Every etchant exposure was followed by an inert gas (N<sub>2</sub>) purge step to ensure that the excess etchant molecules and etch-products are removed from the reactor. In section 4.2.1, the thermochemistry of the etching process as well as overall etch reactions are covered. Later, the experimental findings are discussed in sections 4.2.2 - 4.2.4.

### 4.2.1 Computational chemistry

First the interactions between the TiN surface and each reactant are studied with the help of ab-initio simulations to predict the adsorption steps, and later the thermodynamics of the potential etching reactions are discussed. The scope of the DFT was limited to the adsorption and prediction of thermodynamically favoured etching reactions only. Therefore, mechanisms involved in the formation and desorption of all possible volatile species with all potential reaction pathways were not investigated.

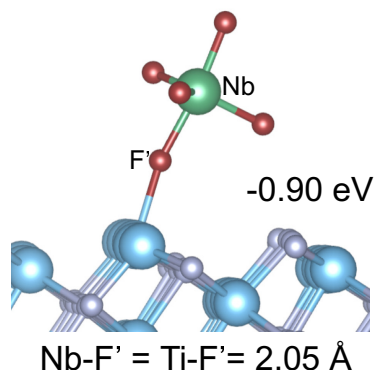


Figure 4.8: DFT computed intact adsorption of NbF<sub>5</sub> molecule on TiN (2 1 1) surface at 0 K. The green and red colours are for niobium and fluorine atoms, respectively. The blue and grey colours are for Ti and N atoms, respectively. Reproduced with permission from Paper [IV], Copyright ©2021 John Wiley and Sons.

**Fluorination pulse:** Figure 4.8 shows a NbF<sub>5</sub> molecule interacting with the TiN (2 1 1) surface. The reactive TiN (2 1 1) surface with step defects was chosen because it represents ALD grown TiN with its typical columnar grain boundaries.<sup>147,148</sup> In the optimized NbF<sub>5</sub> molecule geometry with minimum energy, not all the Nb-F bonds are equal in length. The gas phase NbF<sub>5</sub> molecule has five F atoms that are bonded to Nb, three F atoms in the equatorial plane (with each Nb-F bond length of 1.85 Å) and two F atoms that are on each side of the polar axis (each Nb-F bond is 1.88 Å). A similar

optimized geometry of  $\text{NbF}_5$  molecule is reported in another DFT study, where three angles  $\angle(\text{F-Nb-F})$ s are equal (equatorial  $\angle(\text{F-Nb-F}) = 120^\circ$ ) and each Nb-F distance in the equatorial plane is 1.84 Å while the Nb-F distance in the polar axis is 1.88 Å.<sup>149</sup> The polar axis is an axis passing through the F' and the opposite F atom in Figure 4.8. In every gaseous  $\text{NbF}_5$  molecule, these two Nb-F bonds are longer, weaker and polar in nature as compared to the equatorial Nb-F bonds. Therefore, the  $\text{NbF}_5$  molecules favourably bind to the Ti atoms on the step edges via these polar F atoms. The newly formed Ti-F bond length is 2.05 Å. It was found that the  $\text{NbF}_5$  molecule does not adsorb dissociatively at 0 K, as shown in Figure 4.8, probably due to a kinetic barrier. In the gas phase, in order for the homolytic dissociation of  $\text{NbF}_5$  to take place, high energies of 7.3 or 9.9 eV are required to remove one or two F ligands, respectively.

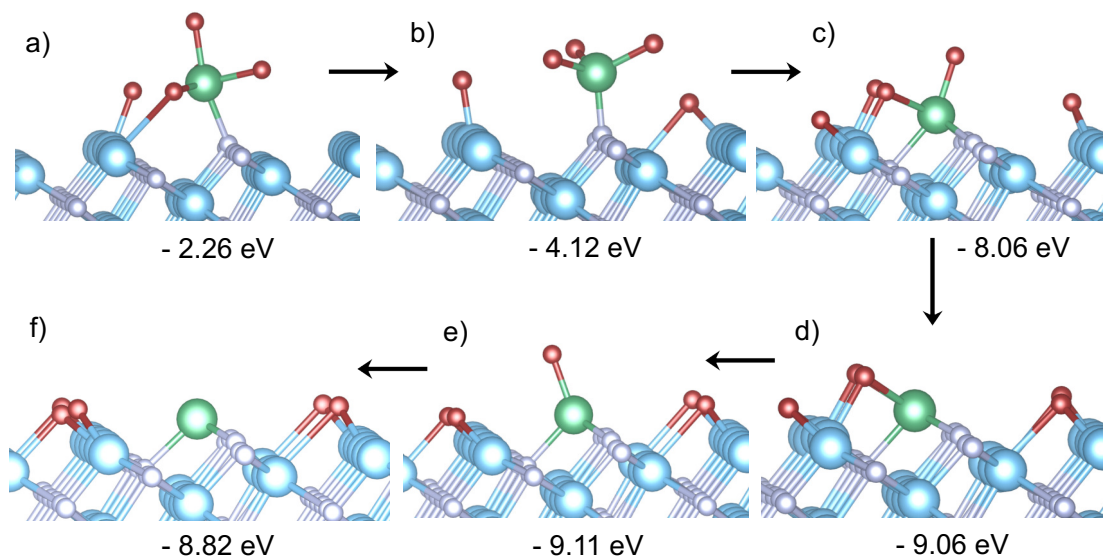


Figure 4.9: Minimum energy geometries of a TiN(2 1 1) surface undergoing an adsorption of a single  $\text{NbF}_5$  molecule. These geometries are extracted from the MD simulation performed at 400 K. Reproduced with permission from Paper [IV], Copyright ©2021 John Wiley and Sons.

On the TiN surface, the Nb-F bonds will break at elevated temperature as shown above. At 400 K, a short 5 ps MD simulation at DFT level was performed and the snapshots of the geometries which attained minimum energies are presented in Figure 4.9. A continuous decrease in the binding energy, from -0.90 eV to -9.11 eV is observed with increasing number of Nb-F bonds broken and Ti-F bonds formed on the surface. Figure 4.9 e) displays the most favourable geometry where Nb is coordinated with three surface N atoms and one F atom pointing away from the surface. This predicts that  $\text{NbF}_5$  dissociates at 400 K on the stepped TiN(2 1 1) surface leaving the surface covered by Nb-N, Nb-F and Ti-F species after the fluorination step. As seen in Figure 4.9 f), a full dissociation of the  $\text{NbF}_5$  molecule is shown to be less favourable than the geometries shown in Figure 4.9 d) and e).

Last, the TiN(2 1 1) surface saturated with many  $\text{NbF}_5$  molecules is shown in Figure 4.10. The predicted saturated TiN surface corresponds to a  $\text{NbF}_5$  coverage of 2.3 molecules/ $\text{nm}^2$ . For simplicity, the Nb and F covered TiN

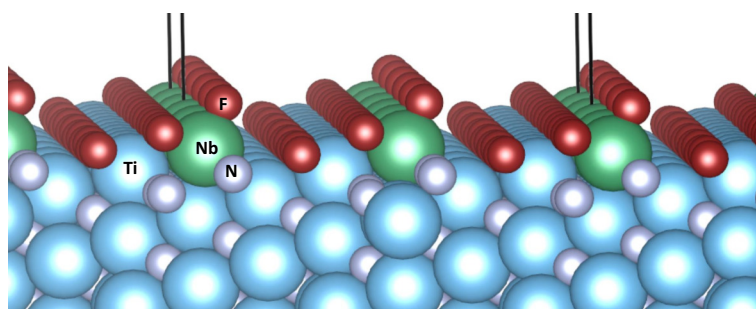


Figure 4.10: Minimum energy geometry of the TiN(2 1 1) surface saturated with adsorbed NbF<sub>5</sub> molecules at 400 K. Reproduced with permission from Paper [IV], Copyright ©2021 John Wiley and Sons.

surface is denoted as Nb<sub>x</sub>F<sub>y</sub> covered TiN surface which stops further reaction with NbF<sub>5</sub>, thus resulting in a self-limiting surface reaction. In the later sections, the experiments show that NbF<sub>5</sub> alone is unable to etch TiN. The surface area in Figure 4.10 is larger than the surface area shown in Figure 4.9 e). In the figure, each Nb atom is bonded to at least one F atom that is not shared with either nearest Ti or other neighbouring Nb atoms.

**Chlorination pulse:** The above described saturated surface after the fluorination step, as shown in Figure 4.11 a), is used for the CCl<sub>4</sub> adsorption. The MD simulations show that, at 0 K, CCl<sub>4</sub> does not bind strongly to the Nb<sub>x</sub>F<sub>y</sub> covered TiN surface due to a repulsion between the Cl atoms and the F atoms on the surface. Figure 4.11 a) depicts the favourable geometry

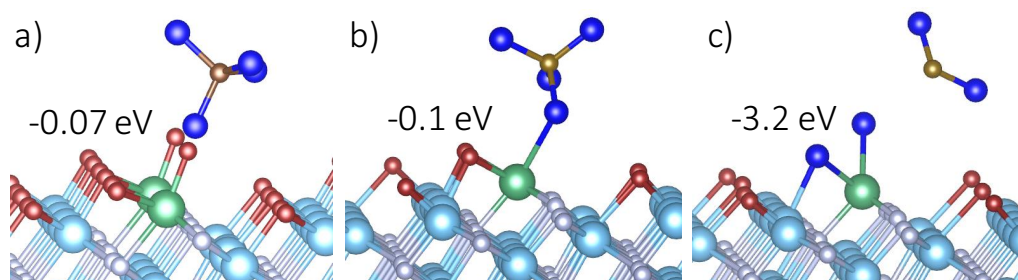


Figure 4.11: A minimum energy geometry of intact CCl<sub>4</sub> adsorbed at the Nb<sub>x</sub>F<sub>y</sub> covered TiN surface at 0 K. Reproduced with permission from Paper [IV], Copyright ©2021 John Wiley and Sons.

(binding energy -0.07 eV) where one Cl from CCl<sub>4</sub> is directed towards the Nb atom at the surface. On the contrary, in the other configurations where the chlorine atoms are directed towards the surface Ti/F atoms, the CCl<sub>4</sub> molecule does not physisorb. This proposes that the Nb sites are important for CCl<sub>4</sub> to interact with the Nb<sub>x</sub>F<sub>y</sub> covered TiN surface and the resulting relaxed geometries are shown in Figures 4.11 b) and c). In Figure 4.11 b) a slightly favourable binding between the Cl and Nb atoms is shown, which results in weakening of the Nb-F bonds. Furthermore, a strong adsorption of CCl<sub>4</sub> is observed at Nb sites when the Nb atom is free of Nb-F bonds.

**Continuous etching:** For the CVE mode, it was found that the CCl<sub>4</sub> molecule spontaneously dissociates on the bare TiN at 0 K. After donating one Cl ligand to the surface the rest of the molecule departs to the vacuum as CCl<sub>3</sub> fragment. This spontaneous dissociation suggests that CCl<sub>4</sub> reacts strongly with the bare TiN surface. A 3 ps long MD simulation at DFT level resulted in CCl<sub>4</sub> adsorption on the bare TiN surface. After just 0.74 ps of MD simulation, three Ti-Cl surface bonds and a surface bound ClCN (the proposed reaction product) were formed. From the DFT it is proposed that CCl<sub>4</sub> is able to spontaneously react with the bare TiN surface, resulting in a continuous etching.

**Overall ALEt cycle:** On the basis of the DFT simulations, TiN is proposed to undergo a self-limiting surface reaction with NbF<sub>5</sub> during the first pulse followed by the adsorption of CCl<sub>4</sub> catalyzed by the Nb sites in the second pulse, leading to the etching of TiN via sequential exposures of NbF<sub>5</sub> and CCl<sub>4</sub>.

**Thermochemistry of overall etch reactions:** Table 4.2 shows Gibbs free energies for potential overall etch reactions. The reactant pressure of 2.5 Torr and the product pressure of 0.01 Torr were used. In the table, the  $\Delta G$  values are given only for the etch temperatures where the etching actually takes place (more details in the SI of [IV]). In Table 4.2, the reactions for bulk TiN etching are shown to form various by-products. Niobium and titanium can take various oxidation states in their stable forms and hence many combinations of volatile by-products are possible. For practical reasons, only a small representative set of by-product combinations is considered.

Table 4.2: Potential overall etch reactions where bulk TiN is converted into gaseous products upon reacting with NbF<sub>5</sub> and CCl<sub>4</sub> molecules. **R2**, **R4** and **R5** (shown in bold font) are redox reactions. All species other than TiN are in gas phase. P<sub>p</sub> at  $\Delta G=0$  is the product pressure at 740 K that will bring the reaction to equilibrium at a constant reactant pressure of 2.5 Torr. A low P<sub>p</sub> value indicates that the reaction products are unlikely and vice-versa. Reproduced with permission from Paper [IV], Copyright ©2021 John Wiley and Sons.

Reactions	$\Delta G$ [eV]		P <sub>p</sub> [Torr] at $\Delta G=0$ ; T=740 K
	640 K	740 K	
R1:TiN + NbF <sub>5</sub> + CCl <sub>4</sub> $\longrightarrow$ TiCl <sub>3</sub> + NbNFCl + CF <sub>4</sub>	2.8	2.5	7.3E-14
<b>R2</b> :TiN + NbF <sub>5</sub> + CCl <sub>4</sub> $\longrightarrow$ TiCl <sub>4</sub> + NbNF + CF <sub>4</sub>	3.3	2.9	1.5E-15
R3:TiN + NbF <sub>5</sub> + CCl <sub>4</sub> $\longrightarrow$ TiCl <sub>3</sub> + NbClF <sub>4</sub> + CNF	-1.2	-1.6	3.8E+00
<b>R4</b> :TiN + NbF <sub>5</sub> + CCl <sub>4</sub> $\longrightarrow$ TiCl <sub>4</sub> + NbF <sub>4</sub> + CNF	-0.8	-1.2	1.4E-01
<b>R5</b> :TiN + NbF <sub>5</sub> + CCl <sub>4</sub> $\longrightarrow$ TiF <sub>4</sub> + NbFCl <sub>3</sub> + ClCN	-2.7	-3.1	3.8E+05

R1 and **R2** in Table 4.2 are not thermodynamically favoured due to large positive changes in the Gibbs free energies at 640 K (370 °C) and 740 K (470 °C). The only favourable reactions near the etch conditions are R3, **R4**, and

**R5**, with **R5** being the most likely one, purely based on the large negative  $\Delta G$  value. For R3 at 400 K, the DFT predicted etch per cycle is 0.57Å. In the redox reactions i.e. **R2**, **R4** and **R5**, Ti is oxidized and Nb is reduced simultaneously. At 0 K, all reactions except **R5** in Table 4.2 are favourable. In other words, only **R5** is spontaneous at all temperatures. An increase in the entropy is usually what drives the etching reactions, hence the free energy decreases at higher temperatures and even R3 and **R4** become spontaneous at temperatures above 500 K. According to the reaction **R5**, the predicted by-products are  $\text{TiF}_4$ ,  $\text{NbFCl}_3$  and  $\text{ClCN}$ . At 640 K (370 °C), R1 and **R2** are more unlikely when compared to R3, **R4**, and **R5** - not because of the titanium containing gaseous species but because of less favourable gaseous species containing niobium and nitrogen.

The evaluated product pressures ( $P_p$ ) indicate the likelihood of the formation of the etch products in the reaction. Small  $P_p$  values as in R1 and **R2** suggest that  $\text{NbNF}$ ,  $\text{NbNFCl}$ , and  $\text{CF}_4$  are not likely to be formed. On the other hand, a high  $P_p$  (at  $\Delta G = 0$  and 740 K) for **R5** indicates a high probability of forming volatile  $\text{TiF}_4$ ,  $\text{NbFCl}_3$  and  $\text{ClCN}$  species,<sup>89,150-153</sup> hence the etching.  $\text{TiF}_4$  is volatile and sublimates at 284 °C.<sup>89,92</sup> On the contrary,  $\text{TiF}_3$  is not volatile, especially within 370-460 °C,<sup>89,154</sup> and therefore was not considered.

Table 4.3: Potential reactions of individual reagent pulses with bulk TiN in the etch process, assessed via thermochemistry computed with DFT. **R6** - **R8** represent the fluorination pulse and R9 represents the chlorination pulse.  $P_p$  at  $\Delta G=0$  is the product pressure at 740 K that will bring the reaction to equilibrium at a constant reactant pressure of 2.5 Torr. Reproduced with permission from Paper [IV], Copyright ©2021 John Wiley and Sons.

Reactions	$\Delta G$ [eV]		$P_p$ [Torr] at $\Delta G=0$ ; T=740 K
	640 K	740 K	
<b>R6:</b> $\text{TiN} + \text{NbF}_5 \rightarrow \text{TiNF} + \text{NbF}_4$	6.1	5.7	7.3E-24
R7: $\text{TiN} + \text{NbF}_5 \rightarrow \text{TiF}_3 + \text{NbNF}_2$	3.5	3.1	4.2E-15
<b>R8:</b> $\text{TiN} + \text{NbF}_5 \rightarrow \text{TiF}_4 + \text{NbNF}$	3.9	3.5	2.5E-16
R9: $\text{TiN} + \text{CCl}_4 \rightarrow \text{TiCl}_3 + \text{ClCN}$	-2.0	-2.4	1.8E+04

Table 4.3 shows reactions (**R6** - R9) between TiN and either  $\text{NbF}_5$  or  $\text{CCl}_4$  alone. **R6**, R7, and **R8** describe the fluorination step in which  $\text{NbF}_5$  reacts with solid TiN to form gaseous  $\text{TiF}_x$  and  $\text{NbNF}_y$  species. For fluorination reactions, highly positive  $\Delta G$  (+3.1 to +5.7 eV at 740 K) and extremely low  $P_p$  values are computed. This indicates that none of the fluorination reactions is able to etch TiN, mainly due to the unfavourable Nb-N compounds. Similarly, the previously discussed adsorption of  $\text{NbF}_5$  on the TiN surface via the dissociation path at 400 K resulted in strong surface Ti-F and Nb-N bonds but no gas phase products were formed in the DFT adsorption studies (more details are in the SI of [IV]). Moreover, the DFT investigations revealed that the Ti-F bonds on the TiN surface are more stable and favourable than the Ti-Cl bonds (see section S3 of [IV]).

The etching of TiN by CCl<sub>4</sub> as described by R9 is spontaneous at 640 and 740 K ( $\Delta G < 0$ ) and the predicted volatile etch products are TiCl<sub>3</sub> and ClCN. Moreover, a very large  $P_p$  value at  $\Delta G=0$  and 740 K also shows the likelihood of the formation of the products. In support, the DFT adsorption studies also predicted the spontaneous dissociation of CCl<sub>4</sub> on TiN(211) surface (more information in the section S2 of [IV]).

In conclusion, subjected to kinetic barriers, the first principles thermochemistry investigations suggest that TiN is not etched by NbF<sub>5</sub> but is etched spontaneously by CCl<sub>4</sub> alone. The DFT studies also predict that NbF<sub>5</sub> - CCl<sub>4</sub> binary process (as per **R5**) provides more effective etching than CCl<sub>4</sub> alone (as per R9). Later, in section 4.2.2, the etch per cycle for the binary process is observed to be higher than for the CCl<sub>4</sub> alone etch process. ClCN is common in both **R5** and R9, while the products TiCl<sub>3</sub> and TiF<sub>4</sub> have very similar zero point energy and entropy.<sup>155,156</sup> However, it is the NbFCl<sub>3</sub> that offers a lower zero point energy and higher entropy than NbF<sub>5</sub> and therefore **R5** attains a lower reaction free energy than R9. Last but not least, the simulations also show that the presence of Nb atoms on the surface allows CCl<sub>4</sub> to spontaneously dissociate which further allows the formation of NbF<sub>x</sub>Cl<sub>y</sub> species as in **R5**. In this way, NbF<sub>5</sub> is predicted to enhance the etching of TiN by CCl<sub>4</sub> as experimentally verified (see Figures 4.12 b) and 4.13 a)).

#### 4.2.2 Effect of etchant pulse times

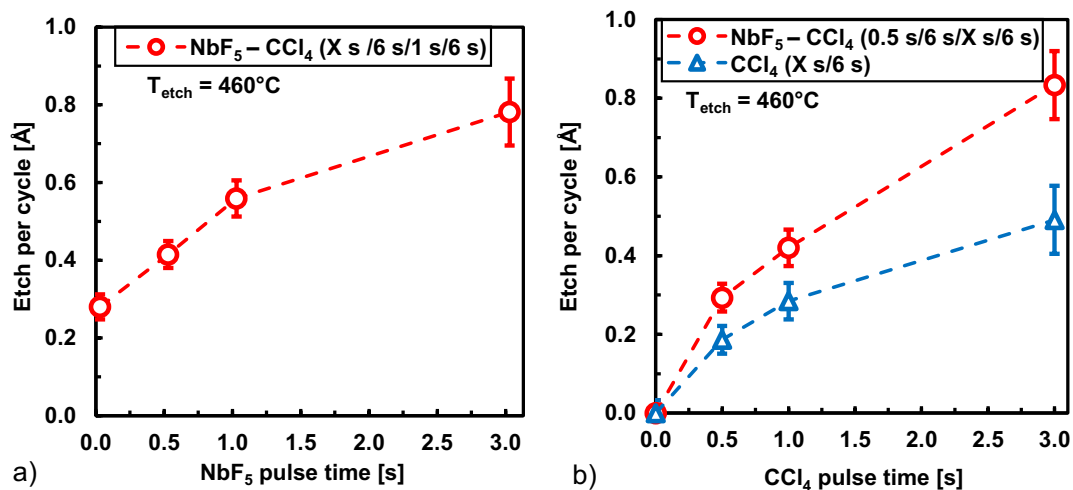


Figure 4.12: Etch per cycle for TiN films with varying: a) NbF<sub>5</sub>, and b) CCl<sub>4</sub> pulse times, at 460 °C. The N<sub>2</sub> purges were fixed at 6 s. Reproduced with permission from Paper [IV], Copyright ©2021 John Wiley and Sons.

Figure 4.12 plots the variation in the EPC with respect to the NbF<sub>5</sub> and CCl<sub>4</sub> pulse times for both the NbF<sub>5</sub> - CCl<sub>4</sub> as well as CCl<sub>4</sub> only etching processes. In both cases, the N<sub>2</sub> purges were kept constant at 6 s, each. In Figure 4.12 a) an EPC value of about 0.3 Å is noted when no NbF<sub>5</sub> is used. This reveals that TiN is etched by CCl<sub>4</sub> alone. Here the CCl<sub>4</sub> pulse time was fixed to 1 s and in total 200 cycles were performed. The capability of TiN being etched by CCl<sub>4</sub> alone



has been already predicted by DFT (section 4.2.1). When the  $\text{NbF}_5$  pulse time is increased from 0 to 3 s, a non-saturating increase in the EPC from 0.3 Å to about 0.8 Å is observed. It was speculated that this increase in the EPC with the  $\text{NbF}_5$  pulse time can be attributed to a slow diffusion of fluoride along TiN grain boundaries leading to a fluorinated TiN layer, more Nb sites for  $\text{CCl}_4$  to react with, inadequate purge time, low volatility or otherwise slow removal of the products from the TiN surface, and the presence of finite vapors of  $\text{CCl}_4$  in the etch system.

Figure 4.12 b) compares the EPCs of the two etch processes with fixed  $\text{NbF}_5$  and varying  $\text{CCl}_4$  pulse times at 460 °C. It is noted that the EPC for the  $\text{NbF}_5$  -  $\text{CCl}_4$  etch process is higher than for the  $\text{CCl}_4$  only etching process. This is consistent with the DFT results in 4.2.1 where an enhanced etch rate is predicted when  $\text{NbF}_5$  is added to the  $\text{CCl}_4$  etch process.

### 4.2.3 Effect of etching temperature

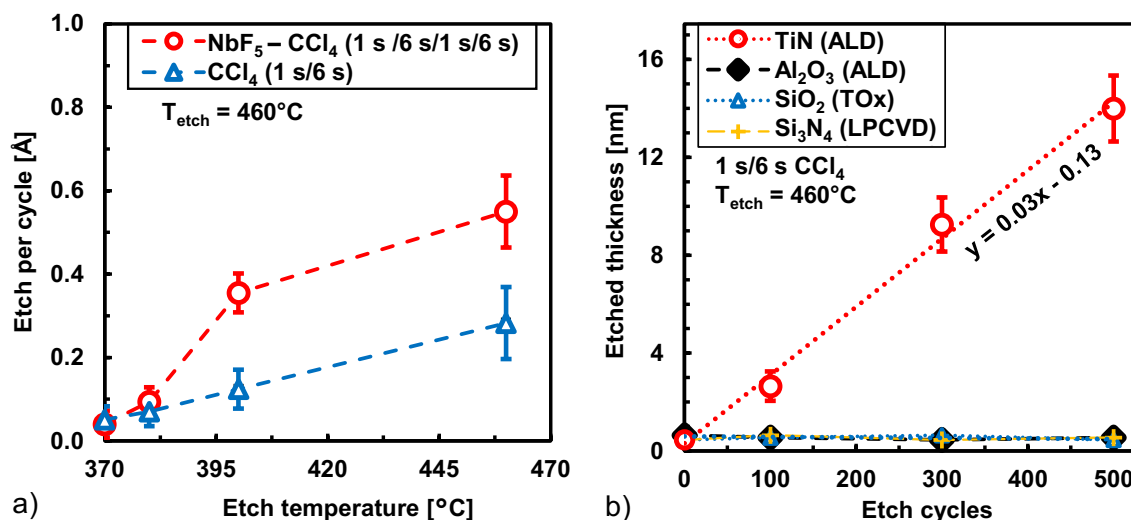


Figure 4.13: a) Etch per cycle of TiN films at different etch temperatures for both  $\text{NbF}_5$  -  $\text{CCl}_4$  and  $\text{CCl}_4$  only etch processes, b) etched thickness of various materials vs. etch cycles for  $\text{CCl}_4$  only etch process. Reproduced with permission from Paper [IV], Copyright ©2021 John Wiley and Sons.

Figure 4.13 summarizes the effect of the etch temperature on the EPC for the both etching processes. Again, consistent with the DFT results, the TiN EPC for  $\text{NbF}_5$  -  $\text{CCl}_4$  is significantly higher at 400 and 470 °C than for the  $\text{CCl}_4$  only process. Albeit, below 400 °C, the small values of EPC obscure this enhancement effect and the EPC values are the same for the both processes. In the case of the  $\text{NbF}_5$  -  $\text{CCl}_4$  process, the EPC values are about 0.4 and 0.5 Å, at 400 and 460 °C, respectively. On the other hand, for the  $\text{CCl}_4$  only process, an EPC of 0.1 Å at 400 °C is measured and it increases to about 0.3 Å at 460 °C. No significant etching was observed at temperatures below 370 °C, even after 1000 etch cycles of both processes.

**Selectivity:** As concluded from Figure 4.13 b), the  $\text{CCl}_4$  alone etching process allows the removal of TiN selectively over  $\text{Al}_2\text{O}_3$ ,  $\text{SiO}_2$ , and  $\text{Si}_3\text{N}_4$ , at 460 °C [IV].



The figure shows the etched thickness of TiN with increasing number of cycles and an EPC of about  $0.3 \text{ \AA}$  with 1 s  $\text{CCl}_4$  pulse time. After 500 etch cycles, about 13 nm TiN is etched and no change in the thickness is observed for  $\text{Al}_2\text{O}_3$ ,  $\text{SiO}_2$  and  $\text{Si}_3\text{N}_4$ . Hence, selective removal of TiN is possible within an etch window of  $370\text{-}460 \text{ }^\circ\text{C}$ . On the contrary, the  $\text{NbF}_5\text{-CCl}_4$  etch process removes  $\text{Al}_2\text{O}_3$  and thus provides selectivity over  $\text{SiO}_2$  and  $\text{Si}_3\text{N}_4$  only.

#### 4.2.4 Post-etch film characterization

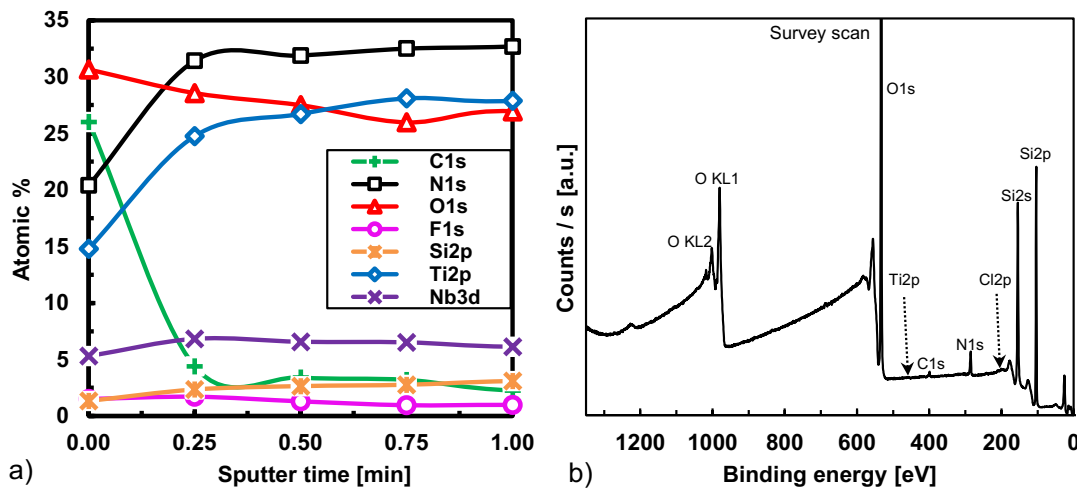


Figure 4.14: X-ray photoelectron spectroscopy, a) depth profile of remaining 9 nm TiN film after being partially etched by  $\text{NbF}_5\text{-CCl}_4$ , b) survey scan of  $\text{SiO}_2$  surface left after complete removal of TiN film by the  $\text{CCl}_4$  etch process at  $460 \text{ }^\circ\text{C}$ . Reproduced with permission from Paper [IV], Copyright ©2021 John Wiley and Sons.

In Figure 4.14 a), an ex-situ XPS depth profile analysis shows the elemental composition of 9 nm TiN film which was left after incomplete etching. The initial film was exposed to 300 cycles of the  $\text{NbF}_5\text{-CCl}_4$  process at  $460 \text{ }^\circ\text{C}$ . The surface is composed of about 31 atomic % O, 26 atomic % C, 20 atomic % N, 15 atomic % Ti and about 5 atomic % Nb. Small amounts of Si and F ( $< 2$  atomic %, each) are associated with the  $\text{SiO}_2$  substrate and F penetration along the grain boundaries. To emphasize and study the elements on the TiN surface, a low Ar ion energy of 1 keV was used for depth profiling. This Ar ion energy was chosen to ensure very low TiN etch rates ( $\leq 0.2 \text{ \AA/s}$ , removal of 1.2 nm/min) and minimize any induced chemical shifts. The high amount of O1s signal detected after 0.25 min of sputtering can be associated with surface oxidation or the implantation of O ions into the TiN film by impinging Ar ions. Moreover, the high affinity of titanium towards oxygen is well known and exploited in sublimation and ion pumps in capturing oxygen residuals from a vacuum chamber.<sup>157</sup> The F in the film can be the result of Ar ion sputtering and drops below 1 atomic % after 60 s of sputtering. The carbon content decreases to about 4 and 3 atomic % after 15 s and 60 s sputter times, respectively. On the other hand, after 15 s of sputtering the Ti and N contents stayed around 25 and 32 atomic %,

respectively. The presence of significant amounts of Nb (about 6 atomic %) and F (0.9-1.7 atomic %) indicates that  $\text{NbF}_5$  is capable of either reacting or dissociating on TiN. This is consistent with the DFT adsorption studies discussed earlier. Lastly, no chlorine was detected by XPS which suggests the full formation and removal of volatile products containing chlorine such as  $\text{TiCl}_3$ ,  $\text{TiCl}_4$ ,  $\text{NbFCl}_3$ ,  $\text{NbClF}_4$ , and  $\text{ClCN}$ . These products were already predicted by the DFT computations.

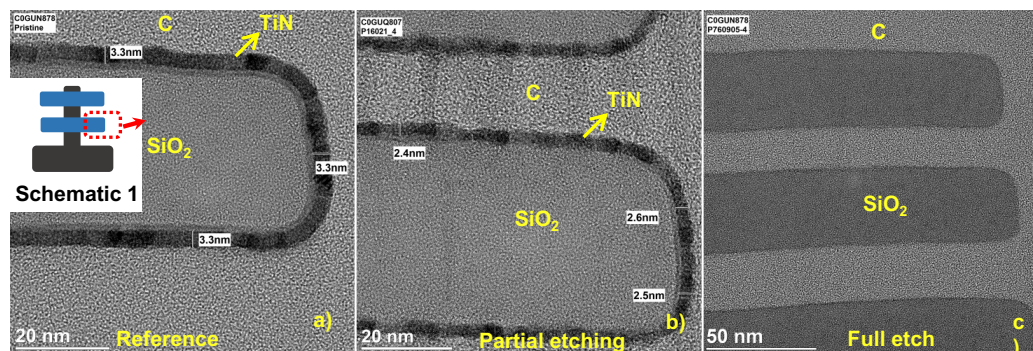


Figure 4.15: Cross-sectional bright-field transmission electron micrograph (BF-TEM) of 3D structures: a) about 3.3 nm TiN film deposited on  $\text{SiO}_2$  fins with lateral cavities, b) the same after etching about 0.8 nm TiN is etched by the  $\text{NbF}_5$  -  $\text{CCl}_4$  process, and c) after removing the TiN film completely. The etching was performed at 460 °C. Schematic 1 in the inset roughly represents the 3D structures on the surface where the horizontal fins ( $\text{SiO}_2$ ) are blue and the back-bone (Si) is black. Reproduced with permission from Paper [IV], Copyright ©2021 John Wiley and Sons.

The TEM images displayed in Figure 4.15 focus on horizontal fins, instead of the whole 3-D structures that were patterned on the silicon substrate. The main purpose of these structures was to verify the isotropic etching, despite the non self-limiting etch reactions. The etch conformality studies in the horizontal cavities emphasize the non-directionality of ALEt. A thin and extremely conformal TiN film was grown by thermal ALD<sup>119</sup> for the etching experiments. Due to the gradient in the partial pressure of the reactant in the 3D structures, CVE by single etchant may result in non-conformal etching, especially when the reaction kinetics are much faster than the diffusion kinetics of the reactant molecules. While, the CVE may result in non-conformal etching especially from the non-line-of-sight features similar to that in schematic 1, another reagent such as  $\text{NbF}_5$  in this case can be introduced to improve the etch conformality or modify the EPC. Figure 4.15 a) shows the reference  $\text{SiO}_2$  fins with the conformally deposited 3.3 nm thick TiN film. The conformal and isotropic etching of TiN by the  $\text{NbF}_5$  -  $\text{CCl}_4$  process is shown in Figure 4.15 b) where about 0.8 nm TiN has been etched without any significant increase in the surface roughness. After over-etching the TiN completely from the structure, as seen in Figure 4.15 c), no surface contaminants or particles are observed. Also the thickness of the  $\text{SiO}_2$  fins is unchanged, hence confirming the etch selectivity.

## 4.3 TiN etching by SOCl<sub>2</sub>

Spontaneous etching of TiN by SOCl<sub>2</sub> is explored in this section, and the details are published in [1]. A single etchant can remove material either in a continuous or a pulsed fashion, and the latter is defined as gas-phase pulsed etching (GPPE). The GPPE offers an additional parameter, i.e. the number of etch cycles which allows an ångström-level control of the etched thickness. Section 4.3.1 covers the thermodynamics of the etch reactions, 4.3.2 discusses the effect of an etchant pulse time on the EPC, and 4.3.3 addresses an effect of the etch temperature on the EPC. Lastly, the post-etch surfaces are characterized using XPS and TEM in 4.3.4.

### 4.3.1 Thermodynamic calculations

Before going to the experimental results, thermodynamic calculations are first discussed to assess the feasibility of SOCl<sub>2</sub> as an etchant for TiN and also for Al<sub>2</sub>O<sub>3</sub>, Si<sub>3</sub>N<sub>4</sub>, and SiO<sub>2</sub> from the perspective of selective etching. The bulk thermodynamic calculations provide changes in the Gibbs free energy ( $\Delta G$ ), entropy ( $\Delta S$ ) and enthalpy ( $\Delta H$ ) for possible reactions between SOCl<sub>2</sub> vapors and solid etch targets. A positive change in the entropy was observed within a wide temperature range (0 - 1000 °C) for all the reactions considered here.

From the HSC database, the etch targets TiN, Al<sub>2</sub>O<sub>3</sub>, SiO<sub>2</sub>, and Si<sub>3</sub>N<sub>4</sub> were chosen in solid form, which closely represents the thin films. The SOCl<sub>2</sub> etchant was in gaseous form. Depending upon the choice of byproducts, many reactions are possible. However, in order for the etching to take place, only those by-products that are either volatile or available in the gaseous form were selected. These are AlCl<sub>3</sub>, AlOCl, <sup>158</sup> SiCl<sub>4</sub>, TiOCl<sub>2</sub>, TiOCl, TiCl<sub>3</sub>, TiCl<sub>4</sub>, O<sub>2</sub>, N<sub>2</sub>, N<sub>2</sub>O, NO<sub>2</sub>, SO<sub>2</sub>, SO and S<sub>2</sub>Cl<sub>2</sub>. With the above reactants and by-products, various potential overall reactions with their  $\Delta G$  values with respect to temperature are plotted in Figure 4.16. A few reactions were ignored and are not discussed here due to very high positive  $\Delta G$  throughout the temperature range. In addition, the reactions that had TiOCl as a by-product were excluded due to its low volatility at 270-370 °C. <sup>159,160</sup>

In Figure 4.16 a), all the reactions show a negative change in Gibbs free energy, especially at temperatures above 300 °C, and are therefore favourable. However, which particular reaction actually takes place is subjected to the kinetic barriers. From the reactions described in Figure 4.16, titanium is predicted to form volatile products such as TiCl<sub>4</sub>(g), TiCl<sub>3</sub>(g) and TiOCl<sub>2</sub>(g). In the reactions **R1-R6**, nitrogen from the TiN film is proposed to form volatile N<sub>2</sub> or NO<sub>2</sub> species. On the contrary, for sulfur SO<sub>2</sub>(g), SO(g) and S<sub>2</sub>Cl<sub>2</sub>(g) are evidently plausible etch by-products.

Figure 4.16 b) plots  $\Delta G$  as a function of temperature for several possible reactions between bulk Al<sub>2</sub>O<sub>3</sub>, SiO<sub>2</sub>, and Si<sub>3</sub>N<sub>4</sub> and SOCl<sub>2</sub>(g). All reactions except **R8** in the figure are endothermic ( $\Delta H > 0$  at all temperatures), that is they require external energy to undergo completion. For an etching to take place, Al must form volatile compounds with chlorine. The volatile compounds containing Al and Cl are AlCl<sub>3</sub> and its dimer form Al<sub>2</sub>Cl<sub>6</sub>. <sup>161</sup> Gaseous AlOCl can be excluded due to a positive  $\Delta G$  for **R9** in Figure 4.16 b)

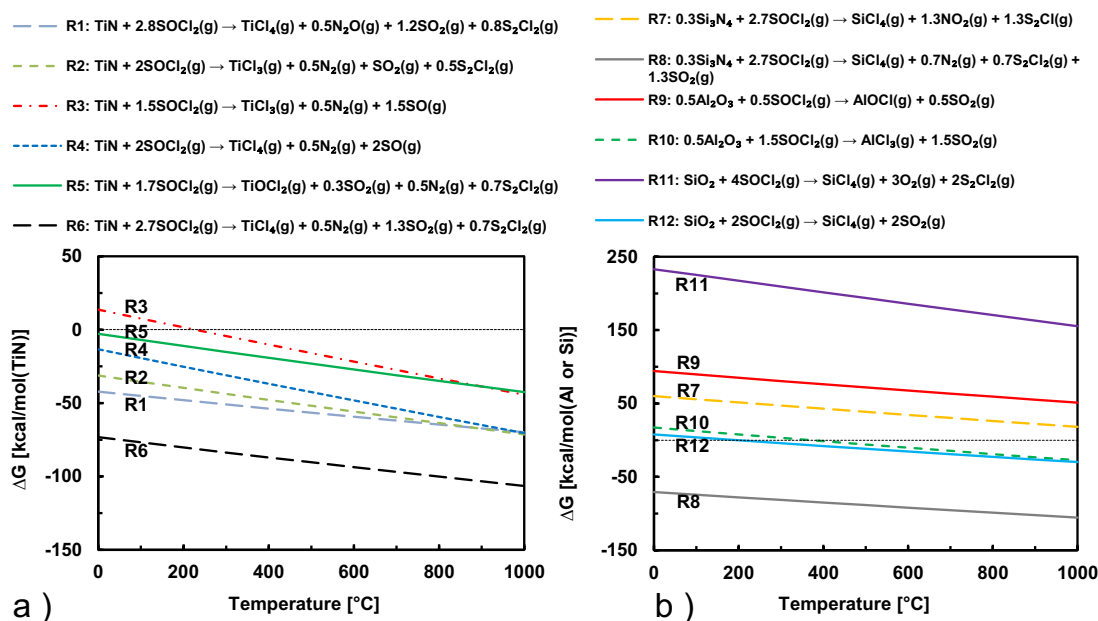


Figure 4.16: Change in Gibbs free energy at different temperatures for several possible reactions between gaseous  $\text{SOCl}_2$  and solids a) TiN, b)  $\text{Al}_2\text{O}_3$ ,  $\text{SiO}_2$  and  $\text{Si}_3\text{N}_4$ . Adapted from [1], Copyright © 2021 Authors, Published by Elsevier, distributed under a Creative Commons (CC BY-NC-ND) License.

and its non-volatility (at least within the temperature range used for the etching experiments) was experimentally found by Greenbaum<sup>158</sup> and Harald.<sup>162</sup> On the other hand, **R10** with  $\text{AlCl}_3$  as a by-product has  $\Delta G < 0$  above 380 °C. Our experiments showed that  $\text{SOCl}_2$  cannot etch  $\text{Al}_2\text{O}_3$  at 370 °C (see 4.18). **R12** in Figure 4.16 b) shows a slightly negative  $\Delta G$  above 200 °C, but the  $\Delta H$  is positive ( $\geq 15$  Kcal/mol(Si), at 0 - 1000 °C) and indicates an entropy driven spontaneous reaction. For  $\text{Si}_3\text{N}_4$ , only **R8** is favourable and spontaneous at all temperatures. However, from our experiments it is concluded that  $\text{SOCl}_2$  does not etch  $\text{Si}_3\text{N}_4$  or  $\text{SiO}_2$  within 270 - 370 °C. This can be explained by either large kinetic barriers or non-favourable surface-gas reactions.

### 4.3.2 Effect of etchant pulse and purge times

Cyclic exposures to  $\text{SOCl}_2$  vapors, separated by inert gas purges, were used for the controlled etching of TiN films at 320 °C. The  $\text{N}_2$  gas purge steps were performed to remove excess reactant, as well as the etch product molecules from the etch system.

In Figure 4.17 a) the EPC at various  $\text{SOCl}_2$  pulse times is plotted. A non self-limiting EPC is observed when the  $\text{SOCl}_2$  pulse time is varied from 0 to 3 s. An almost linear increase in the EPC is observed from 0.02 Å at 0.5 s to about 0.36 Å at 3 s  $\text{SOCl}_2$  pulse time. After 1000  $\text{SOCl}_2$  pulses of 3 s length, about 35 nm TiN film was etched, which was confirmed by SE, weight measurements, XPS and XRR. Further increase in EPC is expected with longer  $\text{SOCl}_2$  pulse times.

Figure 4.17 b) summarizes the effect of the purge time on the EPC, at a fixed 2 s  $\text{SOCl}_2$  pulse time. With increasing purge times, an increase in the EPC is

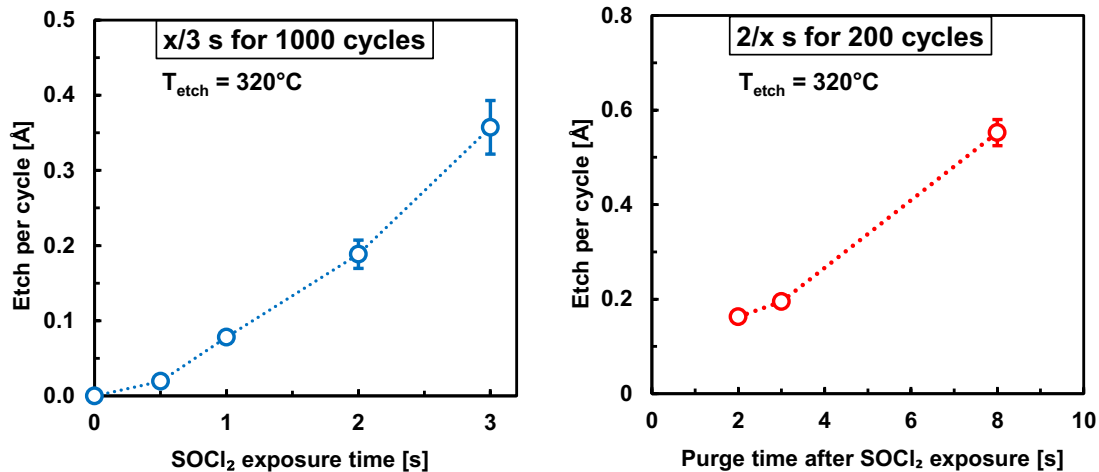


Figure 4.17: Etch per cycle of TiN films vs. a) SOCl<sub>2</sub> pulse time at 320 °C with 3 s of N<sub>2</sub> purges in-between, b) etch per cycle with varying purge times. Adapted from [1], Copyright © 2021 Authors, Published by Elsevier, distributed under a Creative Commons (CC BY-NC-ND) License.

observed, and EPC follows an almost linear trend up to 8 s. EPCs of 0.16 and 0.19 Å is noted for 2 s and 3 s purge times, respectively. At 8 s purge time, the EPC reaches 0.55 Å. The strong dependence of the EPC on the purge time can be due to several reasons such as long time needed for the SOCl<sub>2</sub> vapors to reach its saturated vapor pressure in the source vessel, inefficient purging of SOCl<sub>2</sub>, or a slow removal of less volatile species from the TiN surface. Less volatile species (compared to TiCl<sub>4</sub>) are TiCl<sub>3</sub><sup>163</sup> and TiOCl<sub>2</sub>.

Furthermore, a slow disproportionation reaction, **R13:**  $2 \text{TiCl}_3 \longrightarrow \text{TiCl}_{2(s)} + \text{TiCl}_{4(g)}$ ,<sup>163–165</sup> may generate more TiCl<sub>4</sub> species for the etching to continue even during the purge step. Another possibility could be a presence of residual SOCl<sub>2</sub> molecules in the chamber and thus prolonged etching during purge steps. Albeit the Ångström-level etch control, the non self-limiting etching can produce higher etch non-uniformity.

### 4.3.3 Selectivity and effect of etching temperature

One of the key features of GPPE is its ability to selectively etch one material over the other. Several applications in the semiconductor industry require selective etching. Therefore, the ability of SOCl<sub>2</sub> to etch other materials such as Al<sub>2</sub>O<sub>3</sub>, SiO<sub>2</sub> and Si<sub>3</sub>N<sub>4</sub> was also assessed. Figure 4.18 clearly shows that only TiN is etched within 270-370 °C. At higher temperatures, the EPC of TiN increases exponentially. However, even after 1000 cycles of 2 s SOCl<sub>2</sub> pulses, no change in thickness was observed for Al<sub>2</sub>O<sub>3</sub>, SiO<sub>2</sub> and Si<sub>3</sub>N<sub>4</sub>. This confirms that TiN is etched selectively over Al<sub>2</sub>O<sub>3</sub>, SiO<sub>2</sub> and Si<sub>3</sub>N<sub>4</sub>.

### 4.3.4 Post-etch film characterization

After exposing the TiN films to SOCl<sub>2</sub> pulses, the remaining surfaces were analysed using XPS, TEM and AFM. Figure 4.19 shows the elemental composition of the surface after complete etching of TiN. The surface

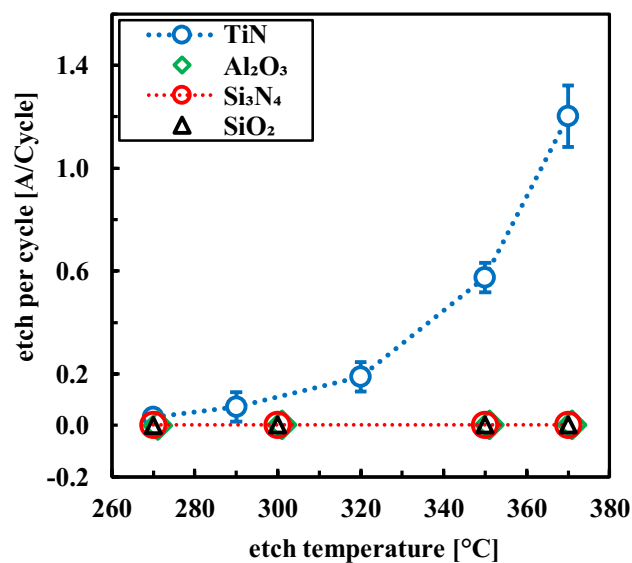


Figure 4.18: Etch per cycle for TiN, SiO<sub>2</sub>, Al<sub>2</sub>O<sub>3</sub> and Si<sub>3</sub>N<sub>4</sub> as a function of etch temperature. The SOCl<sub>2</sub> pulse and N<sub>2</sub> purge times were 2 and 3 s, respectively. Reproduced from [1], Copyright © 2021 Authors, Published by Elsevier, distributed under a Creative Commons (CC BY-NC-ND) License.

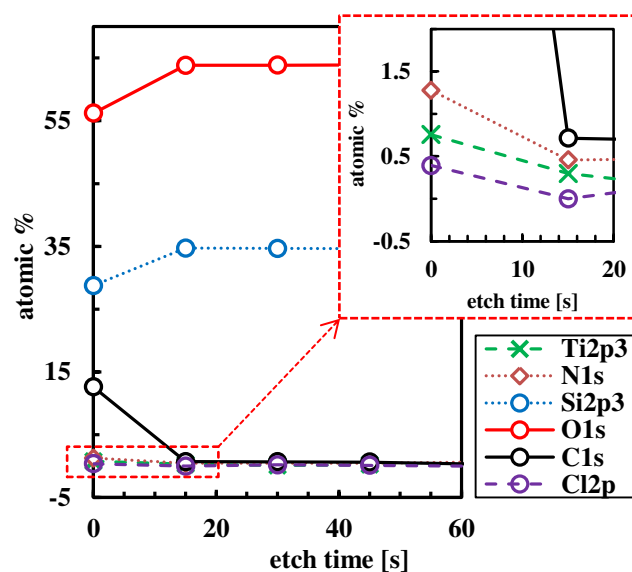


Figure 4.19: XPS depth profiles of a SiO<sub>2</sub> surface after complete removal of TiN film. The surface contaminants are shown in the zoomed-in inset at the top right corner. Reproduced from [1], Copyright © 2021 Authors, Published by Elsevier, distributed under a Creative Commons (CC BY-NC-ND) License.

comprises of silicon, oxygen, and some surface carbon, with very low amounts of titanium and nitrogen. The zoomed-in figure displays about 1.3 and 0.7 atomic % of nitrogen and titanium, respectively. The chlorine content is less than 0.5 atomic % (the detection limit of the XPS). Sulfur from the etchant is not seen. The low amounts of N and Ti can be due to incomplete etching. Maybe a few additional etch cycles would have removed them. No chlorine penetration is detected in the SiO<sub>2</sub> film. However, SOCl<sub>2</sub>



may be able to chlorinate the  $\text{SiO}_2$  surface by forming Si–Cl bonds. For every depth measured (i.e. at every 15 s sputtering interval) the total number of elements fitted was the same and their contents were normalized to 100 atomic %, and the magnitude of the error introduced was estimated about 4 atomic %. The error is due to low signal to noise ratios associated with the measurement and analysis, and fit and measurement error of about 1 atomic % per element. This fitting error explains the incorrect Si to O ratio for the thermal oxide substrate.

Figure 4.20 a) shows a reference structure where a 22 nm TiN film is present on a 20 nm  $\text{SiO}_2$  film.  $\text{SiO}_2$  lines running perpendicular to the image plane were patterned on the TiN layer. The purpose of these test structures was to study the isotropic etching and etch-selectivity towards  $\text{SiO}_2$ . In Figure 4.20 b) 2-3 nm of TiN has been selectively removed over  $\text{SiO}_2$ , without much affecting the TiN roughness, but some under-cut etch can be observed. In Figure 4.20 c) all TiN have been etched from the openings and under the  $\text{SiO}_2$  lines and the lateral etching has resulted in the pattern collapse. No  $\text{SiO}_2$  etching is observed which confirms the selectivity.

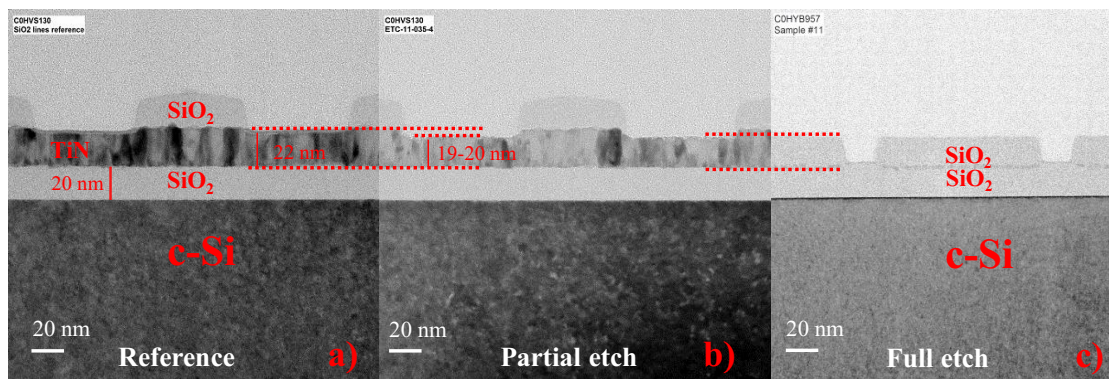


Figure 4.20: Cross-sectional bright-field transmission electron microscope (BF-TEM) images of a) patterned  $\text{SiO}_2$  lines on  $\approx 22$  nm TiN film, where a strong diffraction contrast is seen for the poly-crystalline TiN film, b) the same after etching 2-3 nm of TiN, and c) after complete isotropic removal of TiN underneath  $\text{SiO}_2$  and consequent collapse of  $\text{SiO}_2$  lines. Reproduced from [1], Copyright © 2021 Authors, Published by Elsevier, distributed under a Creative Commons (CC BY-NC-ND) License.

Figure 4.21 a) shows the surface morphology of the unetched TiN film with a roughness of 0.54 nm ( $R_a$ ). A small increase in the roughness to 0.81 nm is observed after removing about 7 nm TiN. As a reference, Figure 4.21 c) shows a smoother 20 nm  $\text{SiO}_2$  film with  $R_a$  of 0.16 nm.

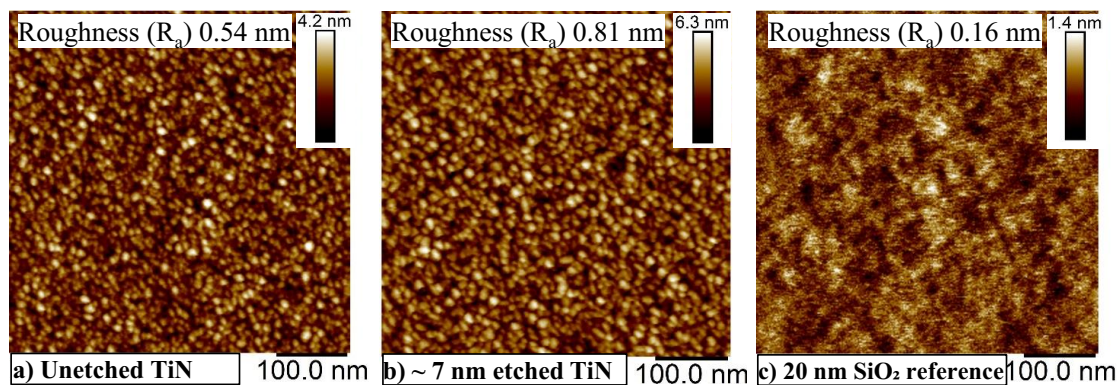


Figure 4.21: AFM images and surface roughnesses of a) about 25 nm unetched TiN film on 20 nm SiO<sub>2</sub>, b) after etching about 7 nm of TiN, and c) reference 20 nm SiO<sub>2</sub> film. The etch temperature was 320 °C. Reproduced from [I], Copyright © 2021 Authors, Published by Elsevier, distributed under a Creative Commons (CC BY-NC-ND) License.

## 4.4 SiGe etching by (O<sub>2</sub> or O<sub>3</sub>/O<sub>2</sub>)-HF-TMA

SiGe (Si<sub>0.15</sub>Ge<sub>0.85</sub>) was etched by first oxidizing the film to SiGeO<sub>x</sub> and then exposing it to the HF-TMA etch chemistry. This type of etching process is an example of oxidation and "conversion-etch" mechanism. In the literature, the same etch mechanism is shown to etch elemental silicon<sup>87</sup> and silicon nitride<sup>88</sup> films. Oxidation was performed by either O<sub>2</sub> or O<sub>3</sub>. The important etching results, possible etch-mechanism and XPS analysis of the post-etched films discussed in this section are from the article [IV].

### 4.4.1 Etching experiments

Figure 4.22 b) plots the EPC with respect to the O<sub>2</sub>, HF and TMA pulse times. EPC does not fully saturate with increasing O<sub>2</sub> pulse time. EPC increases linearly from 0.4 Å to about 0.7 Å, when the O<sub>2</sub> pulse time is varied from 0.4 s to 2.5 s. While varying the O<sub>2</sub> pulse time, the TMA and HF pulse times were fixed to 1.0 s each. EPC saturates to about 0.5 Å for both the TMA and the HF pulse times. The TMA pulse time was varied from 0.4 s to 1.7 s, and the HF pulse time was varied from 0.5 s to 1.7 s, while the O<sub>2</sub> pulse time was fixed to 1.5 s.

Figure 4.22 a) shows the EPC with varying O<sub>3</sub>, HF and TMA pulse times. It is clear that the EPC saturates to approximately 0.4 Å with respect to the pulse times of all reactants. The EPC levels out starting at 0.5 s of each reactant pulse. Ozone is a stronger oxidizing agent than oxygen and therefore the saturated and lower EPC obtained with O<sub>3</sub> is counter-intuitive. However, O<sub>3</sub> may form a dense SiGeO<sub>x</sub> oxide layer which acts as a better diffusion barrier layer and thus stops further oxidation of the underlying SiGe film.



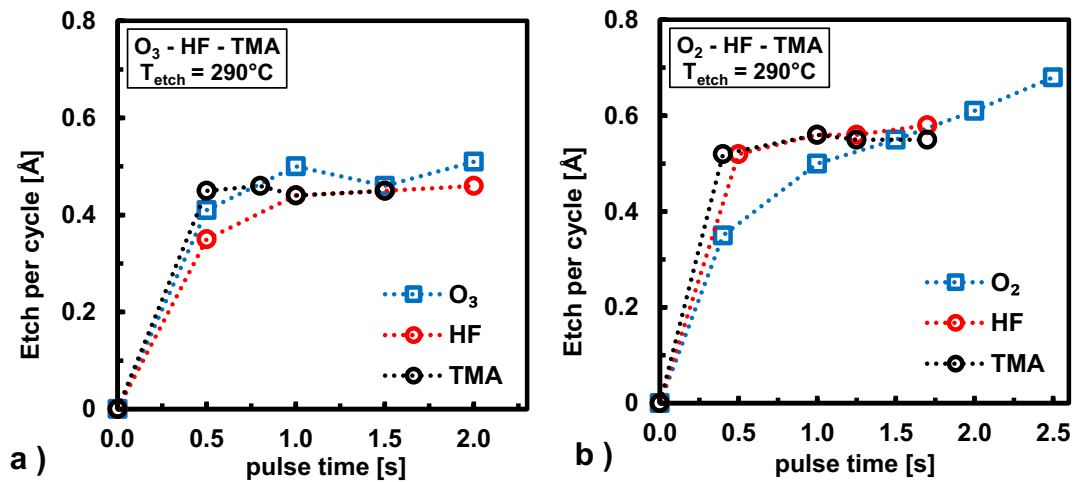
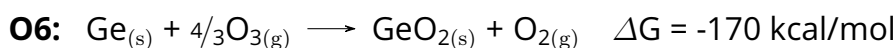
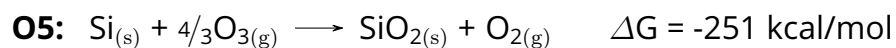
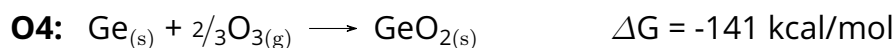
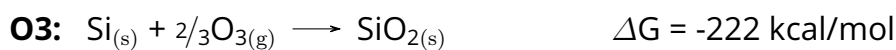
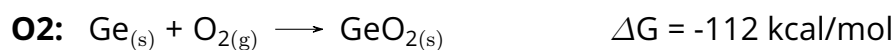


Figure 4.22: The etch per cycle vs. reactant pulse times for a) O<sub>3</sub> - HF - TMA, and b) O<sub>2</sub> - HF - TMA SiGe ALEt. The purge times were kept constant at 30 s each. Adapted with permission from [II], Copyright © 2021 American Vacuum Society.

#### 4.4.2 Thermodynamic calculations

A change in the Gibbs free energy at 300 °C is calculated from the bulk thermodynamics for the oxidation of Si and Ge elements as per the reactions **O1-O6**:



The oxidation of individual elements was considered because SiGe alloys are not listed in the HSC Chemistry (ver. 10) software database. For the corresponding oxidation reactions, the larger negative  $\Delta G$  values when O<sub>3</sub> is used indicate more favourable reactions than when O<sub>2</sub> is used and may predict thicker, denser and higher quality surface oxide. From the above reactions, it can also be concluded that the oxidation of Si is more favourable than that of Ge.

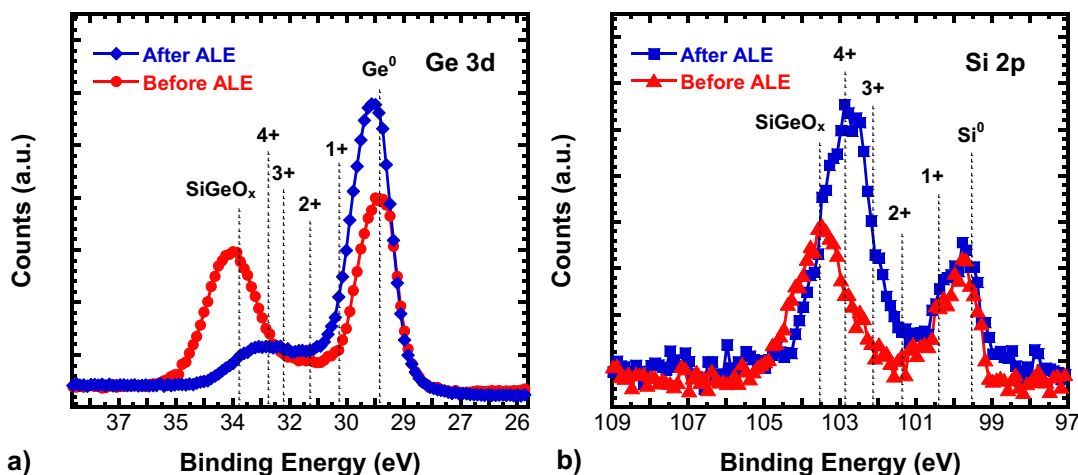


Figure 4.23: XPS spectra of a) Ge 3d , and b) Si 2p signals for SiGe films before and after 100 cycles of  $O_2$  - HF - TMA ALE process at 290 °C. Reproduced with permission from [11], Copyright © 2021 American Vacuum Society.

#### 4.4.3 XPS analysis of the post-etched film

SiGe films were subjected to the surface composition analysis with the ex-situ XPS measurements. The surface of the pristine SiGe ( $Si_{0.15}Ge_{0.85}$  and the Ge to Si ratio of 5) film was comprised of 38.8 atomic % germanium, 50.9 atomic % oxygen, 5.2 atomic % silicon and 5.1 atomic % carbon. After performing 100 ALE cycles of  $O_2$  - HF - TMA (the last pulse), the composition was 39.1 atomic % germanium, 29.4 atomic % oxygen, 8.8 atomic % silicon, 20.9 atomic % carbon, 0.8 atomic % fluorine and 1 atomic % aluminum. The high amount of surface carbon is associated with the handling of the sample in a non-clean room environment and partly to surface methyl groups, likely in the form of  $Si-CH_3$ .

Figure 4.23 compares the XPS spectra of Ge 3d and Si 2p before and after 100 cycles of the  $O_2$  - HF - TMA ALE process. Figure 4.23 a) reveals several germanium oxidation states (denoted by the vertical dotted lines) with a reference binding energy (BE) for  $3d^{5/2}$  XPS peak of  $Ge^0$  at 29.4 eV.<sup>166</sup> For the unetched film, a strong peak is centered at  $33.5 \pm 0.1$  eV and is ascribed to  $SiGeO_x$  oxide.<sup>167</sup> This peak is of much lower intensity after 100 ALE cycles, indicating that the surface oxide is etched away. For the unetched SiGe films, a thick native oxide of about 31 Å was measured by an ellipsometer. The low intensity shoulder peaks as shown by dashed lines in Figure 4.23 a) are assigned to  $Ge^{1+}$ ,  $Ge^{2+}$ ,  $Ge^{3+}$ , and  $Ge^{4+}$  oxidation states. The chemical shifts of  $Ge^{1+}$ ,  $Ge^{2+}$ ,  $Ge^{3+}$ , and  $Ge^{4+}$  with reference to the  $Ge^0$  have been experimentally measured as 0.8, 1.8, 2.75, and 3.3 eV ( $\pm 0.5$  eV), respectively.<sup>166-169</sup> The various Ge oxidation states are observed at similar positions before and after the etching. After the etching, the decrease in the intensity of germanium oxide peaks can be due to the oxide reduction by the TMA reactant. In the literature, a partial reduction of the underlying germanium oxide after  $Al_2O_3$  ALD (using TMA- $H_2O$  at 300 °C) has been reported.<sup>170</sup>

Figure 4.23 b) compares the Si 2p XPS spectra of the SiGe film before and

after 100 cycles of ALEt. The elemental Si 2p peak is observed at 99.5 eV.<sup>167</sup> Similar to germanium, a strong Si peak around 103.5 eV is detected and assigned to  $SiGeO_x$ .<sup>167</sup> On the contrary, after ALEt, the high intensity Si 2p peak at  $102.91 \pm 0.1$  eV is assigned to  $Si^{4+}$  and can be a result of an oxidation step according to **O1**. The shifts in the binding energy for  $Si^{1+}$ ,  $Si^{2+}$ ,  $Si^{3+}$ , and  $Si^{4+}$  with regards to the binding energy of  $Si^0$  are reported as 0.9, 1.9, 2.6, and 3.4 eV, respectively.<sup>171,172</sup> From the figure, it is evident that the  $Si^{2+}$  and  $Si^{3+}$  oxidation states are much more intense after ALEt. The  $Si^{3+}$  peak around 102 eV indicates the presence of a silicon suboxide.<sup>173</sup> After ALEt, the higher intensities (compared with before ALEt) detected for silicon suboxides (associated with  $Si^{3+}$ ,  $Si^{2+}$ , and  $Si^{1+}$ ) can be explained by the partial reduction of  $SiO_2$  by TMA as reported by DuMont et al.<sup>74</sup> Moreover, the possibility of  $SiO_xF_y$  cannot be ruled out, as it may have formed in the reaction between  $SiO_2$  and the HF vapors. Previous reports have confirmed the formation of  $SiO_xF_y$  during the ALEt of  $SiO_2$  by HF-TMA.<sup>74</sup> Thus Si peaks at  $102.8 \pm 0.4$  and 103.9 eV are assigned to  $SiO_xF_y$  surface species.<sup>174</sup>

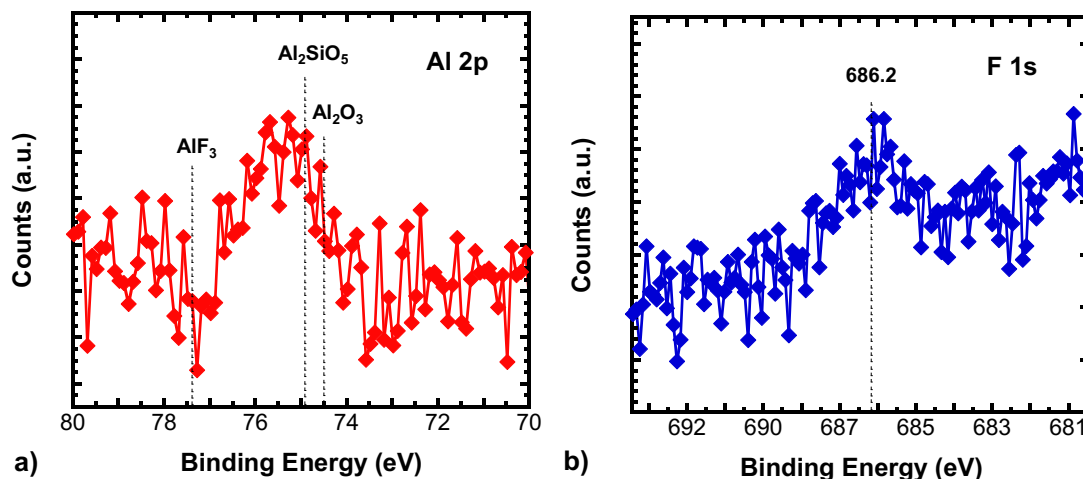


Figure 4.24: XPS spectrum of a) Al 2p, and b) F 1s signals for SiGe film before and after 100 cycles of the  $O_2$  - HF - TMA ALEt process at 290 °C. Reproduced with permission from [II], Copyright © 2021 American Vacuum Society.

After etching the SiGe film, small but non-negligible amounts of aluminum and fluorine were also detected, as shown in Figure 4.24. The aluminum and fluorine contents were 1.0 and 0.8 atomic %, respectively. In Figure 4.24 a) an Al 2p peak is observed at  $75.4 (\pm 0.1)$  eV which is higher than the BE of  $Al_2O_3$  (74.5 eV) but lower than the BE of  $AlF_3$  (77.3 eV).<sup>175</sup> The Al 2p XPS peaks in  $AlF_3$  and  $AlO_xF_y$  are centered around  $77 (\pm 0.5)$  eV<sup>59,142,175</sup> and 75.5 eV,<sup>48</sup> respectively. The BE of aluminosilicate ( $Al_2SiO_5$ ) is reported around 74.9 eV.<sup>176</sup> Hence, the BE of the observed Al peak is consistent with  $AlO_xF_y$  species.<sup>177-179</sup>

In Figure 4.24 b) the F 1s signal demonstrates a maximum around 686.2 eV that belongs to either SiF or GeF surface species.<sup>179</sup> When combined with the detected BEs for Al, Si, and Ge, it can be concluded that the surface lacks  $AlF_3$  species and most likely contains a mix of  $SiGeO_xF_y$ , aluminosilicate and  $AlO_xF_y$  species.

## 4.5 HfO<sub>2</sub> etching by NbF<sub>5</sub>-CCl<sub>4</sub>

Since there was only a limited number of HfO<sub>2</sub> wafers available at the time of experiments, only a few HfO<sub>2</sub> films were subjected to the NbF<sub>5</sub>-CCl<sub>4</sub> etch chemistry (unpublished results). The etch experiments were carried out at 460 °C and the pulsing sequence was NbF<sub>5</sub>/N<sub>2</sub>/CCl<sub>4</sub>/N<sub>2</sub>. Section 4.5.1 plots the EPC at various reactant pulse times. Section 4.5.2 discusses the basic thermodynamics of the etch chemistry and in 4.5.3 the post-etch films are characterized by ex-situ TEM and XPS analyses.

### 4.5.1 Effect of reactant pulse times

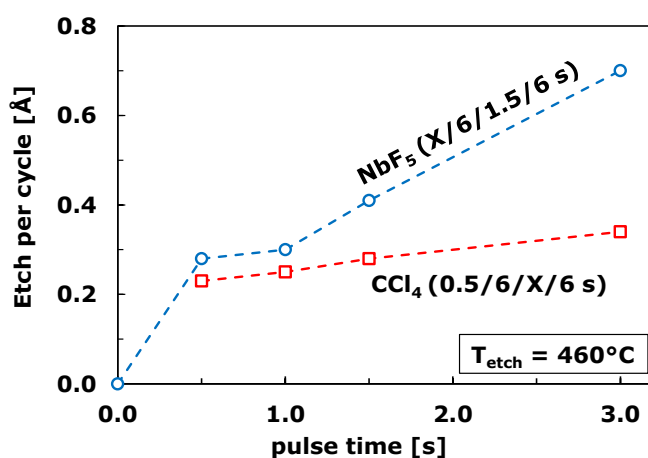


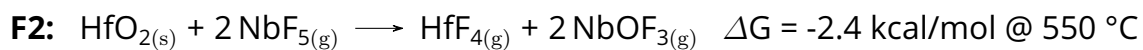
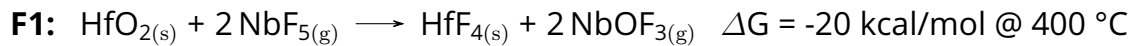
Figure 4.25: EPC of HfO<sub>2</sub> films vs. NbF<sub>5</sub> and CCl<sub>4</sub> pulse times at 460 °C. A total of 100 etch cycles were performed for each data point, except for 3/6/1.5/6 s, where only 50 etch cycles were used. Copyright © 2022 Author.

The HfO<sub>2</sub> films were etched using alternate exposures of NbF<sub>5</sub> and CCl<sub>4</sub>. The EPC depends on the reactant pulse times (Figure 4.25). While varying the NbF<sub>5</sub> pulse time (blue curve), the CCl<sub>4</sub> pulse time was fixed at 1.5 s. The EPC of 0.3 Å for 0.5 s NbF<sub>5</sub> pulse is noted. The EPC increases with an increase in the NbF<sub>5</sub> pulse time and no sign of saturation is observed up to 3.0 s. This non-saturating EPC is explained by the continuous formation of HfO<sub>x</sub>F<sub>y</sub> layer as long as the NbF<sub>5</sub> molecules are available. Similarly, HfO<sub>2</sub> was fluorinated using HF at 450 °C and the conversion took about 30 minutes before saturation was observed.<sup>180</sup>

On the contrary, while varying the CCl<sub>4</sub> pulse time from 0.5 to 3.0 s, a saturated EPC of about 0.3 Å is obtained. The chloride ions from CCl<sub>4</sub> are proposed to undergo halide-exchange with the fluoride species on the modified surface, thereby forming volatile species. In this way, the volatilization of the modified HfO<sub>x</sub>F<sub>y</sub> surface occurs. The volatilization continues as long as the modified layer (HfO<sub>x</sub>F<sub>y</sub>) and CCl<sub>4</sub> are in contact and stops when either the CCl<sub>4</sub> supply is ceased or the underneath HfO<sub>2</sub> becomes exposed. No etching of HfO<sub>2</sub> was observed with CCl<sub>4</sub> alone. Hence, the saturation of EPC with CCl<sub>4</sub> pulse time is observed.

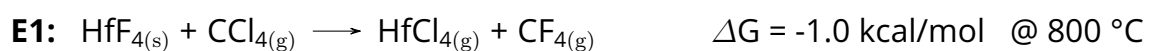
### 4.5.2 Thermodynamics of the etch chemistry

Similar to the Al<sub>2</sub>O<sub>3</sub> ALEt by NbF<sub>5</sub>-CCl<sub>4</sub>, HfO<sub>2</sub> etching is proposed to involve fluorination by NbF<sub>5</sub> followed by the volatilization (halide-exchange reaction) of the products upon reaction with CCl<sub>4</sub>. Fluorination reactions can be written as **F1** and **F2** below.



In **F1**, HfO<sub>2</sub> is converted to HfF<sub>4</sub>, and the oxygen from HfO<sub>2</sub> is scavenged by NbF<sub>5</sub> in the form of volatile NbOF<sub>3</sub> species. NbOF<sub>3</sub> sublimates above 148 °C.<sup>120</sup> According to **F1**, the negative value of ΔG at 400 °C shows that the fluorination reaction is favourable. In contrast, **F2** shows the capability of NbF<sub>5</sub> to convert HfO<sub>2</sub> into gaseous HfF<sub>4</sub> at 550 °C. ΔG for **F2** becomes negative above 515 °C, so it can be said that NbF<sub>5</sub> alone may result in volatilization of HfO<sub>2</sub> films at higher temperatures (> 515 °C). Moreover, HfF<sub>4</sub> sublimation is recorded to occur only above 600 °C.<sup>180</sup> The etch temperature used in the ALEt experiments was at maximum 460 °C. Another possibility is that under experimental conditions HfO<sub>2</sub> undergoes only partial fluorination, i.e., the modified layer is HfO<sub>x</sub>F<sub>y</sub>, similar to the observation made for Al<sub>2</sub>O<sub>3</sub> fluorination, where the modified layer was AlO<sub>x</sub>F<sub>y</sub>. Hf<sub>2</sub>O<sub>6</sub> as an intermediate is reported to form during the fluorination of HfO<sub>2</sub> by HF at temperatures above 400 °C.<sup>180</sup>

In the halide-exchange step, the fluorinated HfO<sub>2</sub> reacts with CCl<sub>4</sub> which can be described using **E1**.



In **E1**, the fluoride ions from HfF<sub>4</sub> transfer to the carbon atom of CCl<sub>4</sub> to form volatile CF<sub>4</sub>. Mixed halides such as CClF<sub>3</sub>, CCl<sub>2</sub>F<sub>2</sub> and CCl<sub>3</sub>F may also form as by-products. On the other hand, mixed halogen containing Hf(+4) compounds (HfF<sub>a</sub>Cl<sub>4-a</sub> where 0 < a ≤ 3) that are likely more volatile than HfF<sub>4</sub> can also form. ΔG for **E1** becomes negative only at about 800 °C, which could indicate that the mixed halide species are the dominant etch products. Calculating the ΔG values for reactions producing mixed halides was not possible due to the absence of such species in the HSC software database.

### 4.5.3 Post-etch film characterization

After exposing HfO<sub>2</sub> films to the NbF<sub>5</sub>-CCl<sub>4</sub> chemistry the remaining surfaces were characterized using TEM and XPS. Etching was carried out at 460 °C and the etch process utilized 3 s reactant pulses and 6 s N<sub>2</sub> purges. Total numbers of etch cycles employed were 60 and 150 in Figure 4.26 a) and b), respectively.

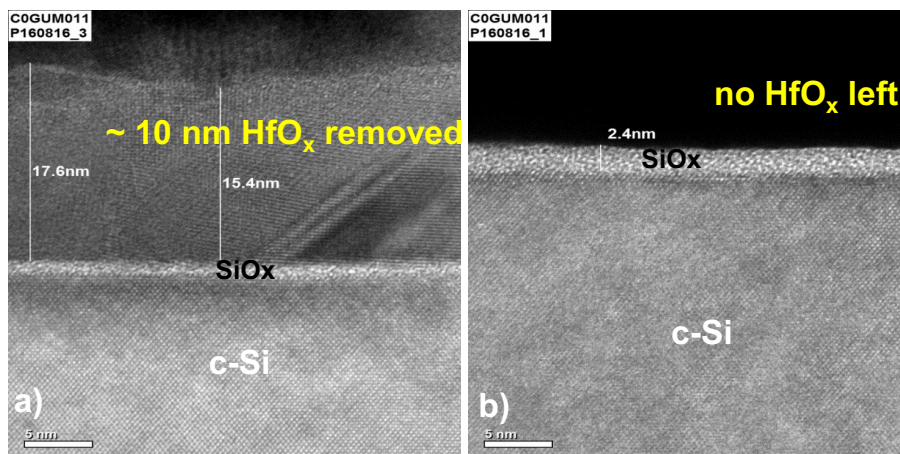


Figure 4.26: Bright-field TEM images of: a) partially etched 17 nm  $\text{HfO}_2$ , and b) silicon substrate with native oxide after complete removal of  $\text{HfO}_2$ . The etchant pulse times used were 3 s and the etch temperature was kept at 460 °C.

The initial thickness of the  $\text{HfO}_2$  was approximately 27 nm and the films were crystalline (not shown here).

In Figure 4.26 a), about 17 nm  $\text{HfO}_2$  film is visible that is crystalline and the surface appears to be roughened. Figure 4.26 b) shows the c-Si substrate with native oxide after complete removal of the  $\text{HfO}_2$  film.

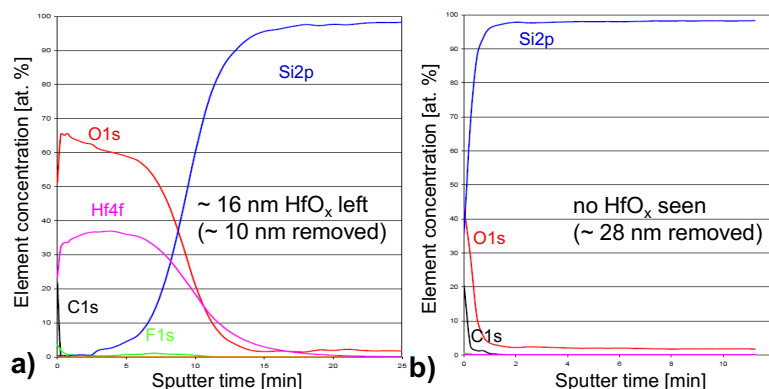


Figure 4.27: XPS depth profiles of: a) partially etched  $\text{HfO}_2$  film, b) silicon surface after complete etching of  $\text{HfO}_2$  with the  $\text{NbF}_5\text{-CCl}_4$  etch chemistry. The etch temperature was 460 °C.

Figure 4.27 a) shows the elemental composition of the film that was left after etching about 10 nm  $\text{HfO}_2$ . The surface is comprised of about 24 atomic % Hf, 51 atomic % O, 22 atomic % C and 3 atomic % F. The Nb and Cl were not detected in the remaining film or at the surface. The amount of fluorine in the remaining film is less than 0.7 atomic % which is possibly a result of sputtering. The high amount of surface carbon (22 atomic %) is associated with the exposure to ambient air during sample storage and transportation or partly with the exposure to  $\text{CCl}_4$ .

Figure 4.27 b) shows that after a complete removal of about 28 nm  $\text{HfO}_2$  film, the surface contains no signs of Hf, Nb and Cl. The amount of F

detected is less than 0.5 atomic %. The XPS analyses reveal that the surface is composed of Si and O along with some carbon contamination and hence, confirms the underlying substrate (c-Si surface with native oxide).

## 4.6 Activation energy determination

In a chemical etch process, the rate of the reaction is determined by the slowest step and strongly depends on the temperature. For single reactant based processes, such as CVE or GPPE, the rate determining step can be the etching reaction or transportation of the etchant or product. Typically, the reaction (etch) rates are low at low temperatures and increase exponentially with temperature according to the Arrhenius equation 4.6a.<sup>7,181,182</sup>

$$k = Ae^{\frac{-E_a}{RT}} \quad (4.6a)$$

Where ' $k$ ' is the reaction rate constant, ' $E_a$ ' is the activation energy, ' $T$ ' is the temperature in Kelvin, ' $R$ ' is the universal gas constant, and ' $A$ ' is pre-exponential factor. Under a given set of experimental conditions, the activation energy is the minimum energy that is needed for the reactants to result in the formation of products, in this case etch-products, and hence, the etching to take place.

In the case of an ideal self-limiting ALEt process based on two reactants, the EPC should have a temperature-independent response. However, this is rarely reported in the literature, and the experimental findings in this thesis also showed that the EPCs increase with the temperature. In reality, the EPCs may depend on the rate of the surface modification or volatilization step. However, the results reported here indicate that it is the surface modification step that derives the increase in the EPCs. In the literature, the surface modification steps such as oxidation<sup>183</sup> and diffusion<sup>184</sup> are reported to follow linear Arrhenius plots.

$$\ln(k) = \frac{-E_a}{RT} + \ln(A) \quad (4.6b)$$

To confirm whether the etch processes studied here follow the Arrhenius equation 4.6b, the natural logarithms of EPCs are plotted against the inverse of the temperature (Figure 4.28). Similarly, activation energies for the gas-solid reactions were determined in the previous reports.<sup>52,185</sup> Here, all the plots are indeed linear, and the following activation energies are determined from the slopes:

- (A) Al<sub>2</sub>O<sub>3</sub> etching by NbF<sub>5</sub>-CCl<sub>4</sub>: 33 kcal/mol
- (B) TiN etching by CCl<sub>4</sub>: 17 kcal/mol
- (C) TiN etching by SOCl<sub>2</sub>: 25 kcal/mol
- (D) SiGe etching by O<sub>2</sub>/O<sub>3</sub>-HF-TMA: 16 kcal/mol

Similar calculations were made for determining the activation energies of the AlF<sub>3</sub> and WO<sub>3</sub> ALEt reactions by AlMe<sub>2</sub>Cl and BCl<sub>3</sub>/HF, and were reported to be 28 and 9 kcal/mol, respectively.<sup>14,20,48</sup>



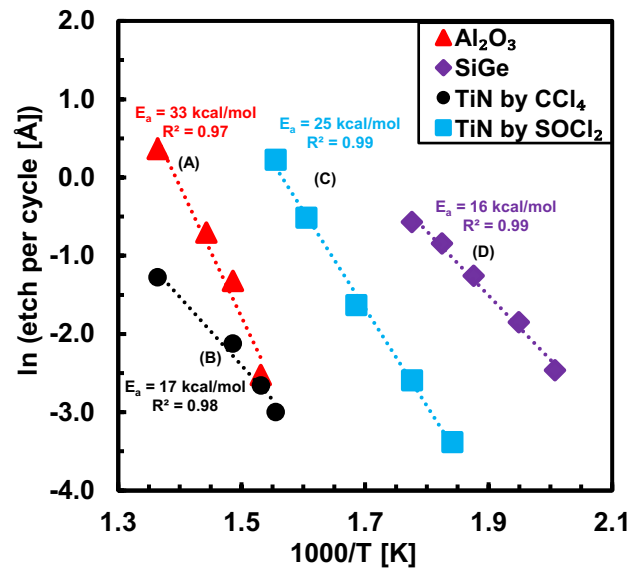


Figure 4.28: Arrhenius plots of the etch per cycle of  $\text{Al}_2\text{O}_3$  (A) etching by  $\text{NbF}_5$  -  $\text{CCl}_4$  (red), TiN (B) etching by  $\text{CCl}_4$  (black), TiN (C) etching by  $\text{SOCl}_2$  (blue) [I], and SiGe (D) etching by  $\text{O}_2$  - HF - TMA (purple) [II]. In the figure  $E_a$  (SiGe) reproduced with permission from [II], Copyright © 2021 American Vacuum Society, and  $E_a$  (TiN by  $\text{SOCl}_2$ ) reproduced with permission from [I], Copyright © 2021 Authors, Published by Elsevier, distributed under a Creative Commons (CC BY-NC-ND) License.



## Chapter 5: Conclusions and outlook

Thermal atomic level etching is a chemical etching technique that relies on sequential gas-surface reactions that are thermally activated and provide ångström-level thickness control. The work reported here is based on novel reactants such as  $\text{NbF}_5$ ,  $\text{CCl}_4$ , and  $\text{SOCl}_2$  as well as previously reported  $\text{O}_2/\text{O}_3$ , HF, and  $\text{Al}(\text{CH}_3)_3$ . In this work, two types of etching processes are reported. The first one includes exposing the target surface to two or more reactants in a cyclic manner (thermal atomic layer etching, ALEt) and the second one utilizes pulsing of a single reactant (gas phase pulsed etching, GPPE). All reactant pulses were separated by inert gas purge steps.

Etching of amorphous  $\text{Al}_2\text{O}_3$  was performed using alternate exposures of  $\text{NbF}_5$  and  $\text{CCl}_4$  reactants, and occurred above  $380^\circ\text{C}$ . The  $\text{Al}_2\text{O}_3$  ALEt proceeds by a two-step mechanism wherein  $\text{NbF}_5$  fluorinates a part of the  $\text{Al}_2\text{O}_3$  layer into  $\text{AlF}_x[\text{O}]$  and  $\text{CCl}_4$  volatilizes the  $\text{AlF}_x[\text{O}]$  layer via a halide-exchange reaction. The proposed etch-products are  $\text{AlCl}_3$ ,  $\text{NbOF}_3$ , and  $\text{CFCl}_3$ . It was found that the fluorination step is not self-limiting but the volatilization step leads to a partially self-limiting etch per cycle (EPC) response. EPC increased with temperature and an EPC of  $1.4 \text{ \AA}$  was obtained at  $460^\circ\text{C}$ . At  $460^\circ\text{C}$  the  $\text{NbF}_5$ - $\text{CCl}_4$  chemistry etched also crystalline  $\text{HfO}_2$  but not  $\text{SiO}_2$  and  $\text{Si}_3\text{N}_4$ . Moreover, TiN was fluorinated by  $\text{NbF}_5$  and the formed  $\text{NbNF}_x$  species did not desorb from the surface under the experimental conditions. In the removal step,  $\text{CCl}_4$  volatilized the modified surface layer by forming volatile  $\text{TiF}_4$ ,  $\text{TiCl}_4$ ,  $\text{NbFCl}_3$ , and  $\text{ClCN}$  products. Hence, TiN,  $\text{HfO}_2$  and  $\text{Al}_2\text{O}_3$  are etched selectively over  $\text{SiO}_2$  and  $\text{Si}_3\text{N}_4$ .

In the GPPE, TiN was etched by either  $\text{CCl}_4$  or  $\text{SOCl}_2$  alone. In the case of GPPE by  $\text{CCl}_4$ , EPCs of about  $0.1$  and  $0.3 \text{ \AA}$  were obtained at  $370$  and  $460^\circ\text{C}$ , respectively. The predicted etch products are  $\text{TiCl}_3$  and  $\text{ClCN}$ .  $\text{SOCl}_2$  was able to etch TiN starting from  $270^\circ\text{C}$ . The proposed etch products are  $\text{TiCl}_4$ ,  $\text{SO}_2$ ,  $\text{N}_2$  and  $\text{S}_2\text{Cl}_2$ . Both GPPE processes selectively etch TiN over  $\text{SiO}_2$ ,  $\text{Si}_3\text{N}_4$ , and  $\text{Al}_2\text{O}_3$ .

SiGe was etched using an oxidation and conversion-etch mechanism. In the oxidation step, SiGe is converted to  $\text{SiGeO}_x$  using either  $\text{O}_2$  or  $\text{O}_3/\text{O}_2$ . The oxidation step shows partially self-limiting EPC while saturated EPC is found with respect to HF and TMA pulse times. An EPC of  $0.6 \text{ \AA}$  for  $\text{O}_2$ -HF-TMA and  $0.4 \text{ \AA}$  for  $\text{O}_3$ -HF-TMA etch process at  $290^\circ\text{C}$  were observed.

For both ALEt and GPPE processes, uniform and conformal thinning as well as complete removal of TiN from 3D structures were demonstrated. Moreover, after the complete removal of the target films, negligible amounts ( $\approx 0.5$  atomic %) of surface remnants were observed.

In the future, effects of the reactant partial pressures, substrate composition, morphology and phase of the target material on the EPC should be studied. In addition, the etch chemistries used here should be tested on other targets such as  $\text{TiO}_2$ ,  $\text{ZrO}_2$ ,  $\text{Ta}_2\text{O}_5$ ,  $\text{Nb}_2\text{O}_5$ , ZrN, TaN, MoN, and AlN. Furthermore, because the reactants contain various halide atoms, it would be beneficial to investigate the process-hardware compatibility.



# Bibliography

- [1] M. Ritala and J. Niinistö, Industrial Applications of Atomic Layer Deposition, *ECS Transactions*, 2019, **25**, 641–652.
- [2] V. Miikkulainen, M. Leskelä, M. Ritala and R. L. Puurunen, Crystallinity of inorganic films grown by atomic layer deposition: Overview and general trends, *Journal of Applied Physics*, 2013, **113**, 021301.
- [3] R. W. Johnson, A. Hultqvist and S. F. Bent, A brief review of atomic layer deposition: from fundamentals to applications, *Materials Today*, 2014, **17**, 236–246.
- [4] S. M. Irving, K. E. Lemons and G. E. Bobos, *Gas plasma vapor etching process*, 1969, US Patent 3,615,956.
- [5] S. M. Irving, A Plasma Oxidation Process For Removing Photoresist Films, *Solid State technology*, 1971, **14**, 47–51.
- [6] M. N. Yoder, *Atomic layer etching*, 1987, US Patent 4,756,794A.
- [7] K. J. Kanarik, T. Lill, E. A. Hudson, S. Sriraman, S. Tan, J. Marks, V. Vahedi and R. A. Gottscho, Overview of atomic layer etching in the semiconductor industry, *Journal of Vacuum Science & Technology A*, 2015, **33**, 020802.
- [8] A. Goda, Recent Progress on 3D NAND Flash Technologies, *Electronics*, 2021, **10**, 3156.
- [9] J. Ryckaert, M. H. Na, P. Weckx, D. Jang, P. Schuddinck, B. Chehab, S. Patli, S. Sarkar, O. Zografos, R. Baert and D. Verkest, Enabling Sub-5nm CMOS Technology Scaling Thinner and Taller!, *IEEE International Electron Devices Meeting (IEDM)*, 2019, 29.4.1–29.4.4.
- [10] S. Zhang, Z. Li, H. Zhou, R. Li, S. Wang, K.-W. Paik and P. He, Challenges and recent perspectives of 3D heterogeneous integration, *Advances in Electrical Engineering, Electronics and Energy*, 2022, **2**, 100052.
- [11] A. Veloso, T. Huynh-Bao, P. Matagne, D. Jang, G. Eneman, N. Horiguchi and J. Ryckaert, Nanowire & nanosheet FETs for ultra-scaled, high-density logic and memory applications, *Solid-State Electronics*, 2020, **168**, 107736.
- [12] K. Nayak, M. Bajaj, A. Konar, P. J. Oldiges, K. Natori, H. Iwai, K. V. R. M. Murali and V. R. Rao, CMOS Logic Device and Circuit Performance of Si Gate All Around Nanowire MOSFET, *IEEE Transactions on Electron Devices*, 2014, **61**, 3066–3074.
- [13] I. Seiichi, *Atomic layer etching method*, 1981, Japan Patent JPS5898929A, JPH0379862B2; filed by Suwa Seikosha KK.

- [14] Y. Lee, J. W. DuMont and S. M. George, Atomic Layer Etching of  $\text{AlF}_3$  Using Sequential, Self-Limiting Thermal Reactions with  $\text{Sn}(\text{acac})_2$  and Hydrogen Fluoride, *The Journal of Physical Chemistry C*, 2015, **119**, 25385–25393.
- [15] S. M. George, Mechanisms of Thermal Atomic Layer Etching, *Accounts of Chemical Research*, 2020, **53**, 1151–1160.
- [16] C. T. Carver, J. J. Plombon, P. E. Romero, S. Suri, T. A. Tronic and R. B. Turkot, Atomic Layer Etching: An Industry Perspective, *ECS Journal of Solid State Science and Technology*, 2015, **4**, N5005–N5009.
- [17] A. Fischer, A. Routzahn, S. M. George and T. Lill, Thermal atomic layer etching: A review, *Journal of Vacuum Science & Technology A*, 2021, **39**, 030801.
- [18] A. Agarwal and M. J. Kushner, Plasma atomic layer etching using conventional plasma equipment, *Journal of Vacuum Science & Technology A*, 2009, **27**, 37–50.
- [19] A. Agarwal and M. Kushner, Plasma atomic layer etching, *The 33rd IEEE International Conference on Plasma Science*, 2006, 469–469.
- [20] N. Johnson and S. M. George,  $\text{WO}_3$  and W Thermal Atomic Layer Etching Using “Conversion-Fluorination” and “Oxidation-Conversion-Fluorination” Mechanisms, *ACS Applied Materials & Interfaces*, 2017, **9**, 34435–34447.
- [21] W. Xie and G. N. Parsons, Thermal atomic layer etching of metallic tungsten via oxidation and etch reaction mechanism using  $\text{O}_2$  or  $\text{O}_3$  for oxidation and  $\text{WCl}_6$  as the chlorinating etchant, *Journal of Vacuum Science & Technology A*, 2020, **38**, 022605.
- [22] J. W. Coburn and H. F. Winters, Plasma etching—A discussion of mechanisms, *Journal of Vacuum Science and Technology*, 1979, **16**, 391–403.
- [23] K. Shinoda, N. Miyoshi, H. Kobayashi, M. Izawa, K. Ishikawa and M. Hori, Rapid thermal-cyclic atomic-layer etching of titanium nitride in  $\text{CHF}_3/\text{O}_2$  downstream plasma, *Journal of Physics D: Applied Physics*, 2019, **52**, 475106.
- [24] F. Roozeboom, ALD & ALE: two similar biotopes in atomic-layer dry and wet processing, *8th RAFALD Workshop, Caen (France)*, 2022.
- [25] J. Kim, T. S. Koga, H. P. Gillis, M. S. Goorsky, G. A. Garwood, J. B. Varesi, D. R. Rhiger and S. M. Johnson, Low-energy electron-enhanced etching of  $\text{HgCdTe}$ , *Journal of Electronic Materials*, 2003, **32**, 677–685.
- [26] H. P. Gillis, J. L. Clemons and J. P. Chamberlain, Low-energy electron beam enhanced etching of  $\text{Si}(100)\text{-(}2\times 1\text{)}$  by molecular hydrogen, *Journal of Vacuum Science & Technology B Microelectronics and Nanometer Structures*, 1992, **10**, 2729–2733.

- [27] H. P. Gillis, D. A. Choutov, P. A. S. IV, J. D. Piper, J. H. Crouch, P. M. Dove and K. P. Martin, Low energy electron-enhanced etching of Si(100) in hydrogen/helium direct-current plasma, *Applied Physics Letters*, 1995, **66**, 2475–2477.
- [28] H. P. Gillis, D. A. Choutov, K. P. Martin and L. Song, Low energy electron-enhanced etching of GaAs(100) in a chlorine/hydrogen dc plasma, *Applied Physics Letters*, 1996, **68**, 2255–2257.
- [29] J. W. Coburn and H. F. Winters, Ion- and electron-assisted gas-surface chemistry—An important effect in plasma etching, *Journal of Applied Physics*, 1979, **50**, 3189–3196.
- [30] X. Wang and S. Samukawa, in *Micro LEDs*, ed. H. Jiang and J. Lin, Elsevier, 2021, vol. 106 of Semiconductors and Semimetals, pp. 203–221.
- [31] H. Shin, W. Zhu, L. Liu, V. M. Sridhar, Shyam; Donnelly, D. J. Economou, C. Lenox and T. Lii, Selective etching of TiN over TaN and vice versa in chlorine-containing plasmas, *Journal of Vacuum Science & Technology A Vacuum Surfaces and Films*, 2013, **31**, 031305.
- [32] B. M. Coffey, H. C. Nallan, J. R. Engstrom, C. H. Lam and J. G. Ekerdt, Vacuum Ultraviolet-Enhanced Oxidation—A Route to the Atomic Layer Etching of Palladium Metal, *Chemistry of Materials*, 2020, **32**, 6035–6042.
- [33] B. M. Coffey, H. C. Nallan and J. G. Ekerdt, Vacuum ultraviolet enhanced atomic layer etching of ruthenium films, *Journal of Vacuum Science & Technology A*, 2021, **39**, 012601.
- [34] U. Streller, B. Li, A. Krabbe, H. Krause, I. Twesten and N. Schwentner, Photochemical etching with tunable VUV radiation, *Journal of Electron Spectroscopy and Related Phenomena*, 1996, **80**, 49–54.
- [35] H. Shin, W. Zhu, V. M. Donnelly and D. J. Economou, Surprising importance of photo-assisted etching of silicon in chlorine-containing plasmas, *Journal of Vacuum Science & Technology A*, 2012, **30**, 021306.
- [36] S. Sakurai and T. Nakayama, Adsorption, diffusion and desorption of Cl atoms on Si(111) surfaces, *Journal of Crystal Growth*, 2002, **237-239**, 212–216.
- [37] G. Oehrlein, D. Metzler and C. Li, Atomic Layer Etching at the Tipping Point: An Overview, *ECS Journal of Solid State Science and Technology*, 2015, **4**, N5041–N5053.
- [38] Y. Lee, J. W. DuMont and S. M. George, Atomic Layer Etching of HfO<sub>2</sub> Using Sequential, Self-Limiting Thermal Reactions with Sn(acac)<sub>2</sub> and HF, *ECS Journal of Solid State Science and Technology*, 2015, **4**, N5013–N5022.
- [39] Y. Lee, J. W. DuMont and S. M. George, Mechanism of Thermal Al<sub>2</sub>O<sub>3</sub> Atomic Layer Etching Using Sequential Reactions with Sn(acac)<sub>2</sub> and HF, *Chemistry of Materials*, 2015, **27**, 3648–3657.

- [40] Y. Lee, J. W. DuMont and S. M. George, Trimethylaluminum as the Metal Precursor for the Atomic Layer Etching of  $\text{Al}_2\text{O}_3$  Using Sequential, Self-Limiting Thermal Reactions, *Chemistry of Materials*, 2016, **28**, 2994–3003.
- [41] S. M. Hu, Defects in silicon substrates, *Journal of Vacuum Science and Technology*, 1977, **14**, 17–31.
- [42] S. D. Athavale and D. J. Economou, Molecular dynamics simulation of atomic layer etching of silicon, *Journal of Vacuum Science & Technology A*, 1995, **13**, 966–971.
- [43] X. Ma, S. Zhang, Z. Dai and Y. Wang, Study on atomic layer etching of Si in inductively coupled Ar/ $\text{Cl}_2$  plasmas driven by tailored bias waveforms, *Plasma Science and Technology*, 2017, **19**, 085502.
- [44] Y. Lee, C. Huffman and S. M. George, Selectivity in Thermal Atomic Layer Etching Using Sequential, Self-Limiting Fluorination and Ligand-Exchange Reactions, *Chemistry of Materials*, 2016, **28**, 7657–7665.
- [45] J. W. Clancey, A. S. Cavanagh, J. E. T. Smith, S. Sharma and S. M. George, Volatile Etch Species Produced During Thermal  $\text{Al}_2\text{O}_3$  Atomic Layer Etching, *The Journal of Physical Chemistry C*, 2020, **124**, 287–299.
- [46] H. F. Winters and J. W. Coburn, The etching of silicon with  $\text{XeF}_2$  vapor, *Applied Physics Letters*, 1979, **34**, 70–73.
- [47] P. C. Lemaire and G. N. Parsons, Thermal Selective Vapor Etching of  $\text{TiO}_2$ : Chemical Vapor Etching via  $\text{WF}_6$  and Self-Limiting Atomic Layer Etching Using  $\text{WF}_6$  and  $\text{BCl}_3$ , *Chemistry of Materials*, 2017, **29**, 6653–6665.
- [48] A. Fischer, A. Routzahn, Y. Lee, T. Lill and S. M. George, Thermal etching of  $\text{AlF}_3$  and thermal atomic layer etching of  $\text{Al}_2\text{O}_3$ , *Journal of Vacuum Science & Technology A*, 2020, **38**, 022603.
- [49] K. Ikeda, S. Imai and M. Matsumura, Atomic layer etching of germanium, *Applied Surface Science*, 1997, **112**, 87–91.
- [50] X.-Q. Wang, X. Yang, K. Walsh and Y.-C. Tai, Proceedings of International Solid State Sensors and Actuators Conference (Transducers '97), 1997, pp. 1505–1508.
- [51] I. Chan, K. Brown, R. Lawson, A. Robinson, Y. Ma and D. Strembecke, Engineering Solutions for the Next Millennium. 1999 IEEE Canadian Conference on Electrical and Computer Engineering (Cat. No.99TH8411), 1999, pp. 1637–1642.
- [52] A. Okubora, J. Kasahara, M. Arai and N. Watanabe, Thermal etching of GaAs by hydrogen under arsenic overpressure, *Journal of Applied Physics*, 1986, **60**, 1501–1504.
- [53] N. Miki, H. Kikuyama, I. Kawanabe, M. Miyashita and T. Ohmi, Gas-phase selective etching of native oxide, *IEEE Transactions on Electron Devices*, 1990, **37**, 107–115.



- [54] W. I. Jang, C. A. Choi, M. L. Lee, C. H. Jun and Y. T. Kim, Fabrication of MEMS devices by using anhydrous HF gas-phase etching with alcoholic vapor, *Journal of Micromechanics and Microengineering*, 2002, **12**, 297–306.
- [55] D. E. Ibbotson, J. A. Mucha, D. L. Flamm and J. M. Cook, Plasmaless dry etching of silicon with fluorine-containing compounds, *Journal of Applied Physics*, 1984, **56**, 2939–2942.
- [56] D. B. Mawhinney, V. Naumenko, A. Kuznetsova, J. T. Yates, J. Liu and R. E. Smalley, Infrared Spectral Evidence for the Etching of Carbon Nanotubes Ozone Oxidation at 298 K, *Journal of the American Chemical Society*, 2000, **122**, 2383–2384.
- [57] J. Zhao, M. Konh and A. Teplyakov, Surface chemistry of thermal dry etching of cobalt thin films using hexafluoroacetylacetone (Hhfac), *Applied Surface Science*, 2018, **455**, 438–445.
- [58] S.-W. Kang, H.-U. Kim and S.-W. Rhee, Dry etching of copper film with hexafluoroacetylacetone via oxidation process, *Journal of Vacuum Science & Technology B: Microelectronics and Nanometer Structures Processing, Measurement, and Phenomena*, 1999, **17**, 154–157.
- [59] A. M. Cano, J. L. Partridge and S. M. George, Thermal Atomic Layer Etching of Al<sub>2</sub>O<sub>3</sub> Using Sequential HF and BCl<sub>3</sub> Exposures: Evidence for Combined Ligand-Exchange and Conversion Mechanisms, *Chemistry of Materials*, 2022, **34**, 6440–6449.
- [60] D. R. Zywotko, J. Faguet and S. M. George, Rapid atomic layer etching of Al<sub>2</sub>O<sub>3</sub> using sequential exposures of hydrogen fluoride and trimethylaluminum with no purging, *Journal of Vacuum Science & Technology A*, 2018, **36**, 061508.
- [61] J. A. Murdzek and S. M. George, Effect of crystallinity on thermal atomic layer etching of hafnium oxide, zirconium oxide, and hafnium zirconium oxide, *Journal of Vacuum Science & Technology A*, 2020, **38**, 022608.
- [62] A. M. Cano, A. Lii-Rosales and S. M. George, Thermal Atomic Layer Etching of Aluminum Nitride Using HF or XeF<sub>2</sub> for Fluorination and BCl<sub>3</sub> for Ligand Exchange, *The Journal of Physical Chemistry C*, 2022, **126**, 6990–6999.
- [63] T. Faraz, F. Roozeboom, H. C. M. Knoop and W. M. M. Kessels, Atomic Layer Etching: What Can We Learn from Atomic Layer Deposition?, *ECS Journal of Solid State Science and Technology*, 2015, **4**, N5023–N5032.
- [64] S. K. Laney, T. Li, M. Michalska, F. Ramirez, M. Portnoi, J. Oh, M. K. Tiwari, I. G. Thayne, I. P. Parkin and I. Papakonstantinou, Spacer-Defined Intrinsic Multiple Patterning, *ACS Nano*, 2020, **14**, 12091–12100.

- [65] M. Shen, J. Hoang, H. Chi, D. Qian, G. Papasouliotis, J. Church, P. Subramonium, E. Hudson, L. Belau, K. Haynes, M. Weimer, R. Puthenkivilakam, S. Reddy, S. Bhadauriya and T. Lill, Advanced Etch Technology and Process Integration for Nanopatterning X, 2021, p. 1161508.
- [66] K. Oyama, 2018 China Semiconductor Technology International Conference (CSTIC), 2018, pp. 1–2.
- [67] Y. Lee, N. R. Johnson and S. M. George, Thermal Atomic Layer Etching of Gallium Oxide Using Sequential Exposures of HF and Various Metal Precursors, *Chemistry of Materials*, 2020, **32**, 5937–5948.
- [68] M. Bonvalot, C. Vallée, C. Mannequin, M. Jaffal, R. Gassilloud, N. Possémé and T. Chevolleau, Area selective deposition using alternate deposition and etch super-cycle strategies, *Dalton Transactions*, 2022, **51**, 442–450.
- [69] R. Rahman, E. C. Mattson, J. P. Klesko, A. Dangerfield, S. Rivillon-Amy, D. C. Smith, D. Hausmann and Y. J. Chabal, Thermal Atomic Layer Etching of Silica and Alumina Thin Films Using Trimethylaluminum with Hydrogen Fluoride or Fluoroform, *ACS Applied Materials & Interfaces*, 2018, **10**, 31784–31794.
- [70] C. Fang, Y. Cao, D. Wu and A. Li, Thermal atomic layer etching: Mechanism, materials and prospects, *Progress in Natural Science*, 2018, **28**, 667–675.
- [71] Y. Tsai, Z. Li and S. Hu, Recent Progress of Atomic Layer Technology in Spintronics: Mechanism, Materials and Prospects, *Nanomaterials*, 2022, **12**, 661.
- [72] X. Sang, Y. Xia, P. Sautet and J. P. Chang, Atomic layer etching of metals with anisotropy, specificity, and selectivity, *Journal of Vacuum Science & Technology A*, 2020, **38**, 043005.
- [73] T. Lill, *Atomic Layer Processing: Semiconductor Dry Etching Technology*, Wiley, 2021.
- [74] J. W. DuMont, A. E. Marquardt, A. M. Cano and S. M. George, Thermal Atomic Layer Etching of SiO<sub>2</sub> by a “Conversion-Etch” Mechanism Using Sequential Reactions of Trimethylaluminum and Hydrogen Fluoride, *ACS Applied Materials & Interfaces*, 2017, **9**, 10296–10307.
- [75] A. M. Cano, A. E. Marquardt, J. W. DuMont and S. M. George, Effect of HF Pressure on Thermal Al<sub>2</sub>O<sub>3</sub> Atomic Layer Etch Rates and Al<sub>2</sub>O<sub>3</sub> Fluorination, *The Journal of Physical Chemistry C*, 2019, **123**, 10346–10355.
- [76] Y. Lee and S. M. George, Thermal Atomic Layer Etching of Al<sub>2</sub>O<sub>3</sub>, HfO<sub>2</sub>, and ZrO<sub>2</sub> Using Sequential Hydrogen Fluoride and Dimethylaluminum Chloride Exposures, *The Journal of Physical Chemistry C*, 2019, **123**, 18455–18466.

- [77] J. C. Gertsch, A. M. Cano, V. M. Bright and S. M. George, SF<sub>4</sub> as the Fluorination Reactant for Al<sub>2</sub>O<sub>3</sub> and VO<sub>2</sub> Thermal Atomic Layer Etching, *Chemistry of Materials*, 2019, **31**, 3624–3635.
- [78] N. R. Johnson, H. Sun, K. Sharma and S. M. George, Thermal atomic layer etching of crystalline aluminum nitride using sequential, self-limiting hydrogen fluoride and Sn(acac)<sub>2</sub> reactions and enhancement by H<sub>2</sub> and Ar plasmas, *Journal of Vacuum Science & Technology A*, 2016, **34**, 050603.
- [79] M. Konh, C. He, X. Lin, X. Guo, V. Pallem, R. L. Opila, A. V. Teplyakov, Z. Wang and B. Yuan, Molecular mechanisms of atomic layer etching of cobalt with sequential exposure to molecular chlorine and diketones, *Journal of Vacuum Science & Technology A*, 2019, **37**, 021004.
- [80] M. Konh, Y. Wang, H. Chen, S. Bhatt, J. Q. Xiao and A. V. Teplyakov, Selectivity in atomically precise etching: Thermal atomic layer etching of a CoFeB alloy and its protection by MgO, *Applied Surface Science*, 2022, **575**, 151751.
- [81] E. Mohimi, X. I. Chu, B. B. Trinh, S. Babar, G. S. Girolami and J. R. Abelson, Thermal Atomic Layer Etching of Copper by Sequential Steps Involving Oxidation and Exposure to Hexafluoroacetylacetone, *ECS Journal of Solid State Science and Technology*, 2018, **7**, P491–P495.
- [82] X. Lin, M. Chen, A. Janotti and R. Opila, In situ XPS study on atomic layer etching of Fe thin film using Cl<sub>2</sub> and acetylacetone, *Journal of Vacuum Science & Technology A*, 2018, **36**, 051401.
- [83] M. Konh, A. Janotti and A. Teplyakov, Molecular Mechanism of Thermal Dry Etching of Iron in a Two-Step Atomic Layer Etching Process: Chlorination Followed by Exposure to Acetylacetone, *The Journal of Physical Chemistry C*, 2021, **125**, 7142–7154.
- [84] N. R. Johnson, J. K. Hite, M. A. Mastro, C. R. Eddy and S. M. George, Thermal atomic layer etching of crystalline GaN using sequential exposures of XeF<sub>2</sub> and BCl<sub>3</sub>, *Applied Physics Letters*, 2019, **114**, 243103.
- [85] W. Lu, Y. Lee, J. C. Gertsch, J. A. Murdzek, A. S. Cavanagh, L. Kong, J. A. del Alamo and S. M. George, In Situ Thermal Atomic Layer Etching for Sub-5 nm InGaAs Multigate MOSFETs, *Nano Letters*, 2019, **19**, 5159–5166.
- [86] J. A. Murdzek, A. Lii-Rosales and S. M. George, Thermal Atomic Layer Etching of Nickel Using Sequential Chlorination and Ligand-Addition Reactions, *Chemistry of Materials*, 2021, **33**, 9174–9183.
- [87] A. I. Abdulagatov and S. M. George, Thermal Atomic Layer Etching of Silicon Using O<sub>2</sub>, HF, and Al(CH<sub>3</sub>)<sub>3</sub> as the Reactants, *Chemistry of Materials*, 2018, **30**, 8465–8475.
- [88] A. I. Abdulagatov and S. M. George, Thermal atomic layer etching of silicon nitride using an oxidation and “conversion etch” mechanism, *Journal of Vacuum Science & Technology A*, 2020, **38**, 022607.

- [89] Y. Lee and S. M. George, Thermal Atomic Layer Etching of Titanium Nitride Using Sequential, Self-Limiting Reactions: Oxidation to TiO<sub>2</sub> and Fluorination to Volatile TiF<sub>4</sub>, *Chemistry of Materials*, 2017, 8202–8210.
- [90] W. Xie, P. C. Lemaire and G. N. Parsons, Thermally Driven Self-Limiting Atomic Layer Etching of Metallic Tungsten Using WF<sub>6</sub> and O<sub>2</sub>, *ACS Applied Materials & Interfaces*, 2018, **10**, 9147–9154.
- [91] D. R. Zywootko and S. M. George, Thermal Atomic Layer Etching of ZnO by a “Conversion-Etch” Mechanism Using Sequential Exposures of Hydrogen Fluoride and Trimethylaluminum, *Chemistry of Materials*, 2017, **29**, 1183–1191.
- [92] W. M. Haynes, D. R. Lide and T. J. Bruno, *CRC handbook of chemistry and physics*, CRC Press, 97th edn., 2017.
- [93] R. Mullins, S. Kondati Natarajan, S. D. Elliott and M. Nolan, Self-Limiting Temperature Window for Thermal Atomic Layer Etching of HfO<sub>2</sub> and ZrO<sub>2</sub> Based on the Atomic-Scale Mechanism, *Chemistry of Materials*, 2020, **32**, 3414–3426.
- [94] N. Cai, G. Zhou, K. Müller and D. E. Starr, Tuning the Limiting Thickness of a Thin Oxide Layer on Al(111) with Oxygen Gas Pressure, *Physical Review Letters*, 2011, **107**, 035502.
- [95] H. Schmalzried, A. T. Fromhold, jr.: Theory of Metal Oxidation. Vol. 1: Fundamentals, *Berichte der Bunsengesellschaft für physikalische Chemie*, 1977, **81**, 353–354.
- [96] B. E. Deal and A. S. Grove, General Relationship for the Thermal Oxidation of Silicon, *Journal of Applied Physics*, 1965, **36**, 3770–3778.
- [97] C. A. Paz de Araujo, Kinetics of Rapid Thermal Oxidation, *Journal of The Electrochemical Society*, 1989, **136**, 2673–2676.
- [98] A. Fick, Ueber Diffusion, *Annalen der Physik*, 1855, **170**, 59–86.
- [99] S. Jakschik, U. Schroeder, T. Hecht, D. Krueger, G. Dollinger, A. Bergmaier, C. Luhmann and J. W. Bartha, Physical characterization of thin ALD–Al<sub>2</sub>O<sub>3</sub> films, *Applied Surface Science*, 2003, **211**, 352–359.
- [100] D.-S. Yoon and J. Roh, Novel Diffusion-Barrier Materials Against Oxygen for High-Density Dynamic Random Access Memory Capacitors, *Advanced Functional Materials*, 2002, **12**, 373–381.
- [101] N. Miyoshi, H. Kobayashi, K. Shinoda, M. Kurihara, T. Watanabe, Y. Kouzuma, K. Yokogawa, S. Sakai and M. Izawa, Atomic layer etching of silicon nitride using infrared annealing for short desorption time of ammonium fluorosilicate, *Japanese Journal of Applied Physics*, 2017, **56**, 06HB01.

- [102] D. Smith, T. Lill and A. Fischer, *Atomic layer etching methods and apparatus*, 2020, <https://patents.google.com/patent/US10692724B2/en>, US10692724B2.
- [103] A. Lii-Rosales, A. S. Cavanagh, A. Fischer, T. Lill and S. M. George, Spontaneous Etching of Metal Fluorides Using Ligand-Exchange Reactions: Landscape Revealed by Mass Spectrometry, *Chemistry of Materials*, 2021, **33**, 7719–7730.
- [104] M. A. George, D. W. Hess, S. E. Beck, K. Young, D. A. Bohling, G. Voloshin and A. P. Lane, Reaction of 1,1,1,5,5,5-Hexafluoro-2,4-pentanedione Hhfac with Iron and Iron Oxide Thin films, *Journal of The Electrochemical Society*, 1996, **143**, 3257–3266.
- [105] G. Oehrlein, D. Metzler and C. Li, Atomic Layer Etching at the Tipping Point: An Overview, *ECS Journal of Solid State Science and Technology*, 2015, **4**, N5041–N5053.
- [106] R. Landau, Corrosion by Fluorine and Fluorine Compounds, *CORROSION*, 1952, **8**, 283–288.
- [107] G. C. Whitaker, Corrosion of Metals in Fluorine And Hydrofluoric Acid, *CORROSION*, 1950, **6**, 283–285.
- [108] A. H. Singleton, J. F. Tompkins, S. Kleinberg and C. J. Sterner, Corrosion of Metals by Liquid Fluorine, *Industrial & Engineering Chemistry*, 1965, **57**, 47–53.
- [109] R. Doering and Y. Nishi, *Handbook of Semiconductor Manufacturing Technology*, CRC Press, 2nd edn., 2017.
- [110] D. A. Hope, Contamination problems in the semiconductor industry, *Microelectronics Reliability: Environmental Engng, November (1968)*, 1969, **8**, 149–150.
- [111] E. Navickas, T. M. Huber, Y. Chen, W. Hetaba, G. Holzlechner, G. Rupp, M. Stöger-Pollach, G. Friedbacher, H. Hutter, B. Yildiz and J. Fleig, Fast oxygen exchange and diffusion kinetics of grain boundaries in Sr-doped LaMnO<sub>3</sub> thin films, *Physical Chemistry Chemical Physics*, 2015, **17**, 7659–7669.
- [112] R. Schmiedl, V. Demuth, P. Lahnor, H. Godehardt and Y. Bodschwinn, Oxygen diffusion through thin Pt films on Si(100), *Applied Physics*, 1996, **62**, 223–230.
- [113] D. Gupta and P. S. Ho, *Diffusion phenomena in thin films and microelectronic materials*, Noyes Publications, Park Ridge, 1989, vol. 2, p. 588.
- [114] J. Appenzeller, J. A. del Alamo, R. Martel, K. Chan and P. Solomon, Ultrathin 600°C Wet Thermal Silicon Dioxide, *Journal of The Electrochemical Society*, 1999, **3**, 84–86.

- [115] G. Dingemans, C. V. Helvoirt, M. C. M. Van de Sanden and W. M. M. Kessels, Plasma-Assisted Atomic Layer Deposition of Low Temperature SiO<sub>2</sub>, *Journal of The Electrochemical Society*, 2019, **35**, 191–204.
- [116] J. M. Olson, Analysis of LPCVD process conditions for the deposition of low stress silicon nitride. Part I: preliminary LPCVD experiments, *Materials Science in Semiconductor Processing*, 2002, **5**, 51–60.
- [117] L. Gosset, J.-F. Damlencourt, O. Renault, D. Rouchon, P. Holliger, A. Ermolieff, I. Trimaille, J.-J. Ganem, F. Martin and M.-N. Séméria, Interface and material characterization of thin Al<sub>2</sub>O<sub>3</sub> layers deposited by ALD using TMA/H<sub>2</sub>O, *Journal of Non-Crystalline Solids*, 2002, **303**, 1–23.
- [118] M. Ritala, M. Leskelä, L. Niinistö, T. Prohaska, G. Friedbacher and M. Grasserbauer, Development of crystallinity and morphology in hafnium dioxide thin films grown by atomic layer epitaxy, *Thin Solid Films*, 1994, **250**, 72–80.
- [119] C. H. Ahn, S. G. Cho, H. J. Lee, K. H. Park and S. H. Jeong, Characteristics of TiCl<sub>4</sub> thin films grown by ALD using TiCl<sub>4</sub> and NH<sub>3</sub>, *Metals and Materials International*, 2001, **7**, 621–625.
- [120] A. D. Pienaar, Niobium and tantalum beneficiation using gas-phase fluorination, *PhD dissertation (University of Pretoria)*, available online: <http://hdl.handle.net/2263/46243>, 2015, 1–107.
- [121] D. L. Hildenbrand and R. A. McDonald, The Heat of Vaporization and Vapor Pressure of Carbon Tetrachloride; The Entropy from Calorimetric Data., *The Journal of Physical Chemistry*, 1959, **63**, 1521–1522.
- [122] D. R. Stull, Vapor Pressure of Pure Substances. Organic and Inorganic Compounds, *Industrial & Engineering Chemistry*, 1947, **39**, 517–540.
- [123] M. Modreanu, P. Cosmin, S. Cosmin, C. Cobianu and C. Dunare, 1996 International Semiconductor Conference. 19th Edition. CAS'96 Proceedings, 1996, pp. 409–412.
- [124] Schrödinger, LLC, New York, NY, 2020, *Schrödinger : Maestro suite (version 11.0)*, <https://www.schrodinger.com/user-announcement/announcing-schrodinger-software-release-2020-1>.
- [125] J. P. Perdew, K. Burke and M. Ernzerhof, Generalized Gradient Approximation Made Simple, *Phys. Rev. Lett.*, 1996, **77**, 3865–3868.
- [126] D. Rappoport, N. R. M. Crawford, F. Furche and K. Burke, *Approximate Density Functionals: Which Should I Choose?*, John Wiley & Sons, Ltd, 2009.
- [127] K. F. Garrity, J. W. Bennett, K. M. Rabe and D. Vanderbilt, *GBRV pseudopotential library*, <https://www.physics.rutgers.edu/gbrv/>, (accessed 2020-07-25).

- [128] H. J. Monkhorst and J. D. Pack, Special points for Brillouin-zone integrations, *Phys. Rev. B*, 1976, **13**, 5188–5192.
- [129] P. Giannozzi, S. Baroni, N. Bonini, M. Calandra, R. Car, C. Cavazzoni, D. Ceresoli, G. L. Chiarotti, M. Cococcioni, I. Dabo, A. Dal Corso, S. de Gironcoli, S. Fabris, G. Fratesi, R. Gebauer, U. Gerstmann, C. Gougoussis, A. Kokalj, M. Lazzeri, L. Martin-Samos, N. Marzari, F. Mauri, R. Mazzarello, S. Paolini, A. Pasquarello, L. Paulatto, C. Sbraccia, S. Scandolo, G. Sclauzero, A. P. Seitsonen, A. Smogunov, P. Umari and R. M. Wentzcovitch, Quantum ESPRESSO: a modular and open-source software project for quantum simulations of materials, *Journal of Physics: Condensed Matter*, 2009, **21**, 395502.
- [130] P. Giannozzi, O. Andreussi, T. Brumme, O. Bunau, M. B. Nardelli, M. Calandra, R. Car, C. Cavazzoni, D. Ceresoli, M. Cococcioni, N. Colonna, I. Carnimeo, A. D. Corso, S. de Gironcoli, P. Delugas, R. A. D. Jr, A. Ferretti, A. Floris, G. Fratesi, G. Fugallo, R. Gebauer, U. Gerstmann, F. Giustino, T. Gorni, J. Jia, M. Kawamura, H.-Y. Ko, A. Kokalj, E. Küçükbenli, M. Lazzeri, M. Marsili, N. Marzari, F. Mauri, N. L. Nguyen, H.-V. Nguyen, A. O. de-la Roza, L. Paulatto, S. Poncé, D. Rocca, R. Sabatini, B. Santra, M. Schlipf, A. P. Seitsonen, A. Smogunov, I. Timrov, T. Thonhauser, P. Umari, N. Vast, X. Wu and S. Baroni, Advanced capabilities for materials modelling with Quantum ESPRESSO, *Journal of Physics: Condensed Matter*, 2017, **29**, 465901.
- [131] S. Kondati Natarajan and S. D. Elliott, Modeling the Chemical Mechanism of the Thermal Atomic Layer Etch of Aluminum Oxide: A Density Functional Theory Study of Reactions during HF Exposure, *Chemistry of Materials*, 2018, **30**, 5912–5922.
- [132] K. Arts, V. Vandalon, R. L. Puurunen, M. Utriainen, F. Gao, W. M. M. Kessels and H. C. M. Knoop, Sticking probabilities of H<sub>2</sub>O and Al(CH<sub>3</sub>)<sub>3</sub> during atomic layer deposition of Al<sub>2</sub>O<sub>3</sub> extracted from their impact on film conformality, *Journal of Vacuum Science & Technology A*, 2019, **37**, 030908.
- [133] G. Kresse and J. Furthmüller, Efficient iterative schemes for ab initio total-energy calculations using a plane-wave basis set, *Phys. Rev. B*, 1996, **54**, 11169.
- [134] G. Kresse and D. Joubert, From ultrasoft pseudopotentials to the projector augmented-wave method, *Phys. Rev. B*, 1999, **59**, 1758.
- [135] *TURBOMOLE V6.2 2010, a development of University of Karlsruhe and Forschungszentrum Karlsruhe GmbH, 1989-2007, TURBOMOLE GmbH, since 2007; available from <http://www.turbomole.com> last accessed 27/11/2019*, 2010.
- [136] A. Togo and I. Tanaka, First principles phonon calculations in materials science, *Scr. Mater.*, 2015, **108**, 1–5.

- [137] M. J. Young, N. M. Bedford, A. Yanguas-Gil, S. Letourneau, M. Coile, D. J. Mandia, B. Aoun, A. S. Cavanagh, S. M. George and J. W. Elam, Probing the Atomic-Scale Structure of Amorphous Aluminum Oxide Grown by Atomic Layer Deposition, *ACS Applied Materials & Interfaces*, 2020, **12**, 22804–22814.
- [138] A. Buechler, E. P. Marram and J. L. Stauffer, Sublimation of aluminum trifluoride and the infrared spectrum of gaseous aluminum fluoride, *Journal of Physical Chemistry*, 1967, **71**, 4139–4140.
- [139] S. S. Zumdahl and D. J. DeCoste, *Introductory Chemistry, Sixth Edition*, Houghton Mifflin, 6th edn., 2007.
- [140] Z. Zhou, J. Chen, H. Yuan and J. Nie, Effects of Aluminum Particle Size on the Detonation Pressure of TNT/Al, *Propellants, Explosives, Pyrotechnics*, 2017, **42**, 1401–1409.
- [141] J.-W. Kim, Y.-C. Kim and W.-J. Lee, Reactive ion etching mechanism of plasma enhanced chemically vapor deposited aluminum oxide film in  $\text{CF}_4/\text{O}_2$  plasma, *Journal of Applied Physics*, 1995, **78**, 2045–2049.
- [142] B. J. Park, W. S. Lim, J. K. Yeon, Y. Y. Kim, S. K. Kang, J. T. Lim and G. Y. Yeom, Fluorination of Aluminum Oxide Gate Dielectrics Using Fluorine Neutral/Ion Beams, *Journal of Nanoscience and Nanotechnology*, 2011, **11**, 5904–5908.
- [143] S. Andersson and A. Åström, The Thermal Decomposition of  $\text{NbO}_2\text{F}$ , *Acta Chemica Scandinavica*, 1965, **19**, 2136–2138.
- [144] M. Binnewies, R. Glaum, M. Schmidt and P. Schmidt, *Chemische Transportreaktionen*, De Gruyter, 2011, pp. 159–285.
- [145] H. Schäfer and M. Hüesker, Beiträge zur Chemie der Elemente Niob und Tantal. XXX. Chemische Transportreaktionen. VIII. Über die Darstellung der Nioboxide und ihren Transport im Temperaturgefälle, *Zeitschrift für anorganische und allgemeine Chemie (John Wiley and Sons)*, 1962, **317**, 321–333.
- [146] G. J. Orloff, S. L. Bernasek, G. L. Wolk and R. J. Coyle, Laser-Assisted Etching of Lithium Niobate, *Materials Research Society Proceedings*, 1988, **126**, 251–256.
- [147] S. Li, C. Sun and H. Park, Grain boundary structures of atomic layer deposited TiN, *Thin Solid Films*, 2006, **504**, 108–112.
- [148] K.-E. Elers, J. Winkler, K. Weeks and S. Marcus,  $\text{TiCl}_4$  as a Precursor in the TiN Deposition by ALD and PEALD, *The Electrochemical Society*, 2005, **152**, G589.
- [149] E. Capelli and R. Konings, Thermodynamic assessment of the niobium-fluorine system by coupling density functional theory and CALPHAD approach, *Journal of Fluorine Chemistry*, 2018, **208**, 55–64.



- [150] G. H. Coleman, R. W. Leeper, C. C. Schulze, L. D. Scott and W. C. Fernelius, in *Cyanogen Chloride*, John Wiley & Sons, Ltd, 1946, pp. 90–94.
- [151] R. E. McCarley and B. A. Torp, The Preparation and Properties of Niobium(IV) Compounds. I. Some Niobium(IV) Halides and their Pyridine Adducts, *Inorganic Chemistry*, 1963, **2**, 540–546.
- [152] T. Pilvi, M. Ritala, M. Leskelä, M. Bischoff, U. Kaiser and N. Kaiser, Atomic layer deposition process with  $\text{TiF}_4$  as a precursor for depositing metal fluoride thin films, *Applied Optics*, 2008, **47**, C271–C274.
- [153] E. H. Hall, J. M. Blocher and I. E. Campbell, Vapor Pressure of Titanium Tetrafluoride, *Journal of The Electrochemical Society*, 1958, **105**, 275–278.
- [154] G. Ramanath, J. E. Greene, J. R. A. Carlsson, L. H. Allen, V. C. Hornback and D. J. Allman, W deposition and titanium fluoride formation during  $\text{WF}_6$  reduction by Ti: Reaction path and mechanisms, *Journal of Applied Physics*, 1999, **85**, 1961–1969.
- [155] *Lange's handbook of chemistry*, ed. J. A. Dean, McGraw-Hill: New York, 12th edn., 1979, p. 1470.
- [156] I. Barin, *Thermochemical Data of Pure Substances, Third Edition*, VCH Verlagsgesellschaft mbH, 3rd edn., 1995.
- [157] L. Holland and L. Laurenson, Pumping characteristics of a titanium droplet getter-ion pump, *British Journal of Applied Physics*, 1960, **11**, 401.
- [158] M. A. Greenbaum, J. A. Blauer, M. R. Arshadi and M. Farber, Heat of formation of  $\text{AlOCl(g)}$ , *Transactions of the Faraday Society*, 1964, **60**, 1592.
- [159] H. Schäfer, F. Wartenpfehl and E. Weise, Über Titanchloride. V. Titan(III)-oxychlorid, *Zeitschrift für anorganische und allgemeine Chemie*, 1958, **295**, 268–280.
- [160] H. Sekimoto, Y. Nose, T. Uda and H. Sugimura, Preparation and Properties of Trivalent Titanium Compounds,  $\text{TiCl}_3$  and  $\text{TiOCl}$ , *High Temperature Materials and Processes*, 2011, **30**, 435–440.
- [161] J. T. Viola, D. W. Seegmiller, A. A. Fannin and L. A. King, Vapor pressure of aluminum chloride systems. 1. Vapor pressure and triple point of pure aluminum chloride, *Journal of Chemical & Engineering Data*, 1977, **22**, 367–370.
- [162] H. C. Lisel Bayer, Das Aluminiumoxychlorid  $\text{AlOCl}$ , *Zeitschrift für anorganische und allgemeine Chemie*, 1950, **263**, 87–101.
- [163] M. Farber and A. J. Darnell, The Disproportionation and Vapor Pressure of  $\text{TiCl}_3$ , *The Journal of Physical Chemistry*, 1955, **59**, 156–159.
- [164] M. Farber, A. J. Darnell and F. Brown, X-Ray Diffraction Patterns of  $\text{TiCl}_2$  and  $\text{TiCl}_3$ , *The Journal of Chemical Physics*, 1955, **23**, 1556.

- [165] G. B. Skinner and R. A. Ruehrwein, Thermodynamic Properties of the Titanium Chlorides, *The Journal of Physical Chemistry*, 1955, **59**, 113–117.
- [166] V. Grossi, L. Ottaviano, S. Santucci and M. Passacantando, XPS and SEM studies of oxide reduction of germanium nanowires, *Journal of Non-Crystalline Solids*, 2010, **356**, 1988–1993.
- [167] M. H. Kibel and P. W. Leech, X-ray Photoelectron Spectroscopy Study of Optical Waveguide Glasses, *Surface and Interface Analysis*, 1996, **24**, 605–610.
- [168] D. Schmeisser, R. Schnell, A. Bogen, F. Himpsel, D. Rieger, G. Landgren and J. Morar, Surface oxidation states of germanium, *Surface Science*, 1986, **172**, 455–465.
- [169] Y. Xu, G. Han, H. Liu, Y. Wang, Y. Liu, J. Ao and Y. Hao, Ge pMOSFETs with GeO<sub>x</sub> Passivation Formed by Ozone and Plasma Post Oxidation, *Nanoscale Research Letters*, 2019, **14**, 126–.
- [170] F. Bellenger, M. Houssa, A. Delabie, V. Afanasiev, T. Conard, M. Caymax, M. Meuris, K. De Meyer and M. M. Heyns, Passivation of Ge(100)/GeO<sub>2</sub>/high- $\kappa$  Gate Stacks Using Thermal Oxide Treatments, *Journal of The Electrochemical Society*, 2008, **155**, G33.
- [171] G. Hollinger and F. J. Himpsel, Oxygen chemisorption and oxide formation on Si(111) and Si(100) surfaces, *Journal of Vacuum Science & Technology A Vacuum Surfaces and Films*, 1983, **1**, 640–645.
- [172] G. Hollinger and F. J. Himpsel, Probing the transition layer at the SiO<sub>2</sub>-Si interface using core level photoemission, *Applied Physics Letters*, 1984, **44**, 93–95.
- [173] A. Deshpande, R. Inman, G. Jursich and C. Takoudis, Characterization of hafnium oxide grown on silicon by atomic layer deposition: Interface structure, *Microelectronic Engineering*, 2006, **83**, 547–552.
- [174] F. Fracassi, R. D'Agostino, A. Fornelli and T. Shirafuji, Dry Etching of SiO<sub>2</sub> Thin Films with Perfluoropropenoxide–O<sub>2</sub> and Perfluoropropene–O<sub>2</sub> Plasmas, *Japanese Journal of Applied Physics*, 2002, **41**, 6287–6290.
- [175] O. Böse, E. Kemnitz, A. Lippitz and W. E. S. Unger, C 1s and Au 4f<sub>7/2</sub> referenced XPS binding energy data obtained with different aluminium oxides, -hydroxides and -fluorides, *Analytical and Bioanalytical Chemistry*, 1997, **358**, 175–179.
- [176] A. E. Hughes, M. M. Hedges and B. A. Sexton, Reactions at the Al/SiO<sub>2</sub>/SiC layered interface, *Journal of Materials Science*, 1990, **25**, 4856–4865.
- [177] K. Roodenko, M. D. Halls, Y. Gogte, O. Seitz, J.-F. Veyan and Y. J. Chabal, Nature of Hydrophilic Aluminum Fluoride and Oxyaluminum Fluoride Surfaces Resulting from XeF<sub>2</sub> Treatment of Al and Al<sub>2</sub>O<sub>3</sub>, *The Journal of Physical Chemistry C*, 2011, **115**, 21351–21357.

- [178] B.-H. Liao, C.-N. Hsiao and C.-C. Lee, Aluminum oxyfluoride films for deep ultraviolet optics deposited by a combined HIPIMS/CFUBMS deposition technique, *Optical Materials Express*, 2016, **6**, 1506–1512.
- [179] A. Hess, E. Kemnitz, A. L. W. Unger and D. Menz, ESCA, XRD, and IR Characterization of Aluminum Oxide, Hydroxyfluoride, and Fluoride Surfaces in Correlation with Their Catalytic Activity in Heterogeneous Halogen Exchange Reactions, *Journal of Catalysis*, 1994, **148**, 270–280.
- [180] B. M. Vilakazi, O. S. Monnahela, J. B. Wagener, P. A. Carstens and T. Ntsoane, A thermogravimetric study of the fluorination of zirconium and hafnium oxides with anhydrous hydrogen fluoride gas, *Journal of Fluorine Chemistry*, 2012, **141**, 64–68.
- [181] S. Arrhenius, Über die Dissociationswärme und den Einfluss der Temperatur auf den Dissociationsgrad der Elektrolyte, *Zeitschrift für Physikalische Chemie*, 1889, **4U**, 96–116.
- [182] S. Arrhenius, Über die Reaktionsgeschwindigkeit bei der Inversion von Rohrzucker durch Säuren, *Zeitschrift für Physikalische Chemie*, 1889, **4**, 226–248.
- [183] H. Shimizu and T. Sato, Kinetics of Ultrathin Thermal Oxide Growth on Si(001) Surfaces, *Japanese Journal of Applied Physics*, 2005, **44**, 808–812.
- [184] A. Le Claire, The theory of  $D_0$  in the Arrhenius equation for self-diffusion in cubic metals, *Acta Metallurgica*, 1953, **1**, 438–447.
- [185] J. W. A. M. Gielen, W. M. M. Kessels, M. C. M. van de Sanden and D. C. Schram, Effect of substrate conditions on the plasma beam deposition of amorphous hydrogenated carbon, *Journal of Applied Physics*, 1997, **82**, 2643–2654.
- [186] Y.-R. Luo, *Handbook of Bond Dissociation Energies in Organic Compounds*, CRC Press, 1st edn., 2002.



## Appendix A: Bond dissociation energies

The bond dissociation energy (BDE) of a bond M-X is a standard enthalpy change, at 298 K, in a reaction:  $M-X \rightarrow M + X$ .<sup>109</sup> BDE is proportional to the bond strength and can be used to measure the strength of a chemical bond M-X.<sup>92,109</sup> Table A.1 shows BDE values in kJ/mol for various bonds that are taken from the CRC database.<sup>186</sup> The values for Nb-Cl and Nb-F were not found and are estimated by extrapolating the BDE values for corresponding Ta and V halides. The extrapolation is based on the group trends in the periodic table. However, the group trends are not always valid as sometimes exceptions are also encountered. To verify the accuracy of the extrapolated BDE values, a similar estimation was done for the BDE values of Nb-O, Nb-N and less than 10 % error was observed.

Table A.1: Bond dissociation energies of selected M-X bonds.

<b>Bond</b>	<b>Bond dissociation energy (kJ/mol)</b>
Ti-C	423
Ti-Cl	405
Ti-F	569
Ti-N	476
Nb-C	524
Nb-F	582
Nb-Cl	511
Nb-N	540